Universiteit
Leiden
The Netherlands

Three-dimensional quantitative coronary angiography and the registration with intravascular ultrasound and optical coherence tomography

Tu, S.

Citation
Tu, S. (2012, February 28). *Three-dimensional quantitative coronary angiography and the registration with intravascular ultrasound and optical coherence tomography. ASCI dissertation series*. Retrieved from https://hdl.handle.net/1887/18531

Version:	Corrected Publisher's Version
License:	Licence agreement concerning inclusion of doctoral thesis in the Institutional Repository of the University of Leiden
Downloaded from:	https://hdl.handle.net/1887/18531

Note: To cite this publication please use the final published version (if applicable).

Three-dimensional Quantitative Coronary Angiography and the Registration with Intravascular Ultrasound and Optical Coherence Tomography

Shengxian Tu

2012

Printed by: Proefschriftmaken.nl

ISBN: 978-90-8891-380-8

© 2012, Shengxian Tu, Leiden, the Netherlands. All rights reserved. No part of this publication may be reproduced or transmitted in any form or by any means, electronic or mechanical, including photocopying, recording or any information storage and retrieval system, without prior permission in writing from the copyright owner.

Three-dimensional Quantitative Coronary Angiography and the Registration with Intravascular Ultrasound and Optical Coherence Tomography

Proefschrift

ter verkrijging van
de graad van Doctor aan de Universiteit Leiden,
op gezag van Rector Magnificus prof. mr. P.F. van der Heijden
volgens besluit van het College van Promoties
ter verdediging op dinsdag 28 februari 2012
klokke 15:00 uur

door

Shengxian Tu

geboren te Raoping, Guangdong, China
in 1981

PROMOTIECOMMISIE

Promotor:
Prof. dr. ir. J.H.C. Reiber

Co-promotores:
ir. G. Koning
dr. ir. J. Dijkstra

Overige leden:
Prof. dr. W. Niessen (Erasmus MC, Rotterdam)
Prof. dr. J.W. Jukema
Prof. dr. W. Wijns (Cardiovascular Centre, OLV Hospital, Aalst, Belgium)

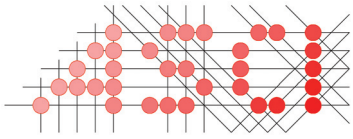

The work was carried out in the ASCI graduate school.
ASCI dissertation series number 252.

Financial support for the publication of this thesis was kindly provided by:

- Bontius Stichting inz. Doelfonds Beeldverwerking
- Medis medical imaging systems bv
- ASCI research school
- Volcano Europe BVBA
- St. Jude Medical

Contents

1 **Introduction and outline 1**
1.1 Quantitative coronary angiography 2
1.2 Three-dimensional angiographic reconstruction and registration 3
1.3 Motivation and objectives 5
1.4 Thesis outline 6
1.5 References 8

2 **Coronary angiography enhancement for visualization 11**
2.1 Introduction 13
2.2 Methods 15
2.2.1 Original lateral inhibition model 15
2.2.2 Stick-guided lateral inhibition 16
2.2.3 Validation 18
2.3 Statistics 20
2.4 Results 21
2.4.1 Visual interpretation 21
2.4.2 Quantitative results 22
2.5 Discussions 23
2.6 Conclusions 25
2.7 References 25

3 **Assessment of obstruction length and optimal viewing angle from biplane X-ray angiograms 27**
3.1 Introduction 29
3.2 Methods 30
3.2.1 Image geometry 30
3.2.2 Approximation of the isocenter offset 32
3.2.3 Centerline reconstruction 33
3.3 Applications 34
3.3.1 Obstruction length assessment 34
3.3.2 Bifurcation optimal viewing angle assessment 36
3.4 Validations 38
3.4.1 Data acquisition protocols 38
3.4.2 Segment length assessment 39
3.4.3 Bifurcation optimal viewing angle 39
3.5 Statistics 40
3.6 Results 41
3.7 Discussions 43
3.8 Conclusions 45
3.9 References 45

4 **The impact of acquisition angle differences on three-dimensional quantitative coronary angiography 49**
4.1 Introduction 51
4.2 Materials and methods 51
4.2.1 Assembled brass phantom 51
4.2.2 Silicone bifurcation phantom 54
4.3 Statistics 56
4.4 Results 56
4.5 Discussions 59
4.6 Limitations 61
4.7 Conclusions 62
4.8 References 62

5 **A novel three-dimensional quantitative coronary angiography system: In-vivo comparison with intravascular ultrasound for assessing arterial segment length 65**
5.1 Introduction 67
5.2 Materials and methods 67
5.2.1 Materials 67
5.2.2 Three-dimensional angiographic reconstruction and quantitative analysis 68
5.2.3 Quantitative IVUS analysis 70
5.3 Statistics 71
5.4 Results 72
5.5 Discussions 75
5.6 Limitations 78
5.7 Conclusions 78
5.8 References 78

6 **In-vivo assessment of optimal viewing angles from X-ray coronary angiography 81**
6.1 Introduction 83
6.2 Materials and methods 83
6.2.1 Population 83
6.2.2 Three-dimensional angiographic reconstruction 84
6.2.3 The determination of optimal viewing angles 86
6.2.4 Validation of overlap prediction 88
6.2.5 Validation of optimal viewing angles 88
6.3 Statistics 89
6.4 Results 89
6.4.1 Overlap prediction 89
6.4.2 Optimal viewing angle 90
6.5 Discussions 92
6.6 Conclusions 95
6.7 References 95

7 **In-vivo assessment of bifurcation optimal viewing angles and bifurcation angles by three-dimensional (3D) quantitative coronary angiography 99**
7.1 Introduction 101
7.2 Methods 102
7.2.1 Study population 102
7.2.2 Bifurcation optimal viewing angles 102
7.3 Statistics 106
7.4 Results 106
7.5 Discussions 109
7.6 Limitations 111
7.7 Conclusions 112
7.8 References 112

8 **Co-registration of three-dimensional quantitative coronary angiography and intravascular ultrasound or optical coherence tomography 115**
8.1 Introduction 117
8.2 Three-dimensional angiographic reconstruction 118
8.3 XA-IVUS/OCT registration 121
8.4 Validations 123
8.4.1 Phantoms validation 123
8.4.2 In-vivo validation 124
8.5 Statistics 124
8.6 Results 125
8.6.1 Phantoms 125

8.6.2 In-vivo 125
8.7 Discussions 126
8.8 Limitations 128
8.9 Conclusions 128
8.10 References 129

9 **In-vivo comparison of arterial lumen dimensions assessed by co-registered three-dimensional (3D) quantitative coronary angiography, intravascular ultrasound and optical coherence tomography 131**
9.1 Introduction 133
9.2 Methods 133
9.2.1 Study population 133
9.2.2 Three-dimensional quantitative coronary angiography 134
9.2.3 Calculation of vessel curvature 135
9.2.4 Registration of 3D QCA with IVUS or OCT 136
9.2.5 Frame selection and quantitative IVUS/OCT analysis 137
9.3 Statistics 138
9.4 Results 138
9.5 Discussions 143
9.6 Limitations 146
9.7 Conclusions 147
9.8 References 147

10 **Summary and conclusions 149**
10.1 Summary and conclusions 149
10.2 Future works 155

11 **Samenvatting en conclusies 157**
11.1 Samenvatting en conclusies 157
11.2 Toekomstige ontwikkelingen 163

List of abbreviations 165

Publications 166

Acknowledgments 168

Curriculum vitae 171

CHAPTER 1

Introduction and Outline

This chapter was adapted from:

QCA, IVUS and OCT in Interventional Cardiology in 2011
Johan H.C. Reiber, Shengxian Tu, Joan C. Tuinenburg, Gerhard Koning,
Johannes P. Janssen, Jouke Dijkstra
Cardiovascular Diagnosis and Therapy 2011; 1(1):57-70.

1.1 Quantitative Coronary Angiography

Quantitative coronary angiography (QCA) was first developed to quantify vessel motion and the effects of pharmacological agents on the regression and progression of coronary artery disease [1]. It has come a long way, from the early 1980's with the angiograms being acquired on 35 mm cinefilm and requiring very expensive cinefilm projectors with optimal zooming for the quantitative analysis [2], to modern complete digital imaging with the images acquired at resolutions of 512^2 or 1024^2 pixels, and with the image data widely available throughout the hospital by means of Cardiovascular Picture Archiving and Communication Systems or CPACS systems. Major differences were of course that on cinefilm the coronary arteries were displayed as bright arteries on a darker background, and there was always an associated pincushion distortion caused by the concave input screen of the image intensifier. With the digital systems the arteries are now displayed as dark vessels on a bright background and the modern flat-panel X-ray detectors are free from geometric distortions. Although there have been many years of debate about the resolution of cinefilm versus digital, the higher contrast resolution of the digital approach has compensated much of the higher spatial resolution of the 35 mm cinefilm, and thus digital has been completed accepted. Also, extensive validation studies have not proven major differences in accuracy and precision between cinefilm and digital: the variability in the analysis is on the order of about ½ pixel, or 0.11 mm [3, 4].

For many years, QCA has been used in clinical research in the hospitals and in core laboratories to assess regression and progression of coronary obstructions in pharmacological interventions, and of course for vessel sizing and the assessment of the efficacy of coronary interventions after the introduction of percutaneous transluminal coronary angioplasty (PTCA), bare-metal stents (BMS), drug-eluting stents (DES) and now also biodegradable stents. In all these cases, the analyses were done on straight vessels. However, since a number of years, bifurcation stenting has become of great interest, and in association with the European Bifurcation Club (EBC), the QCA software has been extended to allow also the quantitative analysis of the bifurcating morphology [5]. This has proven to be a lot more difficult, in particular in defining what the normal sizes of the vessels adjacent to the bifurcation should be, given the complexity of the anatomy and different disease patterns. Validated solutions have been created and are now being used in clinical trials [6-11]. Figure 1-1 shows an example of the validated bifurcation analysis using the T-shape model. The proximal main (parent) vessel, bifurcation core, and distal main vessel are combined into one section, with a step-

down in the reference diameter function at the bifurcation core. The side branch forms another section, with a hock at the mouse of the ostium in the reference diameter function. In such a way, the reference diameter functions represent the true, i.e., healthy, arterial diameter functions and lesion severity can be accurately assessed at the bifurcation including the ostium of the sidebranch.

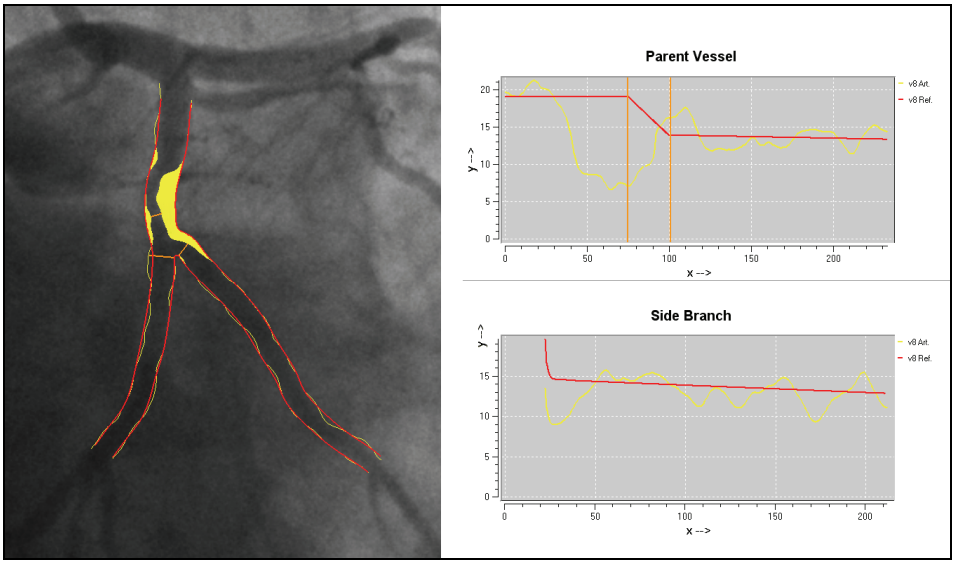

Figure 1-1. An example of the bifurcation analysis using the T-shape model: Left panel shows the obstructed bifurcation with plaque filling and with the detected arterial contours and estimated reference contours superimposed on the bifurcation. Right panel shows the two corresponding diameter functions of the main (parent) vessel and the sidebranch sections.

1.2 Three-dimensional Angiographic Reconstruction and Registration

Despite that dedicated QCA techniques has significantly evolved over the past years, at present, the assessment of absolute lumen dimensions by conventional two-dimensional (2D) analysis is still limited by the well-known errors due to vessel foreshortening and out-of-plane magnification [12, 13]. On the other hand, the increasing need to better understand coronary atherosclerosis and assess lumen dimensions for both off-line and on-line applications in cardiac catheterization laboratories has motivated the continuous development of advanced three-dimensional (3D) approaches. It was thought that 3D QCA could accurately assess lumen dimensions and extend the capacity of X-ray imaging in supporting coronary interventions, by means of restoring the vascular structures in the natural 3D shape.

Early research on 3D angiographic reconstruction can be traced back to decades ago [14, 15]. However, the applications of 3D QCA have never

been applied on a wide scale in on-line situations for a number of reasons: segmentation not robust enough, too many user-interactions required, extensive validations lacking, and acquisition protocols not standardized [24]. However, with the increasing applications of bifurcation stenting and the capability of automated calibrations in modern flat-panel X-ray systems, there may be new opportunities, in combination with improved segmentation and reconstruction approaches. In particular, proper sizing and positioning of the interventional devices has a significant effect on the long-term effect of the procedure [16], optimal viewing angles are more important in bifurcation assessments and interventions [17, 18], the change of bifurcation angles are used to predict the outcomes of bifurcation stenting procedures [19, 20], and last but not least, latest developments also allow for the registration with intravascular imaging modalities, such as IVUS and OCT [21, 22]. This registration links the abnormalities as seen in the IVUS or OCT pullback series with the positions in either the 2D X-ray angiogram, or the 3D reconstruction. In such a way, the interventionalist does not need to rely on his/her mental registration capabilities alone anymore. Besides, lumen dimensions assessed from different imaging modalities can be easily combined at every corresponding position along the arterial segment of interest.

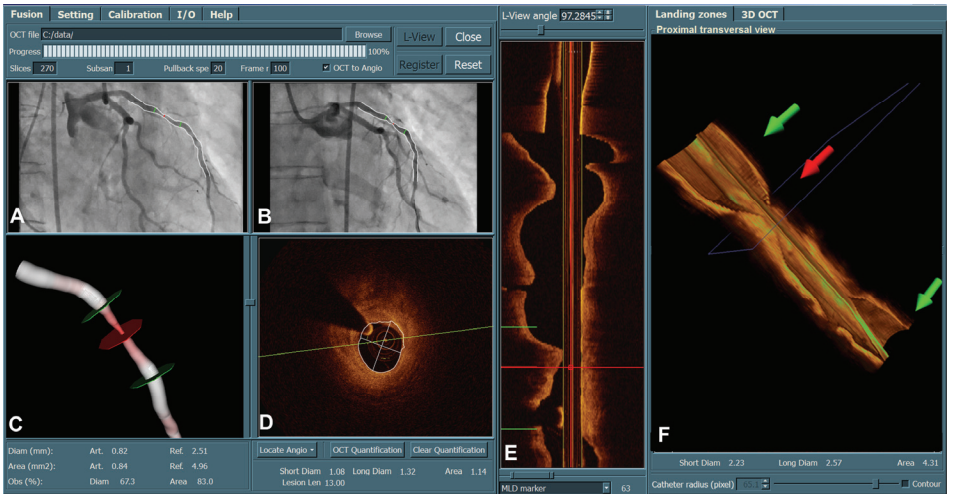

Figure 1-2. Three-dimensional quantitative coronary angiography (3D QCA) and its registration with 3D optical coherence tomography (OCT). A and B are the two angiographic views; C is the reconstructed vessel segment in color-coded fashion; D is the OCT cross-sectional view corresponding to the middle (red) marker; E is the OCT longitudinal view; and F is the 3D OCT image. After the registration, the corresponding markers in different views (A, B, C, E, and F) were synchronized, allowing the assessment of lumen dimensions from both imaging modalities at every corresponding position along the vessel segment. Courtesy: Department of Cardiology, Aarhus University Hospital, Skejby, Denmark.

An example of such an integration approach is given by Figure 1-2. The stenting-position, i.e., landing-zones, defined by the proximal and distal landing-zone markers has been mapped onto the two angiographic views in the top left panel (the two green markers that are superimposed on the angiographic views). Luminal contours can be automatically detected in the OCT cross-sectional images and the assessed lumen size can be compared with 3D QCA. In this case, short diameter, long diameter, and lumen area at the position indicated by the middle (red) marker were 1.08 mm, 1.32 mm, and 1.14 mm^2 by OCT, as compared with 0.82 mm, 1.30 mm, and 0.84 mm^2 by 3D QCA.

1.3 Motivation and Objectives

Coronary artery disease (CAD) is one of the leading causes of mortality and mobility worldwide. Actually, it is a disease starting with local thickening of the coronary artery wall and subsequently narrowing of the lumen of the vessel, which at a certain point in time limits the blood supply to the myocardial wall and in the end the patient experiences chest pain at exercise and rest. Such narrowings need to be treated. Mild and severe narrowings can also rupture, leading to thrombus formation and complete blockage of the artery, and subsequent myocardial infarction, or even death. Coronary angioplasty, i.e. stenting, is an invasive procedure carried out during a cardiac catheterization procedure to open the obstructed arteries. Despite the tremendous success of the procedure in the instant treatment of CAD, a higher risk of restenosis and thrombosis due to the suboptimal stent selection and deployment has hampered the translation of the procedure success into long-term outcomes [16, 23]. Drug-eluting stents have proven to be able to reduce the in-stent restenosis [24]; however, the efficacy depends to a great extent on complete lesion coverage and apposition, and therefore requires appropriate stent sizing and positioning [16, 25]. The ad hoc solution of deploying additional stents when the first-select stent turns out to be of insufficient length, could reduce the minimum stent area and increase the dose of drug release on the overlapping area, which have been demonstrated to be associated with an increased risk of restenosis and thrombosis [26]. In addition, the total expense for the treatment will increase significantly. On the other hand, a stent of excessive length or suboptimal deployment will unnecessarily change the behavior of the over-stented vessel segments, which may result in undesirable results, e.g., covering sidebranches [27], or may even lead to fracture of the stent. Advanced imaging and quantification systems are thus demanded to better support stent sizing and positioning during coronary interventions, and also for the accurate assessment of coronary obstructions.

The goal of this thesis is to come up with a robust and yet novel application that could restore the coronary vascular structures in 3D and explore both the global and the detailed anatomical characteristics that could be interesting for clinical research as well as for clinical decision making. As such, the objectives of this thesis are threefold:

1. To develop fast and reproducible approaches for the 3D X-ray angiographic reconstruction of coronary arteries including the bifurcation, and for the co-registration of X-ray images with intravascular imaging devices, e.g., intravascular ultrasound (IVUS) and optical coherence tomography (OCT).
2. To extend the proposed approaches into specific applications by which relevant anatomical parameters were assessed in an automated manner.
3. To conduct phantom and in-vivo clinical studies for the validation of such approaches and the derived anatomical parameters in typical clinical populations.

1.4 THESIS OUTLINE

This thesis is organized as follow:

Chapter 1 gives a brief overview of the QCA history including the recent developments in 3D QCA and the registration with IVUS or OCT. The motivation and objectives of this thesis are described.

Chapter 2 presents a new algorithm called stick-guided lateral inhibition (SGLI) to improve the quality of the visualization of coronary vascular structures. The SGLI algorithm was compared with the conventional unsharp masking algorithm on static angiographic image frames and the results were independently evaluated by international analysts and cardiologists.

Chapter 3 presents a new 3D QCA system using automated isocenter correction and refined epipolar line constraints, based on biplane X-ray angiographic acquisitions. The accuracy and variability in the assessment of vessel segment length and bifurcation optimal viewing angle were investigated by using phantom experiments.

Chapter 4 studies the impact of acquisition angle difference on the lumen dimensions as assessed by 3D QCA. X-ray angiographic images were recorded at multiple angiographic projections for an assembled brass phantom and a silicone bifurcation phantom. The projections were randomly matched and used for the 3D angiographic reconstruction and analysis. Lesion length, diameter stenosis, and reference diameter were assessed on the brass phantom, while bifurcation angels and bifurcation core volume were assessed on the silicone phantom.

Chapter 5 presents an in-vivo validation study for the comparison of arterial segment lengths as assessed by the proposed 3D QCA approach

and by IVUS using motorized pullback. In addition, the curvature of each analyzed segment was determined and the correlation between the accumulated curvature and the difference in the segment lengths assessed by these two imaging modalities was analyzed.

Chapter 6 presents a novel approach to predict the overlap condition and subsequently determine the optimal angiographic viewing angles for a selected coronary (target) segment from X-ray coronary angiography, without the need to reconstruct the whole coronary tree in 3D, such that subsequent interventions are carried out from the best view. The accuracy of overlap prediction was validated retrospectively by comparing the predicted overlap results with the true overlap conditions on the available angiographic views acquired during coronary angiography. Two experienced interventional cardiologists independently evaluated the success of the proposed optimal views with respect to the expert working views.

Chapter 7 assesses the bifurcation angles and the distribution of two bifurcation optimal viewing angles, i.e, the anatomy-defined bifurcation optimal viewing angle (ABOVA) and the obtainable bifurcation optimal viewing angle (OBOVA), in four main coronary bifurcations using the proposed 3D QCA approach. The ABOVA is characterized by having an orthogonal view of the bifurcation, such that overlap and foreshortening at the ostia are minimized. However, due to the mechanical constraints of the X-ray systems, certain deep angles cannot be reached by the C-arm. In addition, the possible overlap by other major coronary arteries could significantly influence the visualization of the bifurcation, rendering such an ABOVA less useful. Therefore, second best or, OBOVA has to be used as an alternative. The proportion of the later case was assessed in a typical clinical population.

Chapter 8 presents a new and fast approach for the co-registration of 3D QCA with IVUS or OCT, which provides the interventional cardiologist with detailed information about vessel size and plaque size at every position along the vessel of interest. The accuracy of the co-registration approach was retrospectively evaluated on silicone phantoms and in-vivo datasets.

Chapter 9 compares lumen dimensions as assessed in-vivo by 3D QCA and by IVUS or OCT, and to assess the possible association of the discrepancy with vessel curvature. The proposed co-registration approach was applied to guarantee the point-to-point correspondence between the X-ray, IVUS and OCT images, and to eliminate the error concerning a possible mismatch in the selection of the corresponding regions for the comparison of different imaging modalities.

Chapter 10 summarizes the main findings for each chapter.

1.5 REFERENCES

1. Brown BG, Bolson E, Frimer M, et al. Quantitative coronary angiography: estimation of dimensions, hemodynamic resistance, and atheroma mass of coronary artery lesions using arteriography in 256 nonoperated patients. Circulation 1977; 55:329–337.
2. Reiber JHC, Serruys PW, Kooijman CJ, et al. Assessment of short-, medium-, and long-term variations in arterial dimensions from computer-assisted quantitation of coronary cineangiograms. Circulation 1985; 71:280-288.
3. Reiber JHC, van der Zwet PM, Koning G, et al. Accuracy and precision of quantitative digital coronary arteriography: observer-, short-, and medium-term variabilities. Cathet Cardiovasc Diagn 1993; 28:187-198.
4. Reiber JHC, Tuinenburg JC, Koning G, et al. Quantitative coronary arteriography. In: Coronary Radiology 2nd Revised Edition, Oudkerk M, Reiser MF (Eds.), Series: Medical Radiology, Sub series: Diagnostic Imaging, Baert AL, Knauth M, Sartor K (Eds.). Springer-Verlag, Berlin-Heidelberg, 2009:41-65.
5. Lansky A, Tuinenburg J, Costa M, et al., on behalf of the European Bifurcation Angiographic Sub-Committee. Quantitative Angiographic methods for bifurcation lesions: A consensus statement from the European Bifurcation Group. Cath Cardiovasc Interventions 2009; 73:258-266.
6. Janssen JP, Rares A, Tuinenburg JC, Koning G, Lansky AJ, Reiber JHC. New approaches for the assessment of vessel sizes in quantitative (cardio-)vascular X-ray analysis. Int J Cardiovasc Imaging 2010; 26:259-271.
7. Tuinenburg JC, Koning G, Rares A, Janssen JP, Lansky AJ and Reiber JHC. Dedicated bifurcation analysis: basic principles. Int J Cardiovasc Imaging 2010; 26:169-174.
8. Collet C, Costa RA and Abizaid A. Dedicated bifurcation analysis: dedicated devices. Int J Cardiovasc Imaging 2010; 26:181-188.
9. Steigen TK, Maeng M, Wiseth R, et al.; Nordic PCI Study Group. Randomized study on simple versus complex stenting of coronary artery bifurcation lesions: The Nordic bifurcation study. Circulation 2006; 114:1955-1961.
10. Holm NR, Højdahl H, Lassen JF, Thuesen L, Maeng M. Quantitative Coronary Analysis in the Nordic Bifurcation Studies. Int J Cardiovasc Imaging 2011; 27:175-180.
11. Ng VG, Lansky A. Novel QCA methodologies and angiographic scores. Int J Cardiovasc Imaging 2011; 27:157-165.
12. Tu S, Huang Z, Koning G, et al. A novel three-dimensional quantitative coronary angiography system: in vivo comparison with intravascular ultrasound for assessing arterial segment length. Catheter Cardiovasc Interv 2010; 76:291–298.
13. Koning G, Hekking E, Kemppainen JS, et al. Suitability of the Cordis StabilizerTM marker guide wire for quantitative coronary angiography calibration: an in vitro and in vivo study. Catheter Cardiovasc Interv 2001; 52:334–341.
14. Dumay ACM. Image reconstruction from biplane angiographic projections. Dissertation 1992, Delft University of Technology, the Netherlands.
15. Wahle A, Wellnhofer E, Mugaragu I, et al. Assessment of diffuse coronary artery disease by quantitative analysis of coronary morphology based upon 3-D reconstruction from biplane angiograms. IEEE Trans Med Imaging 1995; 14:230–241.
16. Costa MA, Angiolillo DJ, Tannenbaum M, et al. Impact of stent deployment procedural factors on longterm effectiveness and safety of sirolimus-eluting stents (final results of the multicenter prospective STLLR trial). Am J Cardiol 2008; 101:1704–1711.
17. Tu S, Hao P, Koning G, et al. In-vivo assessment of optimal viewing angles from X-ray coronary angiograms. EuroIntervention 2011; 7:112-120.

18. Tu S, Jing J, Holm NR, Onsea K, Zhang T, Adriaenssens T, Dubois C, Desmet W, Thuesen L, Chen Y, Reiber JHC. In-vivo Assessments of Bifurcation Optimal Viewing Angles and Bifurcation Angles by Three-dimensional (3D) Quantitative Coronary Angiography. Int J Cardiovasc Imaging 2011. Epub Ahead of Print. DOI: 10.1007/s10554-011-9996-x.
19. Hassoon M, De Belder A, Saha M, Hildick-Smith D. Changing the coronary bifurcation angles after stenting procedures: the relevance to the technique and unfavorable outcome (Three-dimensional analysis). Minerva Cardioangiol 2011; 59:309-319.
20. Tu S, Holm NR, Holm NR, Koning G, Maeng M, Reiber JHC. The impact of acquisition angle difference on three-dimensional quantitative coronary angiography. Catheter Cardiovasc Interv 2011; 78:214-222.
21. Tu S, Holm NR , Koning G, Huang Z, Reiber JHC. Fusion of 3D QCA & IVUS/OCT. Int J Cardiovasc Imaging 2011; 27:197-207.
22. Tu S, Xu L, Ligthart J, Xu B, Witberg K, Sun Z, Koning G, Reiber JHC, Regar E. In-vivo Comparison of Arterial Lumen Dimensions Assessed by Co-registered Three-dimensional (3D) Quantitative Coronary Angiography, Intravascular Ultrasound and Optical Coherence Tomography. Int J Cardiovasc Imaging 2012. Epub Ahead of Print. DOI: 10.1007/s10554-012-0016-6.
23. Lemos PA, Saia F, Ligthart JM, et al. Coronary restenosis after sirolimus-eluting stent implantation: morphological description and mechanistic analysis from a consecutive series of cases. Circulation 2003; 108:257–260.
24. Stone GW, Moses JW, Ellis SG, et al. Safety and efficacy of sirolimus- and paclitaxel-eluting coronary stents. N Engl J Med 2007; 356:998–1008.
25. Fujii K, Carlier SG, Mintz GS, et al. Stent underexpansion and residual reference segment stenosis are related to stent thrombosis after sirolimus-eluting stent implantation: An intravascular ultrasound study. J Am Coll Cardiol 2005; 45:995–998.
26. Finn AV, Kolodgie FD, Harnek J, et al. Differential response of delayed healing and persistent inflammation at sites of overlap sirolimus- or paclitaxel-eluting stents. Circulation 2005; 112:270–278.
27. Colombo A, Stankovic G, Moses JW. Selection of coronary stents. J Am Coll Cardiol 2002; 40:1021–1033.

CHAPTER 2

Coronary Angiography Enhancement for Visualization

This chapter was adapted from:

Coronary angiography enhancement for visualization.
Shengxian Tu, Gerhard Koning, Joan C. Tuinenburg, Wouter Jukema,
Su Zhang, Yazhu Chen, Johan H.C. Reiber
International Journal of Cardiovascular Imaging. 2009,
Volume 25, issue 7, Pages 657–667.

ABSTRACT

High quality visualization of X-ray angiographic images is of great significance for the diagnosis of vessel abnormalities and for coronary interventions. Algorithms to improve the visualization of detailed vascular structures without significantly increasing image noise are currently demanded. A new algorithm called stick-guided lateral inhibition (SGLI) is presented to increase the visibility of coronary vascular structures. The validation study was set up to compare the SGLI algorithm with the conventional unsharp masking (UM) algorithm on 20 static angiographic images frames. Ten experienced QCA analysts and nine cardiologists from various centers participated in the validation. Sample scoring value (SSV) and observer agreement value (OAV) were defined to evaluate the validation result, in terms of enhancing performance and observer agreement, respectively. The mean of SSV was concluded to be 77.1% ± 11.9%, indicating that the SGLI algorithm performed significantly better than the UM algorithm (*P*-value < 0.001). The mean of the OAV was concluded to be 70.3%, indicating that the average agreement with respect to a senior cardiologist was 70.3%. In conclusion, this validation study clearly demonstrated the superiority of the SGLI algorithm for the visualization of coronary arteries from X-ray angiography.

Chapter 2

2.1 Introduction

Coronary angiography is a minimally invasive procedure that requires administration of a contrast agent via a catheter into the coronary arteries to visualize the inside by lumen [1]. It is performed during both diagnostic and interventional procedures. During the passage of the contrast agent through the coronary arteries, images are acquired with an angiographic X-ray system at 12.5 or more frames/s. Because of the low-pass characteristics of X-ray systems, the sharpness of the visualized coronary arteries is limited (images are blurred), which become less appreciated when zooming in the interesting parts of the image to observe its detailed structures. In certain cases, e.g., branching vessels or complex lesions, high quality visualization of certain anatomical information is of great significance for the diagnosis. Therefore, post image enhancement, a process by which the image is manipulated to achieve a better perception or interpretability of the information in the image, could assist cardiologists in appreciating the finer details of the coronary anatomy.

There are several factors in the area of angiographic image enhancement which have been widely accepted by general cardiologists:

1) The image enhancement is used for visualization purposes only, and not for quantitative analysis. Possible effects of image enhancement on the accuracy and precision of quantitative coronary angiography (QCA) have been investigated [2]. A definite effect was clearly demonstrated, especially for QCA on vessels with smaller diameters (<1.2 mm). Therefore, it is advisable that enhancement be used for visualization purposes only, and that the original images are kept for archiving and quantitative analysis purposes.
2) Detailed image structures should not be lost during the enhancing procedure. Achieving nice appearance and contrast at the sacrifice of losing some detailed information is not acceptable. Image enhancement is expected to improve the visibility of vascular structures with diagnostic value. Therefore, image details should not "disappear" after enhancement.
3) The original dimensions of vascular structures should be preserved in the enhanced image. Any change of the dimensions, e.g., overestimation or underestimation of arterial diameters, could introduce a twisted interpretation, resulting in an inappropriate clinical decision.

The literature on enhancing X-ray coronary angiographic images for visualization purposes is very limited. Although a number of algorithms have been proposed for angiographic image enhancement, the purpose of most algorithms is to improve subsequent segmentation rather than visualization. These algorithms can hardly be adopted in clinical practice to improve visualization quality because of the aforementioned factors. Algorithms based on specific noise models, e.g., quantum noise model [3], might also fail to work in practice since image noise, i.e., the undesirable appearance of mottled or grainy spots which do not reflect

true tissue property, is the hybrid of various sources of noise with different characteristics. Attempting to increase the contrast of vascular structures by suppressing or removing background structures, e.g., the piecewise normalization [4], the rolling algorithm [5], are also of limited effect, since parts of image noise with intensity value within the range of foreground (vascular structures) will be enhanced as well. The step of removing the background might at the same time remove some detailed information in low contrast angiographic images, which is very undesirable.

To the best of the authors' knowledge, all angiographic acquisition systems available on the market use a certain technique to enhance the acquired images in real time, i.e. during the actual acquisition procedure. Most of these enhancement techniques are based on the so-called unsharp masking technique, and allow the operators to customize the degree of enhancement by using multiple gain levels (typically 5). The unprocessed image is first blurred and subtracted from the original image, creating an edge image that only contains the higher spatial frequency components of the original image. This edge image is further multiplied by a certain gain level and added to the original image, resulting in an edge enhanced image [2]. Although image edges are visually enhanced, the result is less optimal since image noise with high spatial frequency will also be enhanced, which might introduce undesirable appearance or influence the perception of the image details.

We have been very interested in developing a technique for enhancing image details without the aforementioned negative effects, e.g., the increase of noise level. A new nonlinear enhancement model, which is called stick-guided lateral inhibition (SGLI), is presented in this paper to improve the visualization of vascular structures, in particular for coronary arteries. The proposed model simulates the enhancing mechanisms integrated in the eyes of human beings and of many animals. By integrating asymmetric sticks as a main tool to approximate vessel edges information for guiding the inhibition process, it has the ability to accentuate the intensity gradients of interesting vessel edges, while suppressing the increase of noise. In this paper the performance of SGLI is compared with the unsharp masking (UM) algorithm implemented on the Philips Digital Cardiac Imaging (DCI) System (Philips Medical Systems, Best, the Netherlands) [2]. In the following sections, the methodological background will be presented, as well as the clinical materials, the set up of the validation study, followed by the presentation of the results, the discussions and the conclusions.

2.2 METHODS

2.2.1 Original lateral inhibition model

The earliest phases of the visualization process in the human being begin in the retina. Signals resulting from light falling on the photoreceptors are first processed by various interactions among retinal neurons, of which the lateral inhibition network is an instance. The retinal neurons receive excitatory input from overlying photoreceptors as well as inhibitory inputs from adjacent illuminated photoreceptors to shape the signals and pass them on by optic nerve to higher visual centers. It is the laterally spread inhibition feature that gives "lateral inhibition" networks their name [6]. Figure 2-1 is a schematic diagram illustrating how lateral inhibition functions in the retina. Green bars represent photoreceptors, which function as signal generators according to the amount of light falling on them. Red circles represent output neurons, which integrate excitatory input signals from overlying photoreceptors (indicated by solid vertical lines) and inhibitory input signals from adjacent photoreceptors (indicated by dash diagonal lines). The output will be passed on to higher visual centers. This phenomenon was first observed and investigated in the eye of the Limulus [7-10]. It has been shown that the interactions among the receptor units (ommatidia) in the eye of the Limulus are predominantly inhibitory and obey simple linear relationships [9].

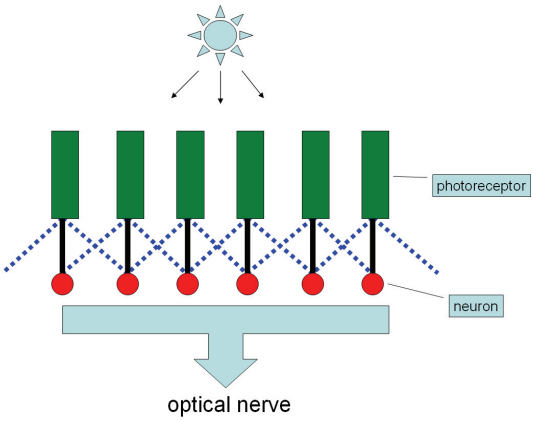

Figure 2-1. Lateral inhibition network (only the inhibition from the direct neighbors is indicated for illustration purposes)

One important function of the inhibitory interactions in the retina is contrast enhancement. On the image edge where the illumination changes, the inhibition from receptor units at the brightly lit side outweighs the inhibition from receptor units at the dimly lit side, resulting in different decreases of signal at two sides. In addition, receptor units are

deployed spatially and the strength of their interaction depends on their separation: the inhibition generally decreases as the distance of interacting units increases. Hence, adjacent receptor units exert a stronger inhibition on each other than distant units, the discrepancy of activities among adjacent receptors, especially for those units around the edge, increases. Such mechanism has been widely adopted in enhancing image edge contrast. An example is given by Figure 2-2. A and B represent dimly and brightly lit areas, respectively. E is the image edge. Clearly, the contrast of the image edge increases after inhibition.

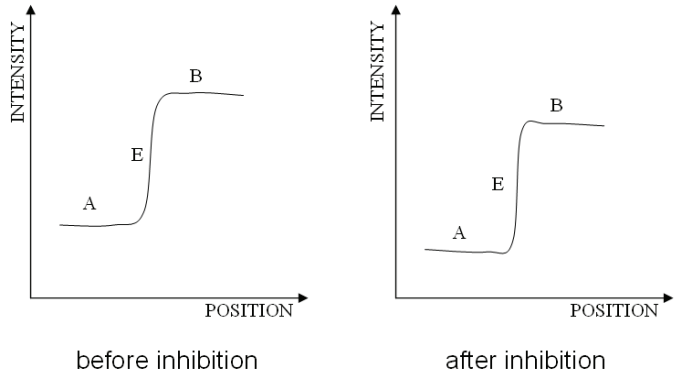

Figure 2-2 Image contrast enhancement by lateral inhibition model

Despite of its simplicity, the original lateral inhibition model has limited capacity in enhancing low contrast images due to its sensitivity to image noise. The model needs some "guidance" in order to work effectively on low contrast X-ray images.

2.2.2 Stick-guided lateral inhibition

The most challenging part of the guiding procedure is to distinguish vascular structures from image noise. Once an acceptable estimation of vessel edges is achieved, the contrast of vascular structures can be improved without increasing image noise in homogenous regions, e.g., background and lumen. In one of our papers [11], we used asymmetric sticks as a tool to perform the task of estimating image edges in a noisy background. Each stick is a digital line with certain direction. Since vessel edges can be decomposed into multiple digital lines, certain combinations of sticks could be used to approximate edges information.

The stick technique for image processing was first proposed by Czerwinski et al. [12, 13] and further extended by Xiao et al. [14] by introducing asymmetric sticks. Compared with symmetric sticks, asymmetric sticks can better approximate image edges, since image edges, especially for the curved parts of edges, are generally asymmetric.

Figure 2-3 shows an asymmetric stick filtering kernel with a length of 4. Given the stick length as *L*, a stick filtering kernel contains 8*L*-*L* different asymmetric sticks with the same starting point, the center of each squared panel.

By increasing angular resolution, the stick filtering kernel is able to detect digital edges with different directions. Statistical features along these sticks are used in the SGLI model to approximate vessel edges information. Based on the edges information, the degree of inhibition will change adaptively for each image point. The proposed SGLI model optimizes the enhancement of vessel edges by avoiding enhancing image noise.

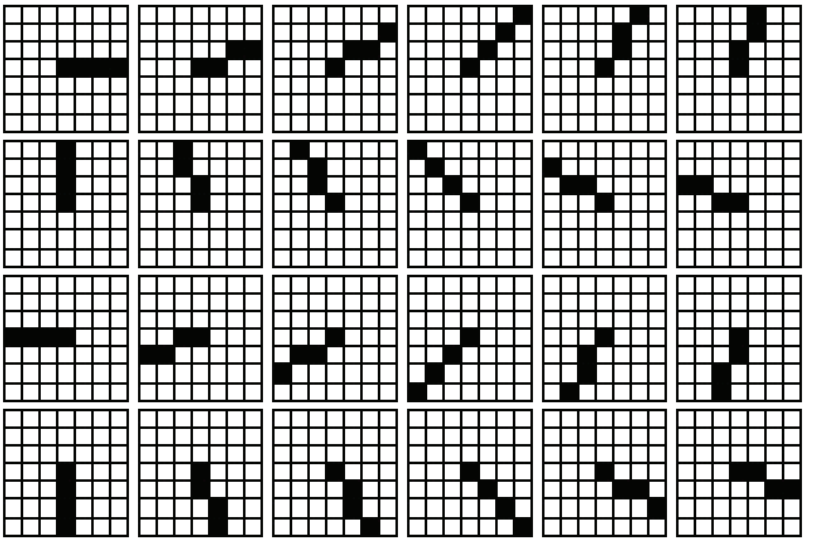

Figure 2-3. Asymmetric stick filtering kernel with length of 4

Figure 2-4 shows the enhancement results by different lateral inhibition models. Figure 2-4 (a) is the original angiographic image (only part of the image is shown). The image is a bit blurred. The lesion near the bifurcation is not clearly visible. Figure 2-4 (b) shows the enhanced result by the original lateral inhibition model. Although the visibility of vascular structures increases, the improvement is moderate. To enhance the detailed information further, a guided inhibition term (GIT) was introduced as a general framework to improve the performance of the lateral inhibition model [11]. The GIT used the edge properties of the image point with respect to its neighbors to adjust the degree of enhancement for that specific image point. The properties could be simply assigned as fixed values (without guidance) or obtained by statistical estimation using the stick filtering kernel (with sticks guidance). Figure 2-4 (c) and (d) show the results of enhancement by implementing GIT without guidance and with sticks guidance, respectively. Clearly, vessel

edges in both enhanced images look sharper than those in the previous versions. The lesion near the bifurcation is better visualized and appreciated. However, the enhancement algorithm without guidance apparently increases the noise level, resulting in a lot of undesirable grainy spots. On the contrary, SGLI significantly enhances the visualization of the vascular structures, while keeping the noise at a low level. Therefore, the quality of visualization improves.

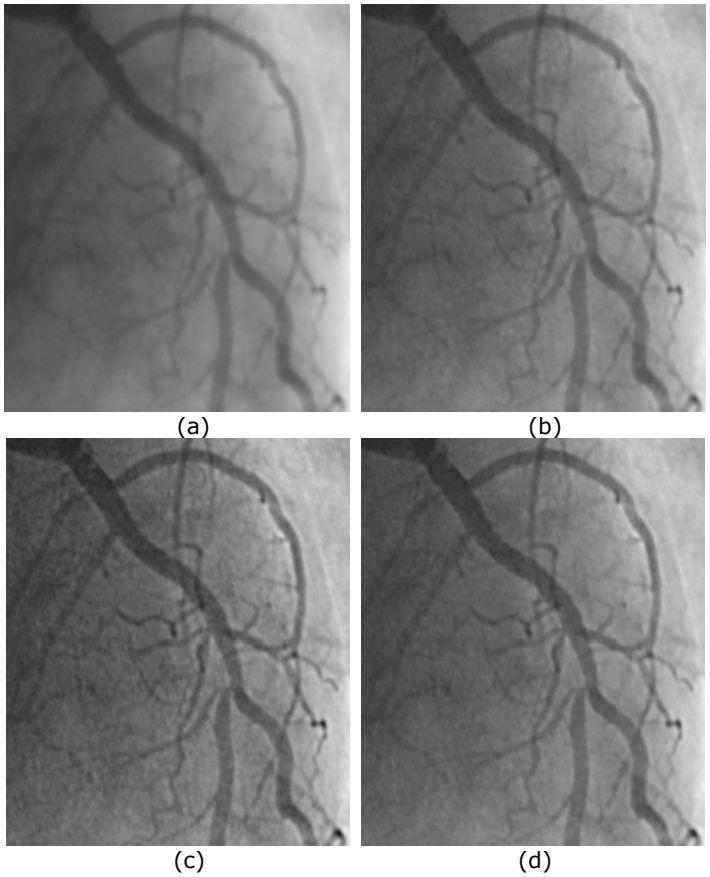

Figure 2-4. Angiographic image enhancement by lateral inhibition models: (a) is the original image; (b) is the result of enhancement by the original lateral inhibition model; (c) is the result of enhancement by the improved lateral inhibition model without guidance; (d) is the result of enhancement by stick-guided lateral inhibition model.

2.2.3 Validation

At the Leiden University Medical Center, routinely acquired coronary angiographic images with different noise levels from 15 patients were selected from the typical clinical databases; images were acquired by the Philips Cardiac Integris systems with 512×512 image resolution; critical information related to patients had been made anonymous before the

validation. 20 static angiographic image frames at different phases of cardiac circle with clinically relevant information were selected from the datasets by experts for the validation.

The validation study was to compare the performance of SGLI and UM algorithms on the selected 20 static image frames. 19 participants including 10 QCA analysts and 9 cardiologists from 5 hospitals in the Netherlands, Japan, Brazil, China, and America participated in the validation. For each image frame, SGLI and UM were applied with the same level of enhancement, which was set by the experts for optimally visualizing the images. The enhanced versions by SGLI and by UM with the same region and zooming factor were grouped into one image pair and incorporated into a PowerPoint slide. Each slide showed the SGLI enhanced version and the UM enhanced version with the same level of enhancement. Figure 2-5 shows an example of the prepared PowerPoint slide. The left-right position of these two enhanced images was randomly set, i.e., the left image could be the SGLI enhanced version or the UM enhanced version. Therefore, the participants were blind to the enhancement algorithm undertaken by each individual image.

In the scoring procedure, the participants were asked to indicate that which image (the left image or the right image) in each slide is the better enhanced image. Given the fact that there is no gold standard for evaluating the quality of visualization, we chose the following three features to be considered as a good enhancement result:

1) Enhance the detailed information which could increase the real diagnostic value.
2) Enhance the sharpness of vessel edges which could improve the contrast of the vascular structures.
3) Keep the noise as low as possible so that interesting information is easier to be appreciated and the enhanced image looks more pleasant.

It is our belief that the ability to visualize more detailed information should be the first priority for an enhancement algorithm, followed by the reduction of efforts in interpreting the interesting information, and then the pleasant appearance of the image content. Therefore, the following steps were set up to approach the scoring procedure:

Step 1: Look thoroughly at two enhanced images in the same slide. Choose the image with clearer and more detailed information as the better image.

Step 2: If there is no difference in the detailed information between two enhanced images, then the image with sharper vessel edges is the better image.

Step 3: If there is still no difference on the edges sharpness between two enhanced images, then the image with less noise should be the better image.

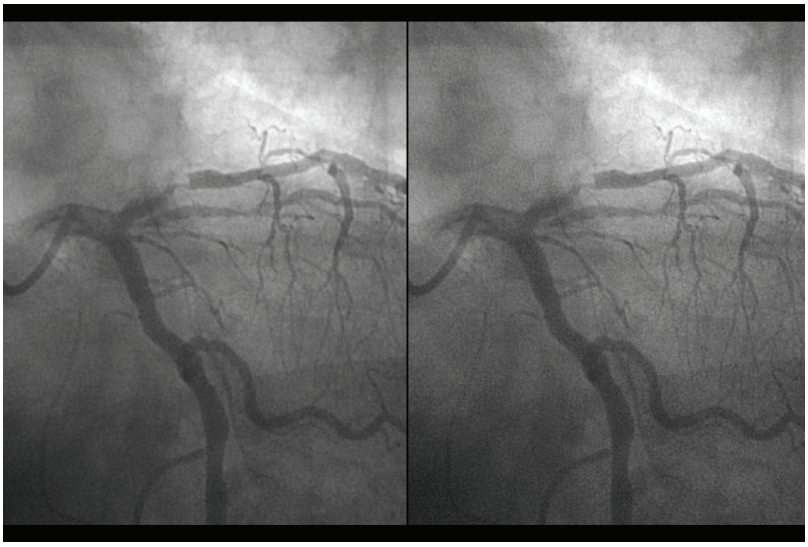

Figure 2-5. A grouped image pair for the comparison of SGLI with UM.

2.3 Statistics

After the scoring procedure, the results were mapped into 2 categories:

Category A: The SGLI enhanced version is better than the UM enhanced version.

Category B: The UM enhanced version is better than the SGLI enhanced version.

Based on the mapping results, two parameters, the sample scoring value (SSV) and the observer agreement value (OAV), in terms of enhancing performance and observer agreement, respectively, are defined to evaluate the scoring result.

1) The SSV is defined by the percentage of observers (participants) belonging to Category A and is calculated for each sample (slide). The mean of the SSV was computed and considered to be an index to the superiority of the SGLI enhancement algorithm with respect to the UM algorithm. 50% represents equal performance between these two algorithms. SSV above 50% indicates that the SGLI algorithm is better and SSV below 50% indicates that the UM algorithm is better. One-sample t-test was performed to investigate whether the mean of SSV is significant different from the 50% value.
2) The OAV is defined by the percentage of agreement between one senior cardiologist and the other observers and is calculated for each observer except for the senior cardiologist. The senior cardiologist with an extensive experience in interventional cardiology was thus defined to be the gold standard against whom the others were compared. The

mean of OAV represents the average agreement with respect to the senior cardiologist.

All statistical analyses were carried out by using statistical software (SPSS, version 16.0; SPSS Inc; Chicago, IL, USA).

2.4 RESULTS

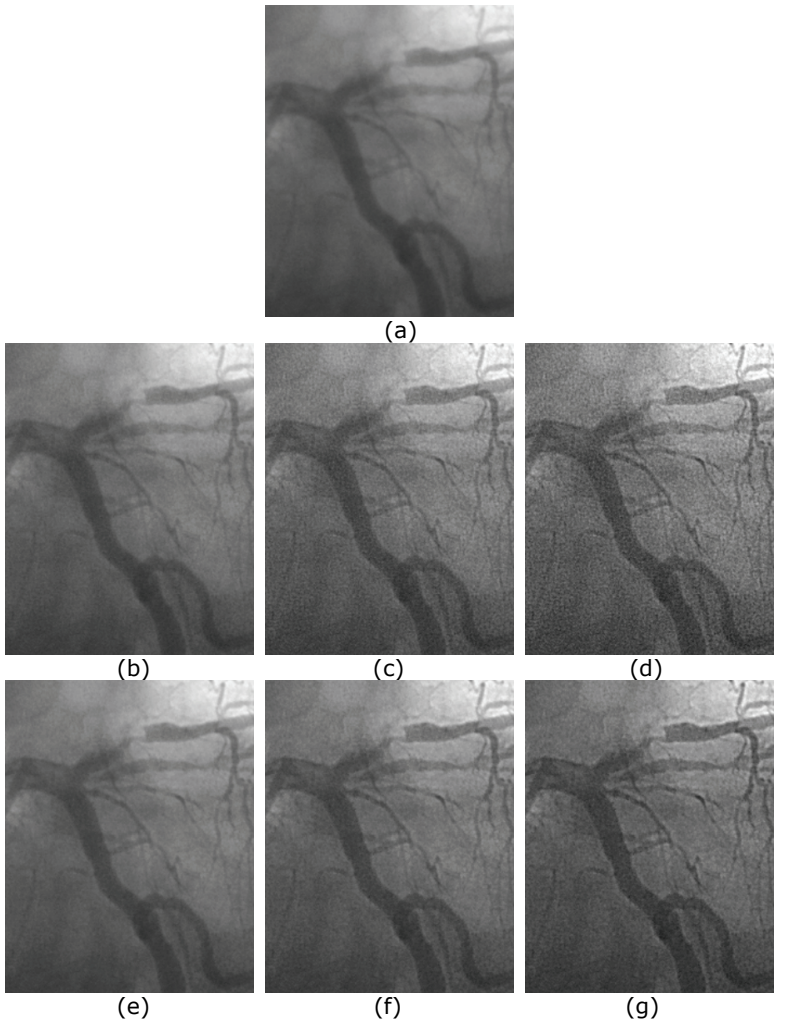

Figure 2-6. Comparisons of SGLI and UM on one angiographic image: (a) is original angiographic image; (b)~(d) are the images enhanced by UM with gain level 1, 3, and 5; (e) ~(g) are the images enhanced by SGLI with gain level 1, 3, and 5.

2.4.1 Visual interpretation

The proposed SGLI algorithm was compared with the UM algorithm available as the enhancement algorithm on the Philips Digital Cardiac

Imaging System [2]. We set 5 gain levels of enhancement for the SGLI algorithm to make it comparable to the UM algorithm. An example of comparison between these two algorithms is given by Figure 2-6. (a) is the original angiographic image. (b)~(d) show the images enhanced by the UM algorithm with the lowest, median, and highest gain level, respectively. With the increasing amount of enhancement, the edges of vascular structures look sharper and sharper. However, image noise also increases significantly. A lot of grainy spots appear in both lumen and background on the enhanced images. (e)~(g) shows the images enhanced by the SGLI algorithm with the lowest, median, and highest level, respectively. With the increasing amount of enhancement, vascular structures also become clearer and clearer while image noise increases slightly. Therefore, the enhancement result is more appreciated. At lower levels of enhancement, the difference between these two algorithms is moderate, although the vessel edges in the SGLI enhanced image still look a bit sharper. At higher levels of enhancement, the difference becomes quite obvious.

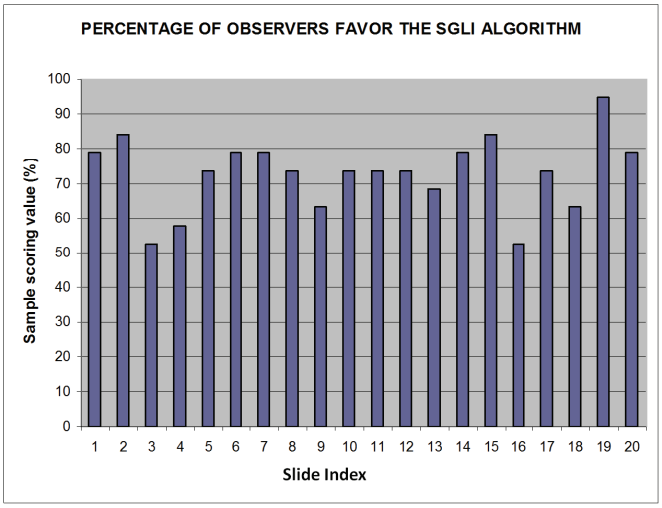

Figure 2-7. The sample scoring value for each sample

2.4.2 Quantitative results

The value of SSV for each sample is given by Figure 2-7. The mean of SSV is 77.1%, with a standard deviation of 11.9%. There is significant difference between the mean of SSV and the 50% value (*P*-value < 0.001), indicating that the observers showed significant preference for the SGLI enhanced images.

Figure 2-8 shows the OAV for each observer. The mean of the OAV is 70.3%, indicating that in average the observers agree with the senior cardiologist on 70.3% of the scoring samples. The large range of OAV

(from 35.0% to 85.0%) indicates that there is large variance in the interobserver agreement, mainly due to the subjectivity of the scoring procedure.

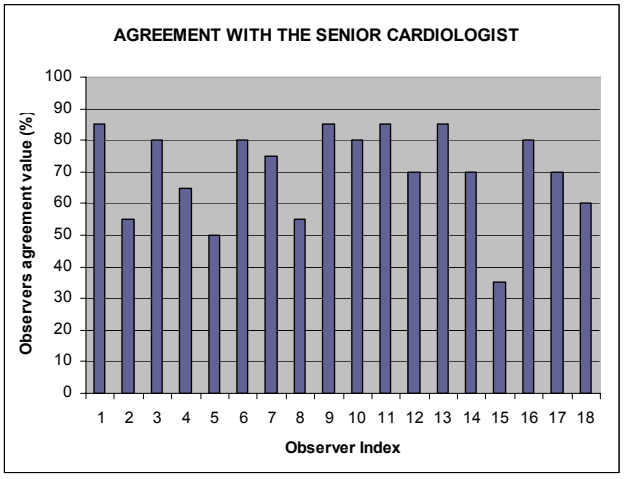

Figure 2-8. The observer agreement value for each observer

2.5 Discussions

X-ray angiography is one of the standard procedures for the diagnosis of coronary artery disease. Image enhancement is of great significance to the visual interpretation of vessel abnormalities. However, due to the low contrast property of angiographic images, image enhancement is not a trivial task when strong noise is present. High accuracy in distinguishing interesting objects, e.g., lesions and sidebranches, from background can be extremely difficult in some situations. Therefore, enhancing vessel edges by suppressing background or removing background might lose some detailed information, which is very undesirable. Enhancing the whole image content might also decrease the quality of visualization due to the increase of noise level.

One of the widely recognized mechanisms in the eyes of most animals (including humans) for outlining important visual structures is the so-called "lateral inhibition network". While it has great advantage of simplicity, it is not "intelligent" enough to differentiate the noise with the true anatomical structures. Therefore, enhancement is less optimal when applied to the low contrast angiographic images. The asymmetric sticks, which have better characteristics to fit the patterns of digital image edges, could be used to improve the lateral inhibition models. Instead of removing or suppressing background information to gain better visualization, more efforts have been put on distinguishing vascular structures from background and lumen by the integration of the stick

filtering kernel. The algorithm has lower risks of removing detailed information and increasing noise level when enhancing detailed vascular structures in low contrast angiographic images.

Image details contribute in utter most importance to the visualization of vascular structures. However, despite many cardiologists share common opinions about the principles underlining the good visualization, there is no gold standard to evaluate the visualization quality. Enhancing detailed information in low contrast images will inevitably increase image noise, which is not always appreciated, especially when the image noise increase significantly. The presence of strong image noise will introduce additional efforts in interpreting the interesting information, especially when the cardiologists quickly review the angiographic image sequences for the entire cardiac cycle. On the other hand, reducing noise will potentially result in loss of some details. There is always a trade-off between enhancing details and reducing noise. The ultimate goal would be to enhance details to the desired quality while keeping the noise at an acceptable level. However, preference of details and tolerance of noise vary among different observers. In addition, it is extremely difficult to define detailed information under certain circumstances. Noise might be accidently treated as information since its presence could create a sense of "details", especially when observers get used to look at the noisy grainy spots in the images. This phenomenon was confirmed by some of the participants in the follow-up discussions after they finished the scoring. It could partly explain the reason why some observers favor the UM algorithm, since they were used to looking at the images with noisy spots. This phenomenon, together with the subjectivity in step 2 of the scoring procedure, i.e., the judgment of the sharpness of vessel edges, accounts for the big variance in interobserver agreement. On the other hand, despite of all the subjectivities involved, the validation study clearly demonstrated that the participants were in favor of the SGLI enhancement algorithm, mainly due to the reason that the relatively low noise level in the enhanced images improved the visualization quality and saved the efforts in the diagnosis. Although we have not validated the algorithm on cine clips, i.e., running movie, we believe that the relative low noise level and clear image details achieved by the SGLI algorithm could potentially reduce the time in examining the whole image sequence and spot more interesting information. Therefore, cardiologists could show more preference to the SGLI algorithm when making quick decisions based on the cine clips.

The majority of the computation cost for the proposed algorithm is to calculate the average intensity and variance along each stick for all image points. Current implementation by using C++ language has achieved a

speed of 0.09 second per image frame on a Windows PC with 3.0 GHz Core 2 Duo CPU and 2.0 GB RAM. Since each stick in the stick filtering kernel is independent, parallel computing techniques can be applied to further accelerate the algorithm.

One limitation to this study is that all angiographic images used for the validation study were acquired by the same X-ray angiographic system. The quality of angiographic images varies among different X-ray systems and is subject to the acquisition condition, which might influence the enhancement results. However, since the SGLI algorithm does not depend on specific noise models and the validation study has already demonstrated its superiority on images with different noise levels, we expect that there will be similar results when applied to other X-ray angiographic systems.

2.6 Conclusions

The SGLI algorithm improves the visibility of detailed vascular structures in low contrast coronary angiographic images. The validation study demonstrates the superiority of the SGLI algorithm, compared with the conventional unsharp masking algorithm.

2.7 References

1. Reiber JHC, Koning G, Dijkstra J, Wahle A, Goedhart B, Sheehan FH, Sonka M. Angiography and Intravascular ultrasound In: M. Sonka, J. M. Fitzpatrick (ed) Handbook of Medical Imaging, Volume 2. Medical Image Processing and Analysis. SPIE, Washington, 2000, pp 711-808.
2. van der Zwet PMJ, Reiber JHC. The influence of image enhancement and reconstruction on quantitative coronary arteriography. Int J Cardiovasc Imaging 1995; 11: 211-221.
3. Aach T, Schiebel U, Spekowius G. Digital Image Acquisition and Processing in Medical X-Ray Imaging. Journal of Electronic Imaging 1999; 8: 7-22.
4. Kumar MSD, Wei L, Turlapthi R, Suri JS. DSA image enhancement via multi-resolution motion correction for interventional procedures: a robust strategy. Proceedings of the fifth IASTED International Conference: biomedical engineering. Innsbruck, Austria: ACTA Press, 2007.
5. Wilson DL, Kaplan EJ. Linear and Morphological Digital Image Enhancement of Peripheral Angiography Images. Proceedings of SPIE: Medical Imaging IV: Image Processing. Newport Beach, USA, 1990.
6. Grobstein P. Tricks of the Eye, Wisdom of the Brain. Serendip. 2003. Available via webpage. http://serendip.brynmawr.edu/bb/latinhib.html. accessed 12 September 2008
7. Hartline HK. Inhibition in the eye of Limulus. Journal of General Physiology 1956; 39:651-673.
8. Hartline HK, Knight Jr BW. The processing of visual information in a simple retina. Annals of the New York Academy of Sciences 1974; 231:12-18.
9. Hartline HK. Visual receptors and retinal interaction. Science 1969; 164:270-278.
10. Lange D, Hartline HK, Ratliff F. Inhibitory interaction in the retina: techniques of experimental and theoretical analysis. Annals of the New York Academy of Sciences 1966; 128:955-971.

11. Tu S, Wu Y, Lu X, Huo H, Fang T. Stick-guided lateral inhibition for enhancement of low-contrast image. Proceedings of SPIE: MIPPR 2007: Pattern Recognition and Computer Vision. Wuhan, China.
12. Czerwinski RN, Jones DL, O'Brien Jr WD. Line and boundary detection in speckle images. IEEE Transactions on Image Processing 1998; 7:1700-1714.
13. Czerwinski RN, Jones DL, O'Brien Jr WD. Detection of lines and boundaries in speckle images - application to medical ultrasound. IEEE Transactions on Medical Imaging 1999; 18:126-136.
14. Xiao C, Su Z, Chen Y. A diffusion stick method for speckle suppression in ultrasonic images. Pattern Recognition Letters 2004; 25:1867-1877.

CHAPTER 3

Assessment of Obstruction Length and Optimal Viewing Angle from Biplane X-ray Angiograms

This chapter was adapted from:

Assessment of obstruction length and optimal viewing angle from biplane X-ray angiograms.
Shengxian Tu, Gerhard Koning, Wouter Jukema, Johan. H.C. Reiber
International Journal of Cardiovascular Imaging. 2010,
Volume 26, Issue 1, Pages 5–17.

ABSTRACT

Three-dimensional quantitative coronary angiography (3D QCA) has been encouraged by the increasing need to better assess vessel dimensions for the diagnosis and for support of interventional procedures. A novel 3D QCA system based on biplane X-ray angiograms is presented in this paper. By correcting for the isocenter offset and by improving the epipolar constraint in the correspondence of the two angiographic projections, accurate and robust reconstruction of the vessel centerline is achieved and the reproducibility of its applications is guaranteed. The accuracy and variability in the assessment of obstruction length and bifurcation optimal viewing angle were investigated using phantom experiments. The segment length assessed by 3D QCA correlated well with the true wire segment length (R^2 = 0.999) and the accuracy was 0.04 ± 0.25 mm (P < 0.01). 3D QCA slightly underestimated the rotation angle (difference: -1.5º ± 3.6º, P < 0.01), while no significant difference was observed for the angulation angle (difference: -0.2º ± 2.4º, P = 0.54). In conclusion, the new 3D QCA approach allows highly accurate and precise assessments of obstruction length and optimal viewing angle from X-ray angiography.

3.1 Introduction

Accurate interpretation of vessel dimensions from X-ray angiography is of great importance to the diagnosis of cardiovascular diseases and to support coronary interventions. Two-dimensional quantitative coronary angiography (2D QCA) has been widely used to obtain clinically relevant parameters, e.g., obstruction length and diameter stenosis, and to assess the results of PCI-trials [1]. However, due to the perspective deformation of vessels on the projection images, 2D QCA has inherent limitations in interpreting the true dimensions of the vascular structures, resulting in an increasing interest in the research and development of three-dimensional quantitative coronary angiography (3D QCA) systems [2-6].

Restoring 3D morphology of the vascular structures requires at least two projections. Biplane angiograms supply a nice solution to the reconstruction problem by allowing two projections obtained at the same time. However, the 3D reconstruction from two projections is an underdetermined problem, allowing a huge number of feasible solutions which could satisfy the projection data [5]. In addition, mechanical distortions in the X-ray systems, as well as noise corruption in the projections, make the development of reliable and robust 3D QCA systems a non-trivial task.

The accuracy of 3D QCA systems mainly depends on the reconstruction of the vascular structures, of which the centerline reconstruction is the primary and yet the most important step. Once an acceptable solution for the 3D centerline has been obtained, the issue of reconstructing the cross-sections becomes relevant. To determine the exact position of the 3D centerline points, the correspondence between the two projected centerlines should be established first, mainly by using the epipolar constraint, i.e., the constraint between a projection point and its corresponding epipolar line, being the projection of the X-ray beam directed towards a particular point on one of the projection planes onto the second projection plane [5]. However, the isocenter offset, i.e., the spatial displacement of the isocenters in the frontal and lateral systems, together with the small perspective viewing angle, i.e. the angle between the epipolar line and the arterial centerline, for noise-corrupt arterial centerlines, could greatly deteriorate the epipolar constraint, leading to an inaccurate correspondence.

Many efforts [2-4, 6] have been undertaken to correct for the isocenter offset, either by manually or automatically identifying several reliable points, e.g., anatomical landmarks, as reference points on the two projections and involving the epipolar constraint [5] to approximate the isocenter offset. At least 5 to 8 pairs [3] or 2 to 5 pairs [7] of reference points were needed to approximate the isocenter offset. However, it may

be very difficult in routine clinical practice to find that many reliable reference points in the two projections, due to the presence of vessel foreshortening and overlap. In addition, requiring the user to indicate many reference points is not very attractive from a workflow perspective. To guarantee the accuracy and reliability in this interactive procedure has already been a difficult task.

We have been very interested in developing a fast and reliable system for the reconstruction of vascular centerlines from X-ray angiography. To minimize the number of reliable reference points in the correction of the isocenter offset and yet to achieve a good correspondence in the centerline reconstruction, we proposed to use one to three reference points for the correction of the isocenter offset. In case of the presence of small perspective viewing angles for noise-corrupt arterial centerlines, the usage of epipolar constraint was further improved by building a distance transformation matrix and subsequently by searching the optimal corresponding path in the matrix. The reconstructed vessel segments can then be used to assess obstruction (stenotic lesion) length and bifurcation optimal viewing angle. In the following sections, the methodology will be presented, followed by the applications of centerline reconstruction in assessing obstruction length and bifurcation optimal viewing angle; next, the validation approach will be described, followed by the results, the discussions and the conclusions.

3.2 Methods

3.2.1 Image geometry

The conventional biplane angiographic equipment consists of a frontal X-ray system and a lateral X-ray system. In theory, the frontal projection axis (central beam) intersects with the lateral projection axis into the so-called isocenter, and the whole X-ray system rotates around the isocenter. However, due to the system distortions caused by the gravity and mechanical influence, the isocenter could hardly be observed as a stable point [2]. Therefore, we define two isocenters, a frontal isocenter and a lateral isocenter, to explicitly model the biplane angiogram under that specific acquisition. When no system distortion is present, these two isocenters will coincide with each other. Otherwise, an isocenter offset is expected and this offset should be eliminated before the reconstruction of vascular centerlines.

Many sources of distortion might contribute to the isocenter offset, e.g., the gantry sag and the inaccurate reading of the acquisition angle. During many years of quality control on several X-ray systems at various hospitals, we found that gantry sag was the main reason leading to the

shift of the isocenter. Due to the gravity and mechanical influence, gantry sag constantly happens during the image acquisition when the acquisition angle is adjusted. For a monoplane system, rotating the gantry to a different acquisition angle could cause a significant shift of more than 20 mm to its isocenter [7]. For a biplane system, either the frontal gantry or the lateral gantry could sag significantly under circumstances. The gantry sags from the two systems could add up, resulting in a significant isocenter offset.

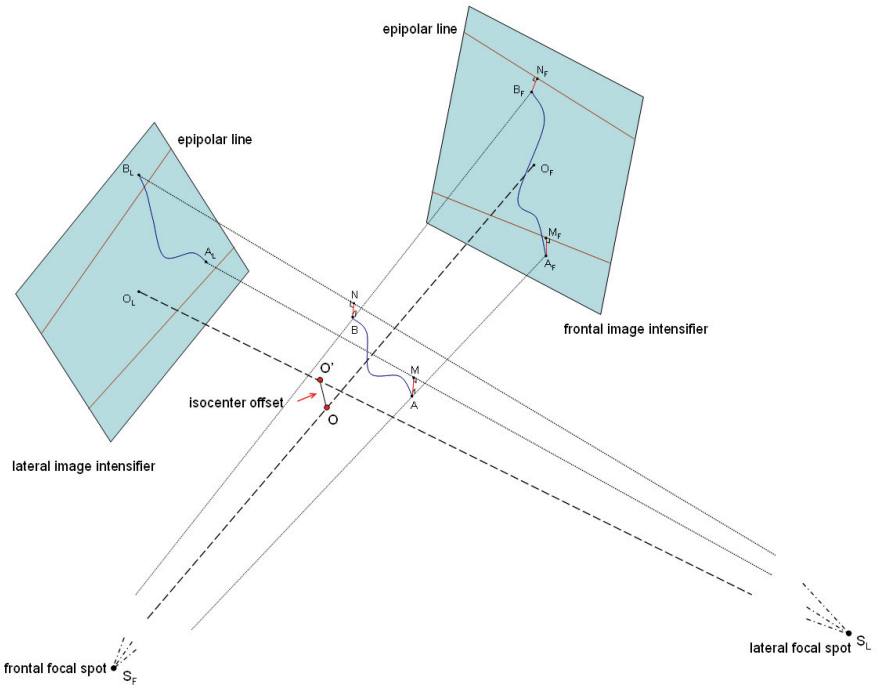

Figure 3-1. 3D biplane model with an isocenter offset

Given the aforementioned facts, we ignore insignificant sources of distortions and assume that the uneven gantry sag between the frontal X-ray system and the lateral X-ray system is the only reason accounting for the isocenter offset. By this assumption, we define the imaging geometry as one X-ray system in fixed position with a shift equal to the amount of the isocenter offset in the other X-ray system. Figure 3-1 shows our 3D biplane model with an isocenter offset O-O'. The system distortion can be examined by using the epipolar constraint [5]. Due to the absence of pincushion distortion in modern X-ray systems with digital image intensifiers, each projection point should intersect with its corresponding epipolar line, when no system distortion is present. However, due to the presence of the isocenter offset, the projection of reference point *A* in the

frontal image intensifier, A_F, does not intersect with its corresponding epipolar line. The same holds for the reference point *B*. This ill-defined epipolar constraint can significantly jeopardize its usage in establishing the correspondence of the two projections for the 3D centerline reconstruction.

3.2.2 Approximation of the isocenter offset

In order to create a good correspondence between the frontal and lateral centerlines, i.e., to enforce the centerline points to correctly intersect with their corresponding epipolar lines, the isocenter offset should be calculated and eliminated. Due to the uncertainty of gantry sag, the real amount of isocenter offset varies for different acquisitions and is not reproducible. Our solution is to use one to three pairs of reference points, chosen from the anatomical landmarks visualized on both projections, e.g., the bifurcations, to approximate the isocenter offset.

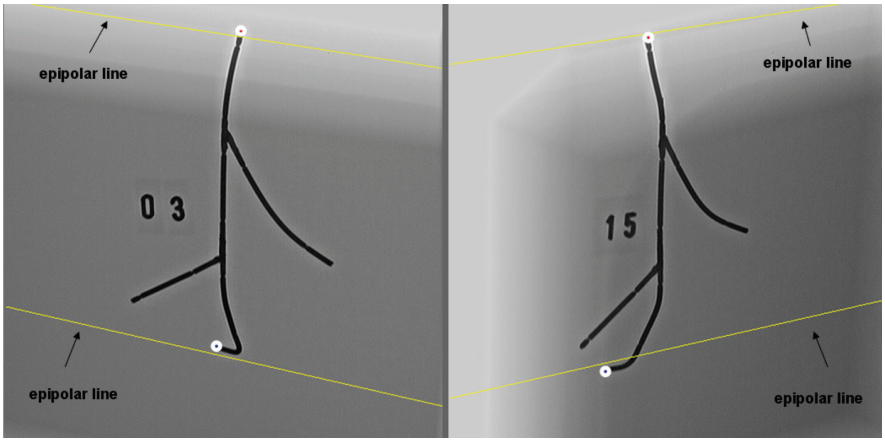

Figure 3-2. Correspondence before correcting for the isocenter offset

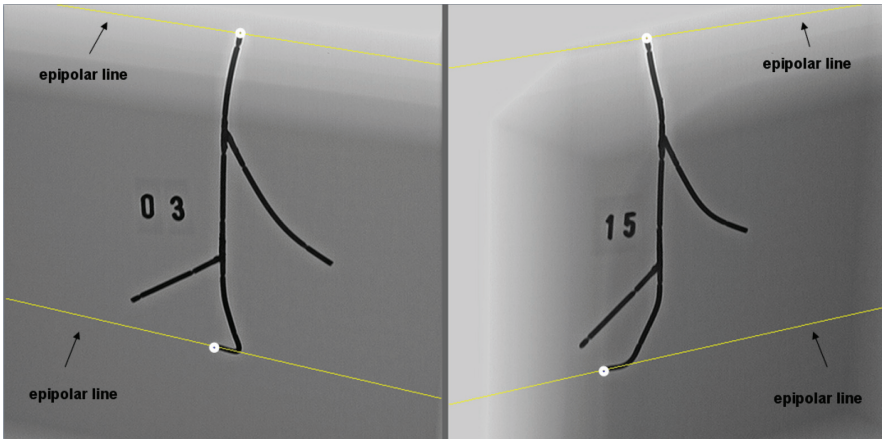

Figure 3-3. Correspondence after correcting for the isocenter offset

The error of approximation is defined as the total distance from the reference points to their corresponding epipolar lines, e.g., the $A_F M_F$ and $B_F N_F$ in Figure 3-1. By using the aforementioned biplane geometry, the error can be formulated as an explicit function of the isocenter offset. By minimizing the error function, the approximation of the isocenter offset is obtained. An example of correspondence before and after eliminating the isocenter offset is given by Figure 3-2 and Figure 3-3, respectively. Clearly, the reliability of the epipolar constraint [5] was improved and good correspondence between the two projections was established after the elimination of the isocenter offset.

3.2.3 Centerline reconstruction

The vascular centerline is defined in this paper as the curve that passes through the center of the vessel lumen. The accuracy of the centerline reconstruction depends both on the 2D centerline extraction and on the 3D point reconstruction. In our approach, the lumen contours are automatically detected by a validated contour detection algorithm [8] after manually specifying the start and end positions of the segment of interest on the two projections. 2D centerlines are then extracted from the contours and used to reconstruct the 3D centerline.

The 3D point reconstruction algorithm requires the knowledge of correspondence between the frontal and lateral centerlines. This knowledge can be facilitated by using the epipolar constraint [5]. However, an ill-defined epipolar line due to the system distortions could cause significant error in the correspondence. Multiple intersections of the projected centerline and the epipolar line, as well as noise corruption in the centerline, could further deteriorate the correspondence. An example of the possible difficulties in creating correspondence by using the epipolar constraint is given by Figure 3-4.

Two possible types of errors might exist in creating the correspondence between the frontal and lateral centerlines:

1) The first error comes from the ill-defined epipolar lines due to the system distortion, mainly the isocenter offset. The correction of the isocenter offset in our 3D model will allow more accurate usage of the epipolar constraint in creating the correspondence, e.g., the corrected epipolar lines of the start and end points in Figure 3-4 correspond better with the vessel centerline than the original epipolar lines.
2) The second error comes from the noise-corrupt arterial centerlines, especially for those images with low contrast and a small perspective viewing angle, e.g., epipolar line **a** in Figure 3-4, which could introduce quite cumbersome problems and affect the quality of correspondence.

To address the problems of using the epipolar constraint in difficult situations, a distance transform matrix is constructed based on the

distance from each projected centerline point to its corresponding epipolar line. A wave propagation algorithm [9] is then applied to search for a smooth corresponding path by which the propagation from the start position to the end position has the lowest cost. Based on the correspondence path, point reconstruction will be performed on based on the correspondence. We adopted the point reconstruction algorithm used by Dumay and Wahle [2, 5]. Each pair of corresponding points will generate two projection rays. The middle point of the shortest vector perpendicular to the two projection rays is used as the reconstruction point.

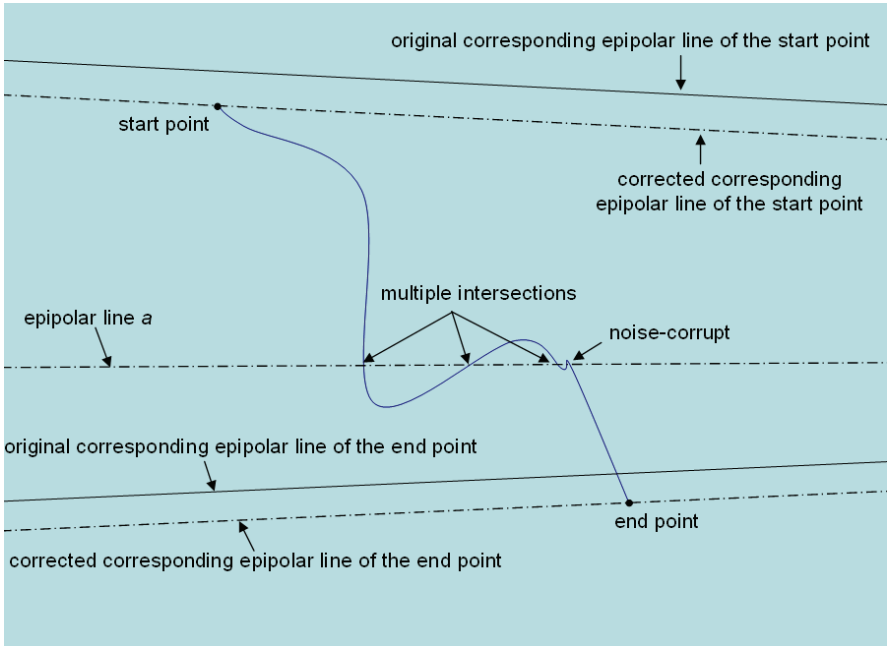

Figure 3-4. Possible difficulties in establishing the correspondence between the two centerlines by using the epipolar constraint.

3.3 Applications

3.3.1 Obstruction length assessment

In coronary interventions, accurate assessment of obstruction length is of utmost importance for the selection of the appropriate stent size. The conventional approach to calculate obstruction length is to perform 2D QCA on the end-diastolic image frame [1, 10]. After defining the start and end positions of the obstruction, the pixel length is calculated and multiplied with the calibration factor to generate the obstruction length. Since the calibration factor only holds true for one particular plane perpendicular to the projection axis, e.g., the catheter plane or isocenter

plane, and this procedure assumes that the obstructed vessel segment lies in that particular plane; significant error due to the out-of-plane magnification [11] could exist when the assumption is not satisfied during the image acquisition. Besides, due to the 2D representation of the 3D vascular structures, 2D QCA has inherent limitations in assessing curved/bended segment length due to vessel foreshortening. The amount of foreshortening in 2D QCA varies with the shape of vessel and the experience of the operators in choosing the so-called optimal viewing angle during the image acquisition. A significant vessel foreshortening by performing 2D QCA on the operator-selected view in standard clinical acquisitions has been reported in early literatures [12-14].

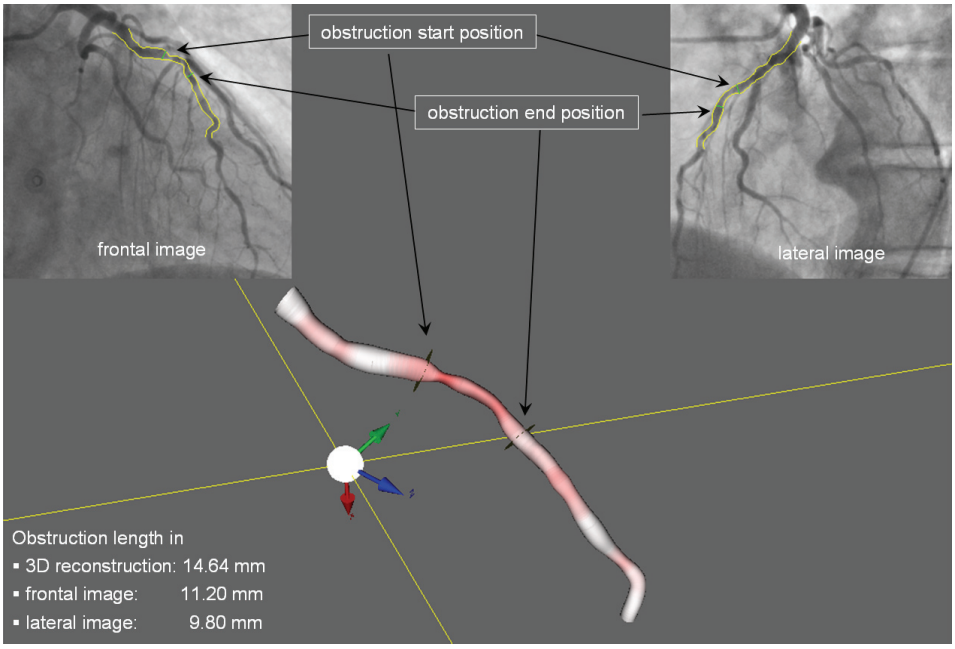

Figure 3-5. Comparison of 3D QCA and 2D QCA in assessing obstruction length: Frontal image (top left panel) and lateral image (top right panel) are biplane data. Courtesy: Department of Cardiology, Leiden University Medical Center (LUMC), the Netherlands.

Figure 3-5 shows an example of comparing 3D QCA and 2D QCA in assessing obstruction length. The centerline and cross-sections of the segment of interest were reconstructed from biplane data (frontal image under 28.7 RAO and 0.3 Cranial, lateral image under 49.2 LAO and 0.2 Cranial) and the obstructed segment was automatically detected. The start and end positions of the obstruction in frontal image, lateral image, and the 3D view were synchronized. 2D QCA was performed on both frontal and lateral images by using isocenter calibration method. A significant error, caused by vessel foreshortening and out-of-plane magnification, was noticed from the 2D QCA assessments: The obstruction

length was measured as 11.20 mm in the frontal image and 9.80 mm in the lateral image, respectively, while the 3D obstruction length was 14.64 mm. The error in the frontal image comes predominantly from the out-of-plane magnification, since the obstructed vessel segment does not lie in the frontal isocenter plane, i.e., the plane perpendicular to the frontal projection axis and passing through the isocenter (the white intersection point of two yellow lines in Figure 3-5). Since the obstructed segment is also not close to the catheter plane, the out-of-plane magnification would still cause significant error, if the catheter calibration method instead of isocenter calibration method was used. The error of 2D QCA in the lateral image is caused by the combination of out-of-magnification and vessel foreshortening, which is more significant in this case.

3.3.2 Bifurcation optimal viewing angle assessment

Due to the increasing complexity of coronary interventions, in particular for bifurcation lesions, the identification of the optimal viewing angle is of increasing importance to the interventionalists to optimally deploy the stent. To stent certain types of bifurcation lesions, e.g., the one classified as 0,1,0 according to the Medina classification [15], a suboptimal viewing angle might not entitle the interventionalists to clearly visualize the ostium, possibly resulting in jailing of the sidebranch [16]. In case of stenting the ostium of a sidebranch, a good viewing angle could help the interventionalists to prevent stent protrusion into the main vessel or incomplete lesion coverage at the ostium of the sidebranch [17].

In routine clinical practice, the optimal viewing angle is subjectively selected by adjusting the rotation angle (LAO/RAO) and the angulation angle (Cranial/Caudal) of the X-ray system. This "trial-and-error" approach could significantly increase the amount of contrast medium administration and the radiation exposure to the patient and staff. In addition, due to the various experiences and preferences of the interventionalists, there is no guarantee that the chosen angle will optimize the visualization of the segment of interest. Therefore, a number of automated methods have been developed to identify the optimal viewing angle after the 3D reconstruction. Chen et al [18] defined the optimal viewing angle as the projection view having minimum foreshortening and overlap of a specific region in angiographic images. However, in case of a bifurcation with strongly curved main (parent) vessel, the viewing angle minimizing the foreshortening of the main vessel is not always the same view optimizing the visualization of the ostium of a sidebranch, e.g., the left main bifurcation [16]. Besides, the choice of a specific region for calculating the foreshortening and overlap is also subjective. Christiaens et al. [19] followed the method of determining

optimal viewing angle for a straight vessel by Dumay et al. [20] and defined the bifurcation optimal viewing angle as the angle perpendicular to the main direction of the bifurcation branches. Again, in a heavily curved main vessel, the optimal view calculated by this approach might not optimal for the ostium of the sidebranch, where the majority of restenosis occurred following T-stenting.

We have decided to take another approach and define a bifurcation main plane by fitting a plane using two centerlines within the bifurcation core, which starts from the proximal delimiter where the two centerlines start to split and ends at two distal delimiters where the bifurcation core ends and separates into two daughter branches, and by minimizing the distance from the carina to the plane. Figure 3-6 shows the definition of bifurcation main plane. The optimal viewing angle is determined by the direction perpendicular to the bifurcation main plane. By this viewing angle, the visualization of the ostium of the sidebranch is improved when a heavily curved main vessel is present.

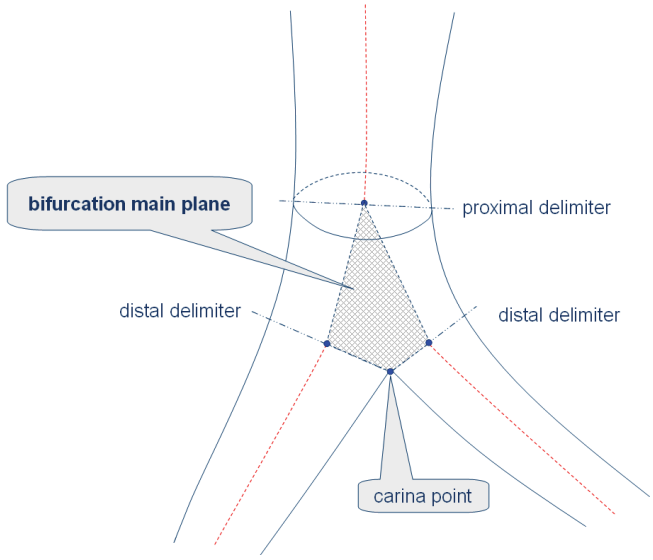

Figure 3-6. The definition of bifurcation main plane

Figure 3-7 shows a clinical example of a biplane acquisition. The frontal image was acquired under 35.8 RAO and 0.2 Caudal, while the lateral image was acquired under 53.4 LAO and 0.2 Caudal. The start and end positions of the bifurcation were indicated for the reconstruction. Figure 3-8 shows the visualization of the reconstructed bifurcation under the optimal viewing angle, being 52.0 LAO and 20.1 Caudal. Clearly, the bifurcation core and the sidebranch are well visualized, with minimum overlap under the optimal view. It is expected that this viewing angle will

enable the interventionalists to accurately see whether the stent has completely covered the ostium of the sidebranch and whether there is stent protrusion into the main vessel.

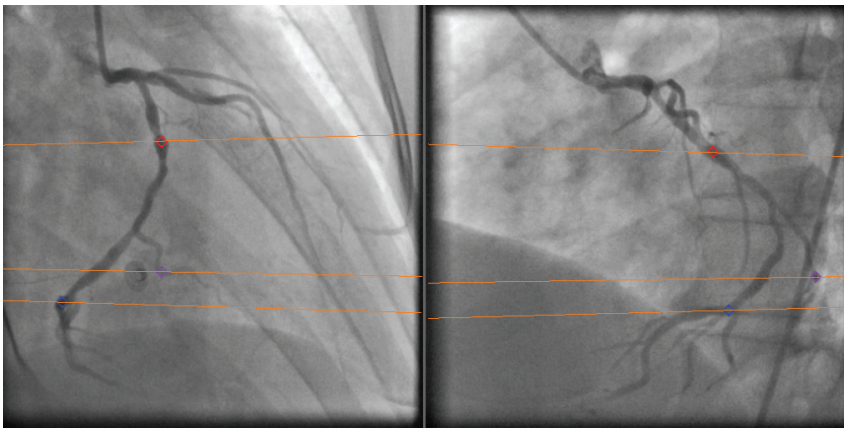

Figure 3-7. A biplane data: Frontal image (left); Lateral image (right). Courtesy, Dept of Cardiology, Leiden University Medical Center (LUMC), the Netherlands.

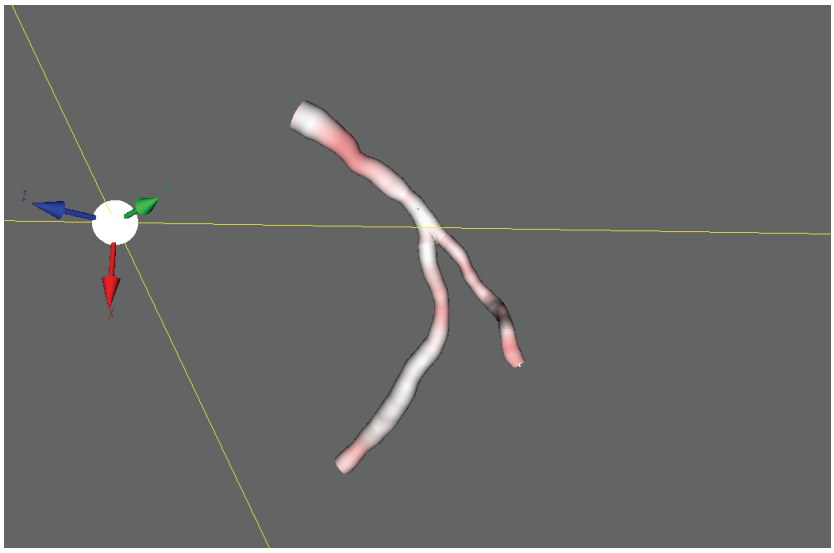

Figure 3-8. The reconstructed bifurcation under the optimal viewing angle, being 52.0 LAO and 20.1 Caudal.

3.4 VALIDATIONS

3.4.1 Data acquisition protocols

Three wire phantoms with a number of markers were used in the validation study. At the Leiden University Medical Center, angiographic images were acquired using a Toshiba biplane X-ray system with a flat-panel image intensifier. The distance from the focal spot to the image

intensifier was set at 1100 mm. The first phantom was acquired with image size of 512×512 and intensifier size of 15 cm, while the other two phantoms were acquired with image size of 1024×1024 and intensifier size of 20 cm. All phantoms were acquired at multiple projections and images were stored in DICOM files. Figure 3-9 shows two of the wire phantoms used in the validation study. The thin cutting positions on the wires were used as markers.

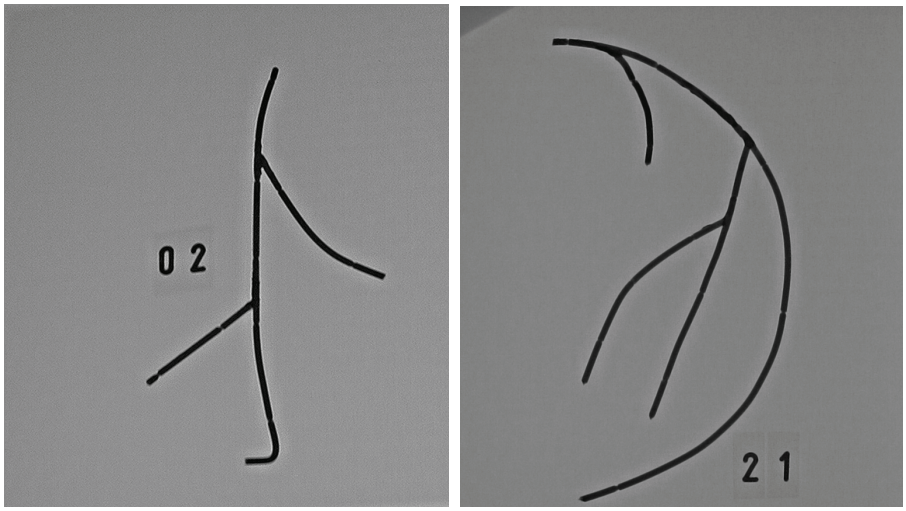

Figure 3-9. Wire phantoms used in the validation study.

3.4.2 Segment length assessment

Twelve segments with length ranging from 16.5 mm to 39.0 mm were defined by the markers on the wire phantoms. The average length for these 12 segments is 24.15 mm. Each segment was reconstructed 4 to 5 times using different combinations of projections (with a difference of 30º to 120º in acquisition angles between the frontal and lateral projections) and its length was measured from each reconstruction, resulting in 52 QCA measurements. The accuracy of these measurements was assessed by comparing these with the known true length of the wire segments.

3.4.3 Bifurcation optimal viewing angle

In order to determine the ground truth of optimal viewing angle for each bifurcation, two orthogonal iron sticks were attached to each bifurcation, one stick on the main distal vessel and the other one on the sidebranch, with the first half parts of two iron sticks joining together as the optimal viewing vector. Figure 3-10 shows two projections of one wire phantom with the attached orthogonal iron sticks. The optimal viewing vector for each bifurcation was carefully adjusted to the best direction to view its related bifurcation. After that, the phantom was put back to the

same position on the table of the X-ray system as the previous acquisitions. For each bifurcation, the table was changed to the position where the bifurcation core was visualized in the middle of the projection image. Next, the rotation and angulation angles were adjusted until the optimal viewing vector was visualized as one point. The reading of the acquisition angles was used as the ground truth for that particular bifurcation. An example of the phantom under the optimal viewing angle for the lowest bifurcation (arrow in left image) and the middle bifurcation (arrow in right image) is given by Figure 3-10.

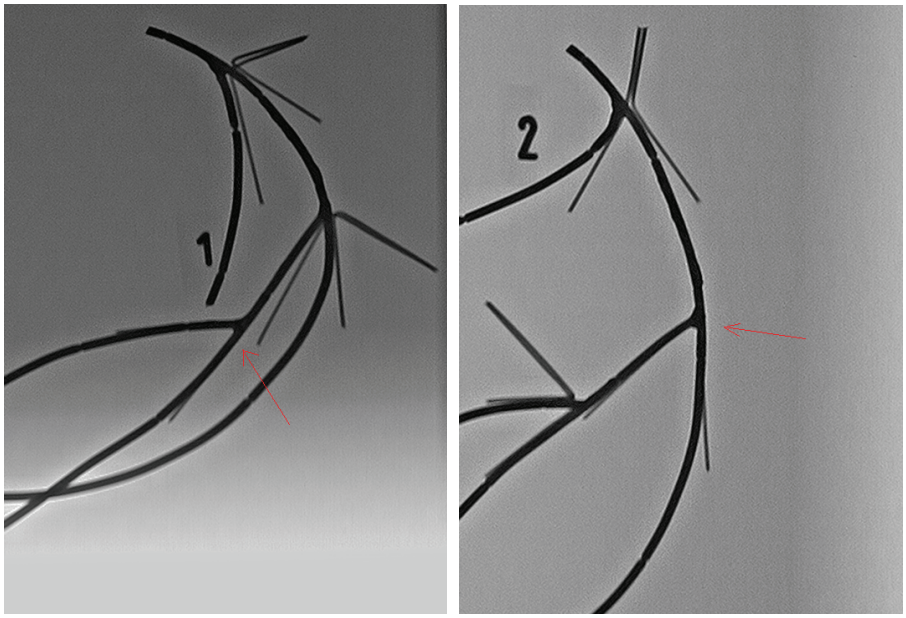

Figure 3-10. Determining the ground truth of optimal viewing angle by using the orthogonal iron sticks: Left image under 4 RAO and 40 Cranial; Right image under 44 LAO and 3 Cranial. The arrow indicates which bifurcation is optimally visualized.

A total of 6 bifurcations from three wire phantoms were used in the validation. Each bifurcation was reconstructed 8 times using different combinations of the projections (with a difference of 30º to 120º in acquisition angles between the frontal and lateral projections) and its optimal viewing angle was assessed from the reconstruction, resulting in 48 measurements.

3.5 Statistics

The correlation between 3D QCA segment length and the true wire segment length was calculated using Pearson's correlation coefficient. The Bland-Altman plot was used to evaluate the difference between the 3D QCA assessment and the true length, while student t-test was performed to investigate the statistical significance of the difference.

The difference of optimal viewing angles between the 3D QCA assessment and the ground truth was evaluated by a scatter plot in terms of rotation angle and angulation angle. The mean difference of the optimal viewing angle was computed and considered to be an index to the accuracy of the QCA assessment, while the standard deviation of the difference was considered as an index of precision. Student t-test was performed to investigate the statistical significance of the difference.
All statistical analyses were carried out by using statistical software (SPSS, version 16.0; SPSS Inc; Chicago, IL, USA).

3.6 Results

The correlation of 3D QCA segment length and the true wire segment length is presented in Figure 3-11. The segment length assessed by 3D QCA correlated very well with the true wire segment length (R^2 = 0.999). Bland-Altman plot for the correlation is given in Figure 3-12. No trend for the difference as a function of the true length was found. The mean and standard deviation of the difference between QCA assessment and the true length were 0.04 mm and 0.25 mm, respectively. The difference was significant (P < 0.01), in other words, 3D QCA slightly overestimated the segment length by 0.04 mm for a segment with an average length of 24.15 mm.

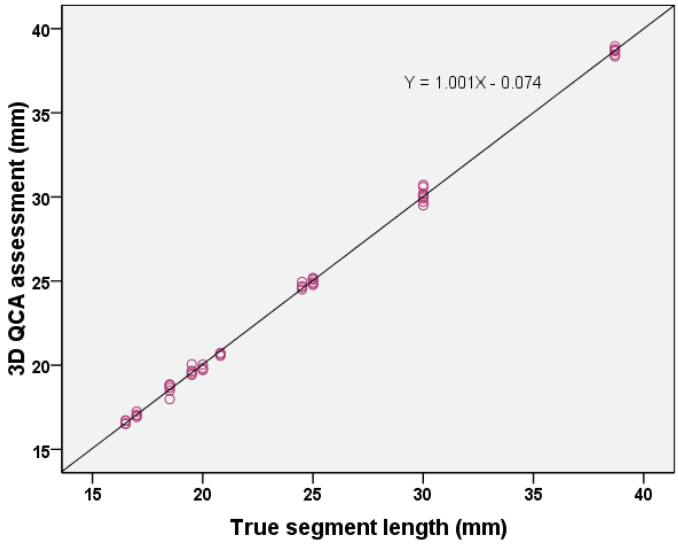

Figure 3-11. Correlation of 3D QCA with the true wire segment length.

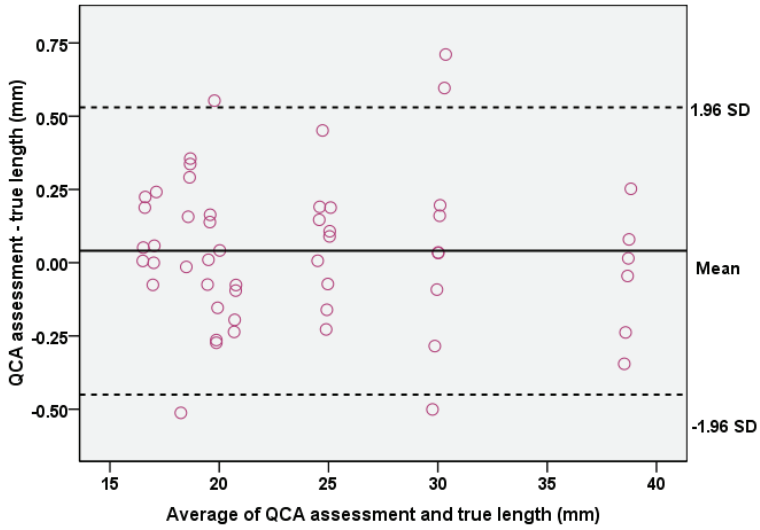

Figure 3-12. Bland-Altman plot of 3D QCA and the true wire segment length.

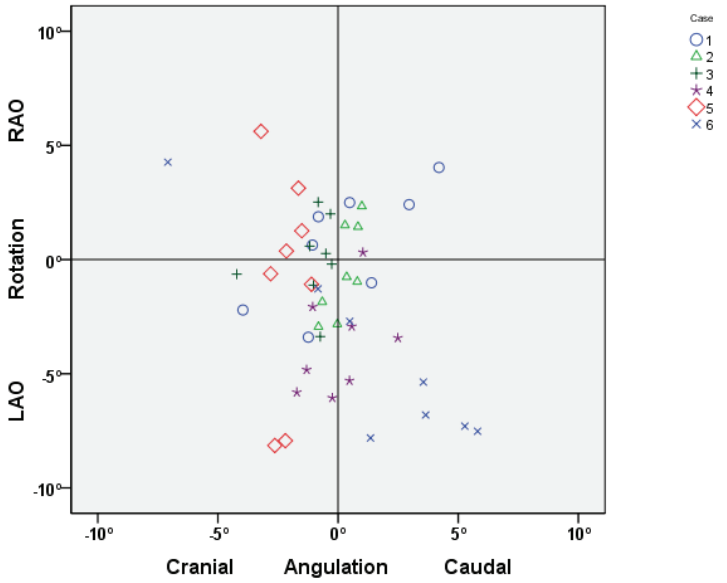

Figure 3-13. Scatter plot for the difference of optimal view angle between 3D QCA assessment and the ground truth.

An optimal viewing angle consists of two parts: rotation angle and angulation angle. The scatter plot for the difference of optimal viewing angles assessed by 3D QCA and the ground truth in terms of these two parts is given by Figure 3-13. The shape of the scatter points represents the bifurcation case. No specific pattern was observed within any bifurcation case, indicating that the assessment was not sensitive to the

acquisition angles for the reconstruction. The descriptive statistics is given by table 1. The mean and standard deviation of the difference of rotation angles between QCA assessment and the ground truth was -1.5º and 3.6º, respectively. The difference was significant (P < 0.01). The mean and standard deviation of the difference of angulation angles between 3D QCA assessment and the ground truth were -0.2º and 2.4º, respectively. The difference was not significant (P = 0.54). In other words, 3D QCA slightly underestimated the optimal rotation angle by 1.5º.

Table 1 The difference of optimal viewing angle between QCA assessment and the ground truth

	Number of assessment	Minimum	Maximum	Mean	Std. Deviation
Rotation (RAO)	48	-8.1º	5.6º	-1.5º	3.6º
Angulation (CAUD)	48	-7.1º	5.8º	-0.2º	2.4º

3.7 Discussions

Over the past years, the development of coronary visualization and quantitative analysis systems has been motivated by the increasing need to better understand the true dimensions of vascular structures and by the on-line need for coronary interventions in catheterization laboratories. 3D QCA has received a lot of interest for the potential benefits of increasing the assessment capabilities for both diagnostic and interventional cardiology. It was thought that the 3D QCA could resolve a number of additional limitations of standard 2D analysis, such as elimination of foreshortening and out-of-plane magnification error [11]. In addition, the automatic identification of the optimal viewing angle might benefit the patients and staffs from less radiation exposure by reducing the trials in achieving the best "working view".

Despite the fact that two simultaneously acquired images are available from biplane X-ray imaging systems, the development of a reliable and robust 3D QCA system is still not a trivial task. All current 3D QCA systems work best under conditions of the two X-ray systems rotating around the isocenter. However, the change of gantry geometry during the image acquisition might significantly shift the isocenter. In addition, the requirement of rotating two X-ray gantries around the same isocenter is a significant constraint to the operator in clinical routine. In other words, 3D QCA should also work accurately under non-isocentric conditions. In order to achieve this, the isocenter offset, i.e., the spatial displacement of the isocenters in the frontal and lateral systems, should be approximated and eliminated before the reconstruction. Ideally, a couple of reliable landmarks should be identified on both projections as reference points to determine the isocenter offset. On the other hand, the practical usage has

been hampered by the efforts in identifying many reliable landmarks, which turned out to be too time consuming or even impossible to identifying such reliable landmarks on the two projections. We have developed an approach by using only one to three pairs of reference points for the correction of the isocenter offset. The phantom validation by using only one or two markers as reference points to correct for the isocenter offset showed a high accuracy in the assessments of segment length and optimal viewing angle. In addition to the refinement of imaging geometry, we have also addressed the difficult problems in the centerline reconstruction when small perspective viewing angles and noise-corrupt arterial centerlines are present, which are expected to occur more frequently in routine clinical acquisitions. Although different acquisitions were used for the reconstruction (the acquisition angles for the frontal and lateral projections varies from 30º to 120º), the variations of the assessments for both segment length and optimal viewing angle were relatively small.

The delineation of vessel segment in 3D QCA could potentially increase the accuracy in stent selection. In current approaches, the selection of stent sizes mainly depends on the obstruction length assessed by visual estimation (eyeballing) or by 2D QCA. Conventionally, the calibration procedure, e.g., catheter calibration, should be performed at the first step of the assessment, which might as well introduce calibration variability. In addition, the foreshortening of the vessel of interest could cause significant underestimation of segment length [13, 21, 22], which could not be assessed or recognized directly from the 2D projections. The ad hoc solution of deploying additional stents when the first-select stent turns out to be of insufficient length could significantly increase the cost. Therefore, in some catheterization laboratories it becomes common for the interventionalists to consider the obstruction length a bit longer than the assessed result. As a result of that, the selection of stent might turn out to be longer than necessary, which could change unnecessarily the behavior of the arteries and associate a possible high risk of restenosis. On the other hand, the usage of automatic calibration in 3D QCA and the high accuracy of 3D QCA in segment length assessment could change the operator in decision making [12].

The ability to identifying the optimal viewing angle is another important feature of 3D QCA systems, especially for the on-line support of coronary interventions. Nevertheless, the optimal viewing angle has been interpreted differently: optimal viewing angle with minimal foreshortening and overlap [3], optimal viewing angle for the maximal exposure of lesion severity, or optimal viewing angle to optimally visualize the stent position in the bifurcation. These interpretations might generate different results

for certain bifurcations, e.g., the left main bifurcation with strongly curved left anterior descending artery. For the best interest of bifurcation related interventional procedures, we have decided to take the last interpretation and use the orthogonal view of the bifurcation main plane as the bifurcation optimal view, since we believe that this optimal view could benefit the interventionalists most in positioning the stent at the correct position and increase the angiographic success. An example case can be observed in T-Stenting: inappropriate view of the stent position might lead to incomplete lesion covering at the ostium of a sidebranch or stent protrusion into the main vessel [23]. Besides, this orthogonal view might as well expose the lesion severity at its maximum, due to the fact that atherosclerotic plaques occur preferably at the outer lateral wall of the bifurcation, i.e., the site opposite to the carina, where flow is more turbulent and endothelial shear stress is lower.

Despite high accuracy and robustness have been achieved by our 3D QCA system, the practical usage of the system has been hampered by the fact that biplane X-ray angiograms are hardly used in routine interventional cardiology. However, combing with the ECG-gated technique, our approach can be extended with a solution for monoplane X-ray systems. The introduction of isocenter offset correction could also be expected to eliminate the shift of heart caused by the patient respiration when changing the gantry from the first projection to the second projection. Future work is directed at performing extensive clinical validations for monoplane X-ray systems.

3.8 Conclusions

A novel 3D QCA system based on X-ray angiograms has been achieved by introducing a highly reproducible vessel centerline reconstruction. The validation study by using wire phantoms showed a high degree of accuracy and precision in the assessments of segment length and optimal viewing angle.

3.9 References

1. Reiber JHC, Tuinenburg JC, Koning G, et al. Quantitative coronary arteriography. In: Coronary Radiology 2nd Revised Edition, Oudkerk M, Reiser MF (Eds.), Series: Medical Radiology, Sub series: Diagnostic Imaging, Baert AL, Knauth M, Sartor K (Eds.). Springer-Verlag, Berlin-Heidelberg, 2009:41-65.
2. Wahle A. Oswald H, Fleck E. 3D Heart-Vessel Reconstruction from Biplane Angiograms. IEEE Computer Graphics and Application 1996; 16:65-73.
3. Chen SJ, Carroll JD, Messenger JC. Quantitative Analysis of Reconstructed 3-D Coronary Arterial Tree and Intracoronary Devices. IEEE Transaction on Medical Imaging 2002; 21:724-740.
4. Metz CE, Fencil LE. Determination of three-dimensional structure in biplane radiography without prior knowledge of the relationship between the two views: Theory. Med Phys 1989;16:45-51.

5. Dumay ACM. Image Reconstruction from Biplane Angiographic Projections. Dissertation 1992, Delft University of Technology.
6. Hoffmann KR, Anindya S, Li L, et al. A system for determination of 3D vessel tree centerlines from biplane images. The International Journal of Cardiac Imaging 2000; 16:315-330.
7. Wahle A, Wellnhofer E, Mugaragu I, et al. Assessment of Diffuse Coronary Artery Disease by Quantitative Analysis of Coronary Morphology Based upon 3-D Reconstruction from Biplane Angiograms. IEEE Transaction on Medical Imaging 1995; 14:230 – 241.
8. Van Der Zwet PMJ, Reiber JHC. A new approach for the quantification of complex lesion morphology: the gradient field transform; Basic principle and validation results. Journal of the American College of Cardiology 1994; 24: 216-224.
9. Janssen JP, Koning G, de Koning PJH, Tuinenburg JC, Reiber JHC. A novel approach for the detection of pathlines in X-Ray angiograms: the wave propagation algorithm. The International Journal of Cardiovascular Imaging 2002; 18:317-324.
10. Goktekin O, Kaplan S, Dimopoulos K, et al. A New Quantitative Analysis System for the Evaluation of Coronary Bifurcation Lesions: Comparison with Current Conventional Methods. Catheterization and Cardiovascular Interventions 2007; 69:172-180.
11. Koning G, Hekking E, Kemppainen JS, Richardson G., Rothman MT, Reiber JHC. Suitability of the Cordis StabilizerTM marker guide wire for quantitative coronary angiography calibration: An in vitro and in vivo study. Catheterization and Cardiovascular Interventions 2001; 52:334-341.
12. Gollapudi RR, Valencia R, Lee SS, Wong GB, Teirstein PS, Price MJ. Utility of Three-Dimensional Reconstruction of Coronary Angiography to Guide Percutaneous Coronary Intervention. Catheterization and Cardiovascular Interventions 2007; 69:479-482.
13. Agostoni P, Biondi-Zoccai G, Van Langenhove G, et al. Comparison of Assessment of Native Coronary Arteries by Standard Versus Three-Dimensional Coronary Angiography. The American journal of cardiology 2008; 102:272-279.
14. Green NE, Chen SJ, Hansgen AR, Messenger JC, Groves BM, Carroll JD. Angiographic Views Used for Percutaneous Coronary Interventions: A Three Dimensional Analysis of Physician-Determined vs. Computer-Generated Views. Catheterization and Cardiovascular Interventions 2005; 64:451–459.
15. Medina A, de Lezo JS, Pan M. A new classification of coronary bifurcation lesions. Rev Espanola de Cardiol 2006; 59:183-184.
16. Sadamatsu K, Sagara S, Yamawaki T, Tashiro H. Three-dimensional coronary imaging for the ostium of the left anterior descending artery. International Journal of Cardiovasc Imaging 2009; 25:223-228.
17. Lemos PA, Saia F, Ligthart JM, et al. Coronary restenosis after sirolimus-eluting stent implantation: morphological description and mechanistic analysis from a consecutive series of cases. Circulation 2003; 108:257-260.
18. Chen SJ, Carroll JD. 3-D Reconstruction of Coronary Arterial Tree to Optimize Angiographic Visualization. IEEE Transactions on Medical Imaging 2000, 19: 318-336.
19. Christiaens J, Van de Walle R, Gheeraert P, Taeymans Y, Lemahieu I. Determination of optimal angiographic viewing angles for QCA. International Congress Series 2001; 1230:909–915.
20. Dumay ACM, Reiber JHC, Gerbrands JJ. Determination of Optimal Angiographic Viewing Angles: Basic Pinciples and Evaluation Study. IEEE Transactions on Medical Imaging 1994; 13:13–24.

21. Bruining N, Tanimoto S, Otsuka M, et al. Quantitative multi-modality imaging analysis of a bioabsorbable poly-L-lactic acid stent design in the acute phase: a comparison between 2- and 3D-QCA, QCU and QMSCT-CA. Euro Intervention 2008; 4:285-291.
22. Rittger H, Schertel B, Schmidt M, Justiz J, Brachmann J, Sinha A. Three-dimenstional reconstruction allows accurate quantification and length measurements of coronary artery stenoses. EuroIntervention 2009; 5: 127-132.
23. Vigna C, Biondi-Zoccai G, Amico CM, et al. Provisional T-drug-eluting stenting technique for the treatment of bifurcation lesions: clinical, myocardial scintigraphy and (late) coronary angiographic results. The Journal of invasive cardiology 2007; 19:92-97.

CHAPTER 4

The Impact of Acquisition Angle Differences on Three-dimensional Quantitative Coronary Angiography

This chapter was adapted from:

The Impact of Acquisition Angle Differences on Three-dimensional Quantitative Coronary Angiography
Shengxian Tu, Niels R. Holm, Gerhard Koning,
Michael Maeng, Johan H.C. Reiber
Catheterization and Cardiovascular Interventions. 2011,
Volume 78, Issue 2, Pages 214-222.

ABSTRACT

Background: Three-dimensional (3D) quantitative coronary angiography (QCA) requires two angiographic views to restore vessel dimensions. This study investigated the impact of acquisition angle differences (AAD) of the two angiographic views on the assessed dimensions by 3D QCA.

Methods: X-ray angiographic images of an assembled brass phantom with different types of straight lesions were recorded at multiple angiographic projections. The projections were randomly matched as pairs and 3D QCA was performed in those pairs with AAD larger than 25º. The lesion length and diameter stenosis in three different lesions, a circular concentric severe lesion (A), a circular concentric moderate lesion (B), and a circular eccentric moderate lesion (C), were measured by 3D QCA. The acquisition protocol was repeated for a silicone bifurcation phantom and the bifurcation angles and bifurcation core volume were measured by 3D QCA. The measurements were compared with the true dimensions if applicable and their correlation with AAD was studied.

Results: 50 matched pairs of angiographic views were analyzed for the brass phantom. The average value of AAD was 48.0±14.1º. The per cent diameter stenosis was slightly overestimated by 3D QCA for all lesions: A (error 1.2±0.9%, $p < 0.001$); B (error 0.6±0.5%, $p < 0.001$); C (error 1.1±0.6%, $p < 0.001$). The correlation of the measurements with AAD was only significant for lesion A ($R^2 = 0.151$, $p = 0.005$). The lesion length was slightly overestimated by 3D QCA for lesion A (error 0.06±0.18 mm, $p = 0.026$), but well assessed for lesion B (error -0.00±0.16 mm, $p = 0.950$) and lesion C (error -0.01±0.18 mm, $p = 0.585$). The correlation of the measurements with AAD was not significant for any lesion. 40 matched pairs of angiographic views were analyzed for the bifurcation phantom. The average value of AAD was 49.1±15.4º. 3D QCA slightly overestimated the proximal angle (error 0.4±1.1º, $p = 0.046$) and the distal angle (error 1.5±1.3º, $p < 0.001$). The correlation with AAD was only significant for the distal angle ($R^2 = 0.256$, $p = 0.001$). The correlation of bifurcation core volume measurements with AAD was not significant ($p = 0.750$). Of the two aforementioned measurements with significant correlation with AAD, the errors tended to increase as AAD became larger.

Conclusions: 3D QCA can be used to reliably assess vessel dimensions and bifurcation angles. Increasing the acquisition angle difference of the two angiographic views does not increase accuracy and precision of 3D QCA for circular lesions or bifurcation dimensions.

4.1 Introduction

Over the past decades, the continuous developments in coronary visualization and quantitative systems have been motivated by the increasing need to better assess coronary atherosclerosis and by the on-line need for support of coronary interventions in cardiac catheterization laboratories. Recently developed three-dimensional quantitative coronary angiography (3D QCA) systems [1-5] aimed to combine two angiographic views from either biplane or monoplane angiograms to restore true vessel dimensions and hence, to resolve some of the well-known limitations of the conventional two-dimensional (2D) quantitative analysis [6-7], e.g., vessel foreshortening and out-of-plane magnification [8]. It has been shown that 3D QCA can better assess vessel segment length [2, 9] and bifurcation angles [10], as well as enabling the subsequent automated determination of optimal viewing angles for the subsequent stent deployment and positioning [11]. However, to the best knowledge of the authors, the impact of acquisition angle difference (AAD) of the two angiographic views on the 3D quantitative assessments has not been studied.

This study investigated the impact of AAD on the assessments of vessel dimensions including diameter stenosis, lesion length, bifurcation angles, and bifurcation core volume for phantoms with known dimensions.

4.2 Materials and Methods

4.2.1 Assembled brass phantom

At the Leiden University Medical Center (Leiden, The Netherlands), X-ray images of an assembled brass phantom with different types of lesions was acquired by an X-ray angiogram (Infinix, Toshiba Medical Systems, Tokyo, Japan) at multiple viewing angles. Images were recorded at a resolution of 1024×1024 pixels and stored in DICOM (Digital Imaging and Communications in Medicine) format. The distance from the X-ray source to the image intensifier was set as 1000 mm for all acquisitions. For the entire acquisition procedure, the angulation angle (Cranial/ Caudal) of the C-arm was changed to 25 Caudal, 15 Caudal, 0º, 15 Cranial, and 25 Cranial, while the rotation angle (LAO/RAO) was changed to 45 LAO, 30 LAO, 15 LAO, 0º, 10 RAO, 20 RAO, 30 RAO, and 40 RAO. The angiographic image was recorded at each combination of rotation and angulation angles.

A total of 40 angiographic views with different acquisition angles were recorded. A computer program was used to randomly select each time two angiographic views with at least 25º in AAD and match the two views as a pair for the subsequent analysis. The AAD of the matched pair was defined

by the angle between the two central projection beams that were determined by the combination of rotation and angulation angles for each angiographic view, respectively. All analyses were performed by an experienced analyst using a recently developed 3D QCA software package (prototype version, Medis medical imaging systems bv, Leiden, Netherlands) [2, 9, 11]. The software package excluded matched pairs that resulted in a perspective viewing angle (PVA) of less than 5º for the entire segment of interest. The PVA was defined as the angle between the epipolar line, being the projection of the X-ray beam directed towards a particular point on one of the projections onto the second projection, and the tangent of the vessel at the corresponding position [9]. Figure 4-1 shows an example of an excluded matched pair: The first angiographic view was acquired at 45 LAO, 25 Cranial and the second angiographic view at 45 LAO, 15 Caudal. In this case, the epipolar line was almost parallel to the vessel with an eccentric lesion at the corresponding marker position.

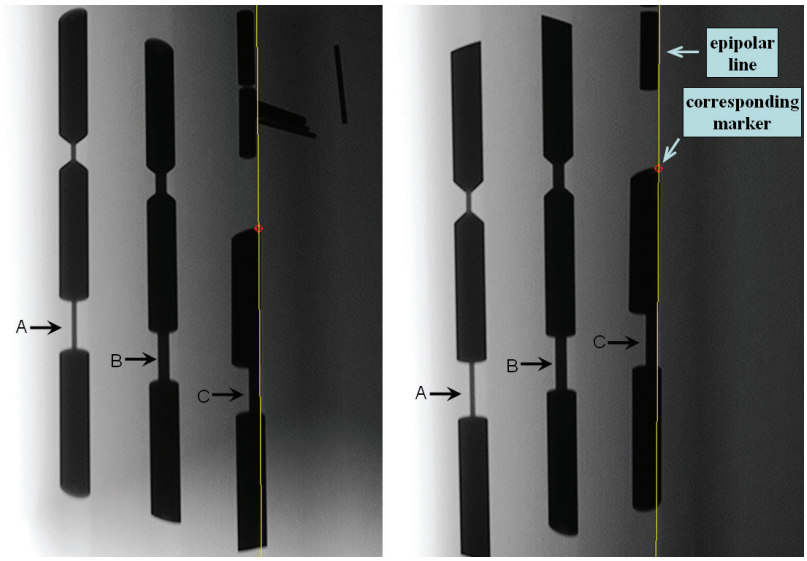

Figure 4-1. The excluded matched pair for 3D angiographic reconstruction. Left angiographic view at 45 LAO, 25 Cranial and right angiographic view at 45 LAO, 15 Caudal. The perspective viewing angle is almost zero for all three lesions. A is a circular concentric severe lesion; B is a circular concentric moderate lesion; and C is a circular eccentric moderate lesion.

For each included matched pair, the diameter stenosis and lesion length were assessed on 3 different types of straight lesions in the brass phantom, i.e., a circular concentric severe lesion (A), a circular concentric moderate lesion (B), and a circular eccentric moderate lesion (C). In addition, the reference diameter was also assessed on lesion B and

compared with the true dimension. Figure 4-1 shows the three types of lesions with known dimensions: A and B have circular concentric cross-sections with 80% and 60% diameter stenosis, respectively; C has circular eccentric cross-sections with 60% diameter stenosis; All three lesions have the same length (10.0 mm) and the same reference diameter (5.00 mm).

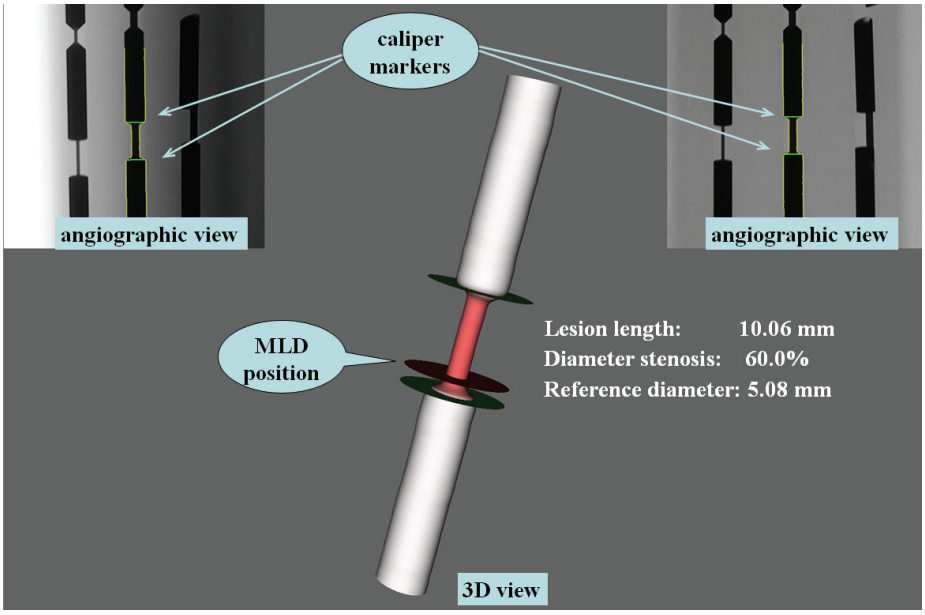

Figure 4-2. An analyzed matched pair of angiographic views and the 3D QCA assessed dimensions. Left angiographic view at 45 LAO, 15 Caudal and right angiographic view at 20 RAO, 15 Cranial. Diameter stenosis and reference diameter were reported at the MLD position.

Due to the angiographic isocenter offset introduced by gantry sag and other system distortions at different acquisition angles, one or two landmarks were used in the software package to correct the isocenter offset for each matched pair [9]. In the next step, lumen contours were detected automatically after specifying the proximal and distal positions for the segment of interest, followed by 3D reconstruction and quantifications. The position of the minimum lumen diameter (MLD) was automatically detected by the software package and diameter stenosis and the reference diameter were reported at that position. For lesion length assessment, the analyst moved the caliper markers to the lesion borders in one of the angiographic views, blinded to the measurement result. Since the repositioning of a marker in different views in the software package was supported by the fact that there existed a point correspondence between the 2D and 3D views, therefore, the caliper markers in the 3D view were synchronized to the lesion borders and the

3D lesion length was reported. Figure 4-2 shows an example of one analyzed matched pair and the 3D QCA assessed dimensions. In this case, the lesion has a length of 10.06 mm, diameter stenosis of 60.0%, and reference diameter of 5.08 mm.

The analyses on lesion B for the first 15 included matched pairs were repeated by the same analyst two months later, and by a second experienced analyst, both blinded to the earlier measurement results. From these measurements, intra- and inter-observer variabilities in the assessments of diameter stenosis, lesion length, and reference diameter were derived.

4.2.2 Silicone bifurcation phantom

At the Aarhus University Hospital, Skejby (Aarhus, Denmark), a silicone bifurcation phantom (Via Biomedical, CA, USA) with known dimensions was filled with iodinated contrast media (Visipaque 320, GE Healthcare, WI, USA) and scanned by an X-ray angiogram (AlluraXper, Philips Medical Systems, Best, The Netherlands). Images were recorded at a resolution of 1024×1024 pixels and stored in DICOM format. For the entire acquisition procedure, the angulation angle (Cranial/ Caudal) was changed to 20 Caudal, 0º, 20 Cranial, while the rotation angle (LAO/RAO) was changed to 45 LAO, 30 LAO, 15 LAO, 0º, 10 RAO, 20 RAO, 30 RAO, and 40 RAO. The angiographic image was recorded at each combination of rotation and angulation angles.

A total of 24 angiographic views with different acquisition angles were recorded. The same computer program was used to randomly select pairs of angiographic views with at least 25º in AAD. All analyses were performed by an experienced analyst using the same software package, blinded to the true bifurcation dimensions. For bifurcation analysis, the software package excluded those matched pairs that resulted in a PVA of less than 5º for either the entire main vessel or the entire sidebranch.

For each included matched pair, the bifurcation angles and bifurcation core volume were assessed. Two bifurcation angles, i.e., the proximal angle between the proximal main vessel (PMV) and the distal main vessel (DMV), and the distal angle between the DMV and the sidebranch (SB) [12], were measured. Figure 4-3 shows one angiographic view of an analyzed matched pair and the reconstructed bifurcation in 3D. In this case, the PVA was about 30º for the main vessel and 80º for the sidebranch. Hence, the matched pair was included for the subsequent analysis. The bifurcation core was separated by 3 delimiters: The proximal delimiter at the most distal position of PMV; The distal delimiter at the most proximal (carina) position of DMV; and the side delimiter at the most proximal (carina) position of SB. The cross-section of the bifurcation core

was of bean shape, as corresponded to the green contours that were superimposed onto the 3D bifurcation core in Figure 4-3. The size of the bifurcation core L was automatically determined by the combination of reference diameters of DMV and SB at the carina position. Therefore, the size of bifurcation core varied with the individual reconstructed bifurcation and more importantly, it was independent from the extent of lesion severity at the bifurcation core. Three directional vectors were estimated by applying linear regression algorithms on the sub-segments of PMV, DMV, and SB, respectively, with the same size of the bifurcation core. The proximal angle was defined by the angle between vector 1 and vector 3, while the distal angle was defined by vector 2 and vector 3. The bifurcation angles and bifurcation core volume were automatically calculated and reported by the software package. The true proximal and distal angles for the bifurcation phantom are 135º and 45º, respectively.

The analyses for the first 15 included matched pairs were repeated by the same analyst two months later, and by a second experienced analyst, both blinded to the earlier measurement results. From these measurements, intra- and inter-observer variabilities in the assessments of bifurcation angles and bifurcation core volume were derived.

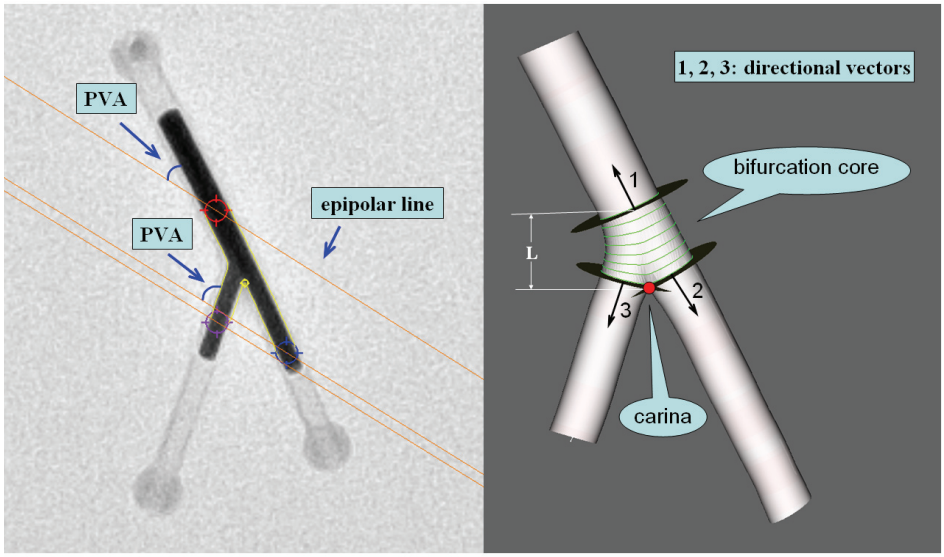

Figure 4-3. Angiographic view at 30 LAO, 20 Caudal of the silicone phantom and the reconstructed bifurcation in 3D. The 3D bifurcation core was separated by 3 delimiters (circular cross-sectional markers). The proximal angle was defined by the angle between vector 1 and vector 3, while the distal angle was defined by vector 2 and vector 3. The perspective viewing angle (PVA) was about 30º for the main vessel and 80º for the sidebranch.

4.3 Statistics

The results of 3D QCA measurements except for bifurcation core volume (unknown true dimension) were compared with the true dimensions by using paired *t*-test. The accuracy and precision were presented as measurement error and variability. Quantitative data were presented as mean difference ± standard deviation and the correlations were assessed by using Pearson's correlation coefficient, providing the correlation coefficient (R^2). If the correlation was significant, the equation of the regression line was provided. A 2-sided *p*-value of <0.05 was considered to be significant. All statistical analyses were carried out by using a statistical software package (SPSS, version 16.0; SPSS Inc; Chicago, IL, USA).

4.4 Results

A total of 52 matched pairs of angiographic views with AAD larger than 25º were generated for the brass phantom. Two matched pairs were excluded due to a small PVA for the entire vessel of interest. Therefore, 3D QCA was performed on the 50 remaining matched pairs. The values of AAD in the remaining matched pairs ranged from 27.1º to 85.5º, with an average value of 48.0±14.1º. The results of the 3D QCA assessments are given in Table I. In short, the per cent diameter stenosis was slightly overestimated by 3D QCA for all lesions: A (error 1.2±0.9%, $p < 0.001$); B (error 0.6±0.5%, $p < 0.001$); C (error 1.1±0.6%, $p < 0.001$). The intra- and inter-observer variabilities were 0.15±0.54 and 0.33±0.55, respectively. The lesion length was slightly overestimated by 3D QCA for lesion A (error 0.06±0.18 mm, $p = 0.026$), but well assessed for lesion B (error -0.00±0.16 mm, $p = 0.950$) and lesion C (error -0.01±0.18 mm, $p = 0.585$). The intra- and inter-observer variabilities were 0.08±0.11 and 0.04±0.14, respectively. The reference diameter (only measured in lesion B) was slightly overestimated by 3D QCA (error 0.07±0.03 mm, $p < 0.001$). The intra- and inter-observer variabilities were 0.01±0.01 and 0.01±0.01, respectively. Figure 4-4 and 4-5 show the scatter plots of the errors in measuring the diameter stenosis and lesion length, respectively. The correlation of the diameter stenosis measurements with AAD was significant for lesion A ($R^2 = 0.151$, $p = 0.005$, linear regression equation: Error = 0.025 × AAD – 0.019), but not for lesion B ($R^2 = 0.012$, $p = 0.440$) and lesion C ($R^2 = 0.025$, $p = 0.275$). The measurement error for lesion A tended to increase as AAD became larger. The correlation of the lesion length measurements with AAD was not significant for any lesion: A ($R^2 = 0.002$, $p = 0.747$); B ($R^2 = 0.002$, $p = 0.772$); C ($R^2 = 0.000$, $p = 0.959$).

TABLE I. 3D QCA ASSESSMENTS FOR THE BRASS AND SILLICONE PHANTOMS

	Mean ± SD	95% CI	Intra-observer error	Inter-observer error
Diameter stenosis (%)				
Lesion A	81.17 ± 0.91	(80.92-81.43)	-	-
Lesion B	60.56 ± 0.49	(60.42-60.70)	0.15 ± 0.54	0.33 ± 0.55
Lesion C	61.10 ± 0.56	(60.94-61.26)	-	-
Lesion length (mm)				
Lesion A	10.06 ± 0.18	(10.01-10.11)	-	-
Lesion B	10.00 ± 0.16	(9.9 5-10.04)	0.08 ± 0.11	0.04 ± 0.14
Lesion C	9.99 ± 0.18	(9.94-10.04)	-	-
Reference diameter (mm)	5.07 ± 0.03	(5.06 - 5.08)	0.01 ± 0.01	0.01 ± 0.01
Proximal bifurcation angle (°)	135.35 ± 1.08	(135.01-135.70)	0.33 ± 1.03	0.45 ± 0.89
Distal bifurcation angle (°)	46.54 ± 1.32	(46.12-46.96)	0.84 ± 1.02	0.26 ± 0.78
Bifurcation core volume (mm^3)	29.51 ± 1.11	(29.15-29.86)	0.13 ± 1.55	0.01 ± 0.90

CI, confidence interval

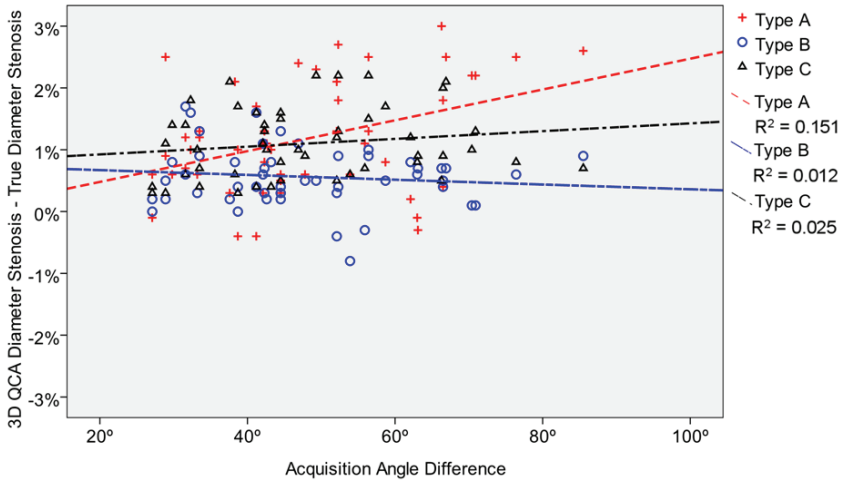

Figure 4-4. Diameter stenosis assessment by 3D QCA. The correlation of the3D QCA measurements with AAD was significant for lesion A, but not for lesion B and lesion C.

A total of 45 matched pairs of angiographic views with AAD larger than 25º were generated for the silicone bifurcation phantom. Five matched pairs were excluded due to the small PVA for either the entire main vessel or the entire sidebranch. Therefore, 3D QCA was performed on 40 remaining matched pairs. The values of AAD in the remaining matched pairs ranged from 25.8º to 85.0º, with an average value of 49.1±15.4º. The results of the measurements are given in Table I. In short, 3D QCA slightly overestimated the proximal angle (error 0.4±1.1º, p = 0.046) and the distal angle (error 1.5±1.3º, p < 0.001). The intra- and inter-observer variabilities for the proximal angle were 0.33±1.03 and 0.45±0.89, and for the distal angle were 0.84±1.02 and 0.26±0.78,

respectively. Figure 4-6 shows the scatter plot of the errors in measuring the bifurcation angles. The correlation with AAD was not significant for the proximal angle (R^2 = 0.012, p = 0.502), but significant for the distal angle (R^2 = 0.256, p = 0.001, linear regression equation: Error = 0.043 × AAD – 0.590). The measurement error for the distal angle tended to increase as AAD became larger. The bifurcation core had an average volume of 29.5±1.11 mm^3. The intra- and inter-observer variability was 0.13±1.55 and 0.01±0.90, respectively. The correlation with AAD was not significant (R^2 = 0.003, p = 0.750).

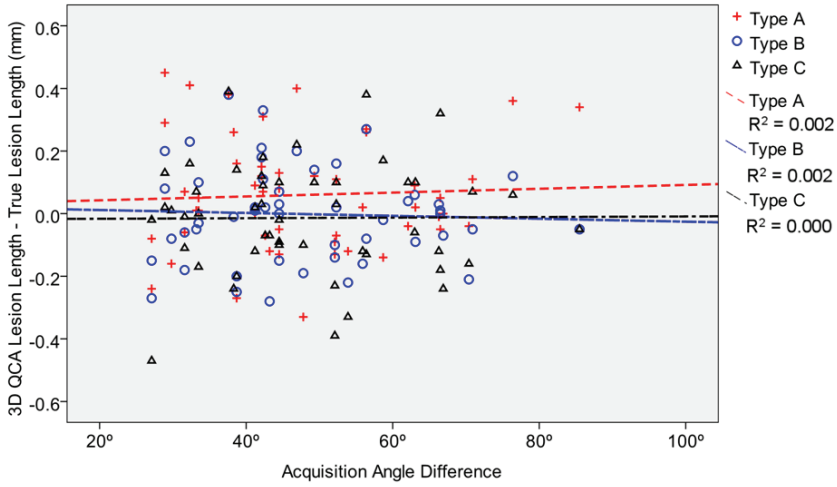

Figure 4-5. Lesion length assessment by 3D QCA. The correlation of the3D QCA measurements with AAD was not significant for any lesion.

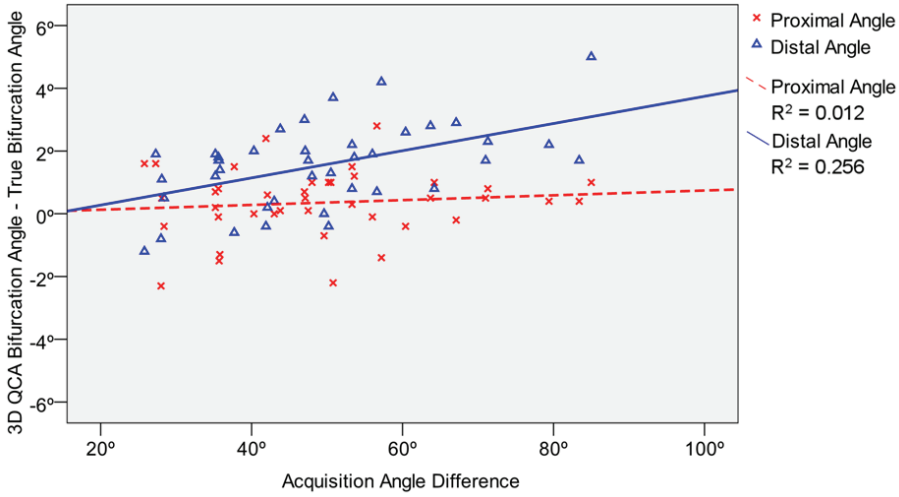

Figure 4-6. Bifurcation angle assessment by 3D QCA. The correlation of the3D QCA measurements with AAD was significant for the distal angle, but not for the proximal angle.

4.5 Discussions

Quantitative coronary angiography was first developed to quantify vessel motion and the effects of pharmacological agents on the regression and progression of coronary artery disease [13]. It has developed substantially over the past decades and has been applied worldwide for research and clinical purposes, in both off-line and on-line situations [7]. Although QCA techniques have been evolving with its wide applications [14-16], it remains as a limitation for 2D analysis that proper calibration, e.g., catheter calibration, needs to be performed for every analysis. If the vessel of interest is not in the calibration plane, the so-called out-of-plane magnification error will occur and hence, result in inaccurate measurements of absolute vessel dimensions. In addition, due to the 2D representation of the 3D vascular structures, the assessments of segment length and bifurcation angles depend to a great extent on vessel tortuosity and the angiographic viewing angle [11]. 3D QCA was motivated to overcome such limitations and to provide more support for coronary interventions in catheterization laboratories. By combing two angiographic views and the geometry of X-ray projections, 3D QCA was able to reconstruct vessel centerline and restore more details of the luminal cross-sections [1,9,18]. The continuous efforts in the DICOM standardization have made the automatic calibration procedure in 3D QCA feasible for most modern X-ray angiograms. Rapid improvements in computer hardware have also enabled real time 3D reconstruction on a conventional PC [2].

Despite the recent progresses, 3D QCA has been used in limited number of studies. One of the main reasons is the lack of standard operation procedures or protocols for performing 3D QCA. So far there is no official guideline for the angiographic acquisition dedicated for 3D QCA in a broad clinical setting. In general, the analyst selected two of the available angiographic views that were acquired during coronary angiography and used those two views for the subsequent 3D analysis. The optimal selection criteria remain unclear. Particularly, the impact of AAD of the two selected angiographic views on the 3D reconstruction and quantitative assessments has not been studied. This study showed that AAD did not have significant impact on 3D QCA for circular moderate lesions. For assessing bifurcation dimensions, the correlation between AAD and 3D QCA was only significant for the distal bifurcation angle. The correlation was weak and it indicated that the measurement error tended to increase as AAD became larger. One possible explanation is that as AAD increased, there were more overlaps between the DMV and the SB at their proximal parts. Therefore, the computer detected DMV centerline at

the proximal part could be slightly shifted toward the SB, resulting in an increase in the angle between the DMV and SB directional vectors, i.e., the distal angle.

Although this study showed that larger AAD did not increase accuracy and precision of 3D QCA in assessing circular lesions and bifurcation dimensions, non-circular lesions with asymmetric cross-sectional geometry are frequently encountered when assessing significant coronary stenoses in vivo [17]. Performing 3D QCA on two angiographic views with larger AAD may reveal more details of the luminal cross-sections and result in better luminal area assessment. However, larger AAD could potentially introduce more isocenter offset, as well as increasing the chance of vessel overlapping in the angiographic views and impair the assessments, especially for bifurcations where there tend to be more overlaps between the DMV and the SB as AAD increases. In other words, there are pros and cons of using larger AAD for assessing non-circular lesions in vivo and the optimal value may depend on individual vessel/bifurcation and the coronary anatomy. The actual impact of AAD on 3D QCA to assess lesions with asymmetric cross-sections still requires proper validations. It may be of interest to note that 3D QCA software packages generally calculate lesion length based on the approximated healthy vessel centerline, i.e., the so-call reference centerline, which calculates the length of the centerline in the vessel as if there is no obstruction [2]. Therefore, it is reasonable to expect that the impact of AAD on 3D QCA length assessment will be limited for vessels with non-circular lesions as well.

In this phantom study, the two angiographic views that were used for the 3D angiographic reconstruction were randomly selected by a computer program. As a result of this, 2 out of 52 matched pairs were excluded from the subsequent analyses for the brass phantom due to a small PVA (the angle between the epipolar line and the tangent of the vessel) for the entire vessel, while 5 out of 45 matched pairs were excluded for the silicone bifurcation phantom. When the PVA is 0º, there exist a huge number of feasible solutions which could satisfy the projection data. Figure 4-7 shows an example of different vessels that could generate the same lumen contours in the projection views, i.e., projection A and B. In this case, using projection A and B for the 3D angiographic reconstruction will result in a PVA of 0º for the entire vessel. In other words, the reconstruction of vessel centerline from projection A and B is not unique, since the PVA of the two projections is 0º for the entire vessel. In principle, the density information could be incorporated to decrease the feasible solutions; however, such solutions are hampered by the general quality of angiographic images in routine clinical practice, especially when

there are overlaps from other vessel segments. It implies that in practice using two angiographic views with larger PVA is preferred for 3D angiographic reconstruction and quantitative analysis. It is important to note that two angiographic views with larger AAD do not necessarily generate larger PVA, and vice versa. In theory, the PVA is determined by the tangent direction of the individual vessel and the geometry of the two angiographic views including acquisition angles and the distance from the X-ray source to the image intensifier. If one projection is already acquired, the practical approach to generate larger PVA for a specific vessel is to rotate the C-arm around the principal direction of the vessel to acquire the second projection. More specifically, the acquisition angle can be adjusted by changing the rotation angle (LAO/RAO) or the angulation angle (Cranial/Caudal) of the C-arm. If the first projection visualizes the lesion properly, and if the vessel of interest is positioned along the Cranial-Caudal direction, then changing the rotation angle to acquire the second projection will result in a large PVA. On the contrary, if the vessel of interest is positioned along the LAO-RAO direction, changing the angulation angle to acquire the second projection will result in a large PVA. For bifurcation cases, a trade-off between the main vessel and the sidebranch should be made so that both branches have relatively large PVA.

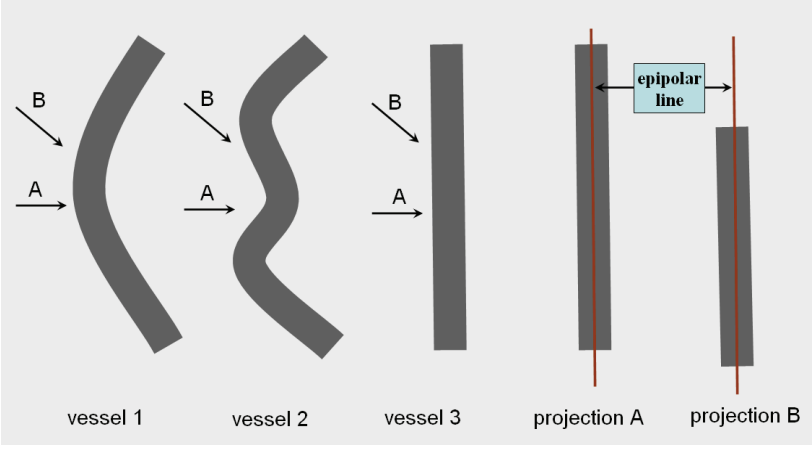

Figure 4-7. Different vessels that could generate the same lumen contours in the projections: Projection A and B have a perspective viewing angle (the angle between the epipolar line and the tangent of the vessel) of 0º for the entire vessel.

4.6 Limitations

Only lesions with circular concentric and circular eccentric cross-sections were investigated in this phantom study. The phantom studies do not account for the full complexity of angiographic acquisition artifacts in vivo, including angiographic system distortions, cardiac motions and

patient's respirations. In support of the findings, methods for the correction of such artifacts have been implemented in the software package.

4.7 Conclusions

3D QCA can be used to reliably assess vessel dimensions and bifurcation angles. Increasing the acquisition angle difference of the two angiographic views does not increase accuracy and precision of 3D QCA for circular lesions or bifurcation dimensions.

4.8 References

1. Wahle A, Lopez JJ, Olszewski ME, et al. Plaque development, vessel curvature, and wall shear stress in coronary arteries assessed by X-ray angiography and intravascular ultrasound. Medical Image Analysis 2006; 10: 615–631.
2. Tu S, Huang Z. Koning G, et al. A novel three-dimensional quantitative coronary angiography system: In-vivo comparison with intravascular ultrasound for assessing arterial segment length. Catheter Cardiovasc Interv 2010; 76: 291–298.
3. Gollapudi RR, Valencia R, Lee SS, et al. Utility of three-dimensional reconstruction of coronary angiography to guide percutaneous coronary intervention. Catheter Cardiovasc Interv 2007; 69:479–482.
4. Rittger H, Schertel B, Schmidt M, et al. Three-dimensional reconstruction allows accurate quantification and length measurements of coronary artery stenoses. EuroIntervention 2009; 5:127–132.
5. Green NE, Chen SY, Hansgen AR, et al. Angiographic views used for percutaneous coronary interventions: a three-dimensional analysis of physician-determined vs. computer-generated views. Catheter Cardiovasc Interv 2005; 64: 451–459.
6. Reiber JHC, Serruys PW, Kooijman CJ, et al. Assessment of short-, medium-, and long-term variations in arterial dimensions from computer-assisted quantitation of coronary cineangiograms. Circulation 1985; 71: 280–288.
7. Reiber JHC, Tuinenburg JC, Koning G, et al. Quantitative coronary arteriography. In: Coronary Radiology 2nd Revised Edition, Oudkerk M, Reiser MF (Eds.), Series: Medical Radiology, Sub series: Diagnostic Imaging, Baert AL, Knauth M, Sartor K (Eds.). Springer-Verlag, Berlin-Heidelberg, 2009:41-65.
8. Koning G, Hekking E, Kemppainen JS, et al. Suitability of the Cordis StabilizerTM marker guide wire for quantitative coronary angiography calibration: An in vitro and in vivo study. Catheter Cardiovasc Interv 2001; 52: 334–341.
9. Tu S, Koning G, Jukema W, et al. Assessment of obstruction length and optimal viewing angle from biplane X-ray angiograms. Int J Cardiovasc Imaging 2010; 26: 5–17.
10. Girasis C, Serruys PW, Onuma Y, et al. 3-Dimensional Bifurcation Angle Analysis in Patients With Left Main Disease. J Am Coll Cardiol Intv 2010; 3: 41–48.
11. Tu S, Hao P, Koning G, et al. In-vivo assessment of optimal viewing angles from X-ray coronary angiography. EuroIntervention 2011; 7:112-120.
12. Louvard Y, Thomas M, Dzavik V, et al. Classification of coronary artery bifurcation lesions and treatments: time for a consensus! Catheter Cardiovasc Interv 2008; 71:175–83.

13. Brown BG, Bolson E, Frimer M, et al. Quantitative coronary angiography : estimation of dimensions, hemodynamic resistance, and atheroma mass of coronary artery lesions using arteriography in 256 nonoperated patients. Circulation 1977; 55: 329–337.
14. Janssen JP, Rares A, Tuinenburg JC, et al. New approaches for the assessment of vessel sizes in quantitative (cardio-) vascular X-ray analysis, Int J Cardiovasc Imaging 2010; 26: 259–271.
15. Lansky A, Tuinenburg J, Costa M, et al. Quantitative Angiographic Methods for Bifurcation Lesions: A Consensus Statement from the European Bifurcation Group. Catheter Cardiovasc Interv 2009; 73: 258–266.
16. Holm NR, Højdahl H, Lassen JF, et al, Quantitative coronary analysis in the Nordic Bifurcation studies, Int J Cardiovasc Imaging 2010; 27:175-180.
17. Arbab-Zadeh A, Texter J, Ostbye KM, et al. Quantification of lumen stenoses with known dimensions by conventional angiography and computed tomography: implications of using conventional angiography as gold standard. Heart 2010; 96: 1358-1363.
18. Tu S, Holm NR, Kong G, Huang Z, et al. Fusion of 3D QCA and IVUS/OCT. Int J Cardiovasc imaging 2011; 27:197–207.

CHAPTER 5

A Novel Three-dimensional Quantitative Coronary Angiography System: In-vivo Comparison with Intravascular Ultrasound for Assessing Arterial Segment Length

This chapter was adapted from:

A Novel Three-dimensional Quantitative Coronary Angiography System:
In-vivo Comparison with Intravascular Ultrasound for
Assessing Arterial Segment Length
Shengxian Tu, Zheng Huang, Gerhard Koning, Kai Cui, Johan H. C. Reiber
Catheterization and Cardiovascular Interventions. 2010,
Volume 76, Issue 2, Pages 291-298.

ABSTRACT

Background: Accurate on-line assessments of vessel dimensions are of utmost importance for the selection of the right stent size in coronary interventions. Recently a new three-dimensional quantitative coronary angiography (3D QCA) analytical software package was developed. This study aimed to validate the 3D QCA software package for the assessment of arterial segment length by comparing with intravascular ultrasound (IVUS). In addition, the difference between 3D QCA and IVUS in assessing curved segments was studied.

Methods: A retrospective study including 20 patients undergoing both coronary angiography and IVUS examinations of the left coronary artery was set up for the validation. The same vessel segments of interest between the proximal and distal markers were identified and measured on both angiographic and IVUS images, by the 3D QCA software and by a quantitative IVUS software package, respectively. In addition, the curvature of each segment of interest was assessed and the correlation between the accumulated curvature of the segment and the difference in segment lengths measured from the two imaging modalities was analyzed.

Results: 37 vessel segments of interest were identified from both angiographic and IVUS images. The 3D QCA segment length was slightly longer than the IVUS segment length (15.42 ± 6.02 mm vs. 15.12 ± 5.81 mm, $p = 0.040$). The linear correlation of the two measurements was: 3D QCA Length = -0.09 + 1.03 * IVUS Length ($r^2 = 0.98$, $p < 0.001$). Bland-Altman plot showed that the difference in the two measurements was not correlated with the average of the two measurements ($p = 0.141$), but with the accumulated curvature of the segment ($p = 0.015$). After refining the difference by the correlation equation, the average difference of the two measurements decreased from 0.30 ± 0.86 mm ($p = 0.040$) to 0.00 ± 0.78 mm ($p = 0.977$).

Conclusions: The 3D QCA software package can accurately assess the true arterial segment length. The difference in segment lengths measured from 3D QCA and IVUS was correlated with the accumulated curvature of the segment.

5.1 Introduction

Over the past years, the continuous development in coronary visualization and quantitative analysis tools has been motivated by the increasing need to better assess the true dimensions of vascular structures and by the on-line need for support of coronary interventions in catheterization laboratories. Three-dimensional quantitative coronary angiography (3D QCA) based on routine angiographic projections has emerged as a new tool to increase the assessment capabilities for both diagnostic and interventional cardiology [1-8]. It was thought that the 3D QCA could resolve a number of additional limitations of standard two-dimensional (2D) analysis, such as elimination of foreshortening and out-of-plane magnification error [9], and help the interventionalists determine the optimal course of treatments and implement the chosen course of action. The advantages of 3D QCA with respect to standard 2D analysis have been presented in [5-7].

Recently we have developed a novel 3D QCA software package that was validated with phantom experiments [8]. By correcting for the angiographic system distortions and noise-corrupt errors in the 3D reconstruction, the software package has achieved high accuracy in the phantom validation. In this current paper we would like to address the in-vivo validation of our 3D QCA analytical approach for the assessment of vessel segment length by comparing with quantitative intravascular ultrasound (IVUS) measurements.

Although the motorized IVUS transducer pullback has been regarded as a standardized procedure for the measurement of segment length [10], the bending of the catheter inside the vessel could cause significant shift of the transducer pullback path away from the vessel centerline, especially for curved/tortuous vessels. This study also investigated the possible correlation between the accumulated curvature of the segment with the difference in the segment lengths assessed by 3D QCA and by IVUS.

5.2 Materials and methods

5.2.1 Materials

At the Department of Cardiology, Nanfang Hospital affiliated to the Southern Medical University in Guangzhou, China, 23 patients were randomly selected for the retrospective study from the patients who underwent both angiographic and IVUS examinations of the left coronary artery. Patients were considered for including IVUS imaging when the physicians felt the need to see the vessel wall composition to decide whether the lesions needed to be treated and if so, the treatment strategy and the optimal stents size, especially when the lesions were presented at

critical locations, e.g., the ostium of main arteries. Three patients were excluded from the study since the IVUS transducer pullback was performed manually during image acquisitions. Therefore, in total we studied 20 patients (LAD *n*=17, LCX *n*=3) by identifying and analyzing the same segments of interest on both angiographic and IVUS images.

Angiographic images were recorded at 25 frames/sec by a monoplane X-ray angiographic system (AXIOM-Artis, Siemens, Germany). IVUS scans were performed by using a motorized transducer pullback system (0.5 mm/s) with a rotating 40 MHz transducer catheter and 2.6 F imaging sheath (Boston Scientific, Boston, MA, USA).

5.2.2 Three-dimensional angiographic reconstruction and quantitative analysis

From the routine coronary angiography acquisitions, two image sequences acquired at two arbitrary angiographic views at least 25 degrees apart in viewing angles were selected for the reconstruction. The 3D angiographic reconstruction was performed using a recently developed 3D QCA software package (prototype version, Medis medical imaging systems bv, Leiden, The Netherlands) [8] and the whole procedure consists of four major steps: 1) Select the end-diastolic image frames with the lumen well filled with contrast from the two image sequences as projection views for the subsequent 3D reconstruction; 2) Identify one to three reference points, e.g., the same anatomical point or the same marker of the catheter, on both projection views for the automated correction of the system distortions introduced by the isocenter offset and the respiration-induced heart motion [4,8]; 3) Manually define the start and end positions of the vessel segment to be reconstructed on the projection views, and extract its contours and centerline [11-13]; 4) Reconstruct the centerline and cross-sections of the vessel segment in 3D after eliminating the noise-corrupt errors [8].

After the 3D reconstruction is achieved, length measurement can easily be performed by defining the proximal and distal markers for the segment of interest, i.e., particular subsegment of the reconstructed vessel segment (Figure 5-1). The start and end positions of these subsegments are best defined at the bifurcation points of sidebranches (the carina) for the subsequent comparison with the IVUS measurements. The vessel diameter which is closest to a bifurcation (the carina) is used as either the proximal or distal marker for defining the subsegment of interest. Such marker is visualized in the two projection views as well as in the 3D view. The repositioning of a marker in the different views is supported by the fact that there exists a point correspondence between the 2D and 3D views. Therefore, the analyst can very easily move the

marker in any of the three views to position it where needed. Because of the fixed point correspondence, there is no need to find a corresponding position in the 2D or 3D views; spatially, the data is synchronized which is a great advantage and minimizes any observer variability. In case of poor image quality around the carina, image enhancement techniques [14] could be used to increase the visibility of detailed image structures. In the example of Figure 5-1, the two thumbnails at the top left and top right panels show the two projection views selected for the reconstruction, with the extracted 2D lumen contours superimposed, plus the proximal and distal markers for the definition of the subsegment of interest. In the middle of the figure, the 3D view with the reconstructed vessel segment is presented, plus the 3D proximal and distal markers. After the positions of the proximal and distal markers are confirmed, the 3D segment length is automatically calculated. In addition, the software package also calculates the 2D segment length based on each of the two projections views by using the isocenter calibration approach. The result from the projection view which has the least foreshortening to the segment of interest is defined as the 2D QCA segment length and will be used to demonstrate the effect of the foreshortening in the 2D analysis, relative to the 3D QCA approach.

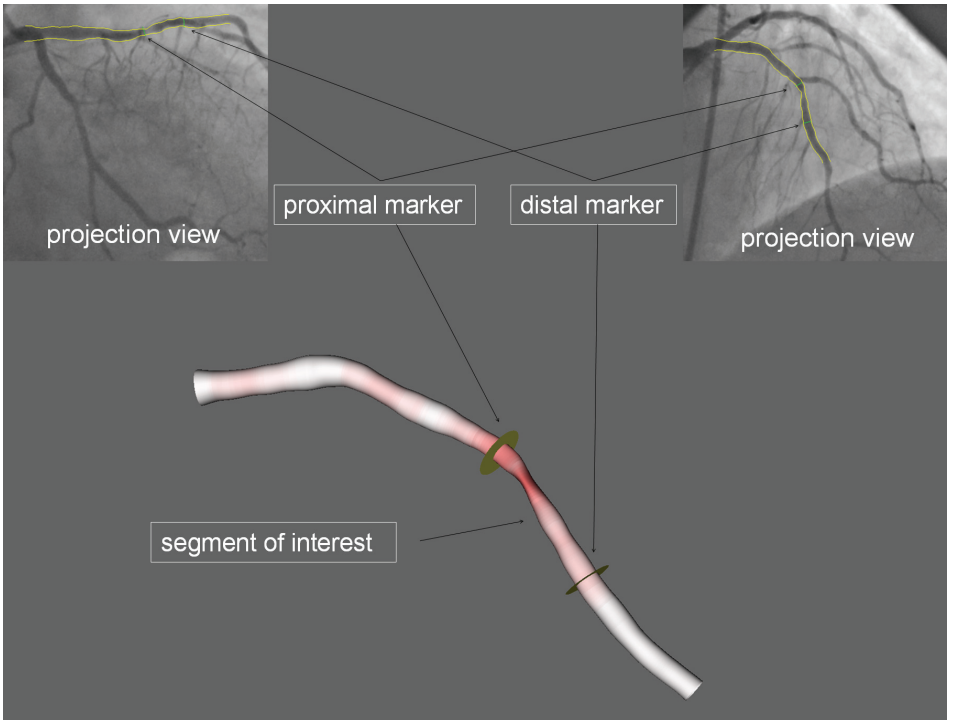

Figure 5-1. Three-dimensional angiographic reconstruction and the definition of segment of interest for length measurement.

The same protocols for the 3D angiographic reconstruction and length measurement were repeated by the same analyst one month later, blinded to his initial measurement results. From these first and second measurements, the intra-observer variability in the assessment of the segment length can be determined.

To calculate the accumulated curvature of the segment of interest, the 3D reconstructed centerline was first fitted to a smooth B-spline curve and the curvature was estimated from this B-spline curve for each curve point [15]. The accumulated curvature was obtained by summing up the curvature values for all the points on the segment of interest. An example of the fitted B-spline curve for the 3D reconstructed centerline in Figure 5-1 is given by Figure 5-2. The accumulated curvature for the segment of interest is 0.848 mm^{-1}.

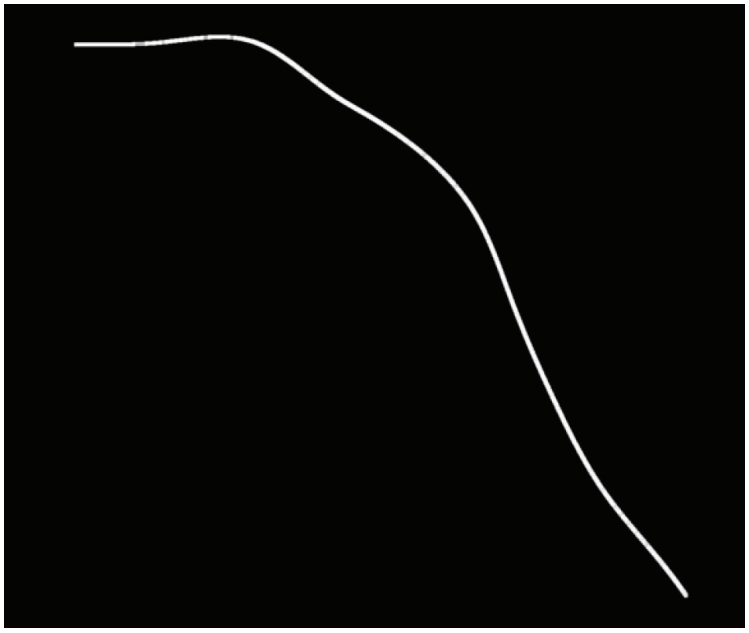

Figure 5-2. The fitted B-spline curve of the reconstructed centerline

5.2.3 Quantitative IVUS analysis

Intravascular ultrasound images were analyzed using a quantitative IVUS analysis software package (QIvus Clinical Edition 1.1, Medis medical imaging systems bv, Leiden, The Netherlands) [16]. By reconstructing a number of longitudinal image cuts which are parallel to the longitudinal axis through the transversal image stack and by viewing these in a movie mode, the software creates an impression of the 3D structure of the pullback sequence, which can be very helpful in identifying the positions of the bifurcation points to define the proximal and distal markers for the segment of interest, respectively.

An example of length measurements from the IVUS images for the same segment of interest as Figure 5-1 is given by Figure 5-3. By the combination of longitudinal images and transversal images, the proximal and distal markers to define the segment of interest were manually identified and the segment length was automatically calculated by the software; in the example the segment length is equal to 11.34 mm.

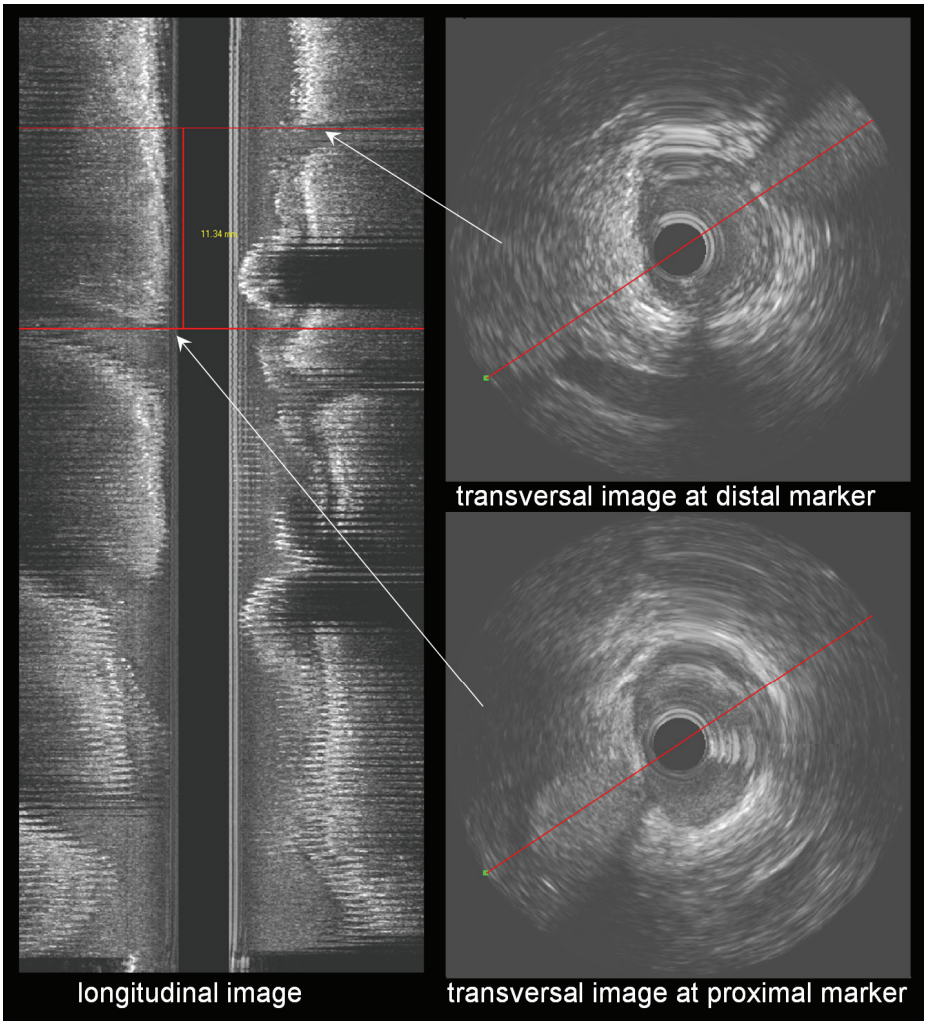

Figure 5-3. Length measurement by intravascular ultrasound. The sidebranches are visible in the longitudinal image and in the transversal images.

5.3 Statistics

The results of segment lengths measured from the two imaging modalities were compared by using a paired *t*-test. The correlation between the two measurements was assessed by using linear regression and the difference was evaluated by the Bland-Altman plot. The difference

in the two measurements was further analyzed by assessing its correlation with the accumulated curvature of the segment of interest.

In the aforementioned analyses, quantitative data were presented as mean ± standard deviation and the correlations were assessed by using Pearson's correlation coefficient, providing the correlation coefficient (r^2) and the equation of the regression line. A 2-sided p-value of <0.05 was considered to be significant. All statistical analyses were carried out by using a statistical software package (SPSS, version 16.0; SPSS Inc; Chicago, IL, USA).

5.4 Results

TABLE I. Baseline Characteristics

Age (years)	58.9 ± 13.2
Gender (male, female)	16/4
1–vessel disease	12 (60%)
2–vessel disease	7 (35%)
3–vessel disease	1 (5%)
Target coronary artery (*n*)	
Left anterior descending	19
Left circumflex	7
Right coronary artery	3
Location (*n*)	
Proximal	6
Mid	15
Distal	8
Percent diameter obstruction (%)	44.27 ± 15.38

The baseline characteristics for the 20 patients included in this retrospective study are summarized in Table I. A total of 37 vessel segments of interest were identified from both the angiographic and IVUS images for the quantitative analyses and comparisons. The results of segment lengths measured from 3D QCA ranged from 4.81 mm to 27.59 mm, with an average length of 15.42 ± 6.02 mm, while the results for the same segments of interest measured from IVUS ranged from 4.78 mm to 26.77 mm, with an average length of 15.12 ± 5.81 mm. Figure 5-4 shows a good correlation between the segment lengths measured from 3D QCA and from IVUS. The linear correlation for the two measurements is: 3D QCA Length = -0.09 + 1.03 * IVUS Length (r^2 = 0.98, p < 0.001). The intra-observer variability for measuring segment length from 3D QCA is 0.02 ± 0.41 mm (p = 0.772).

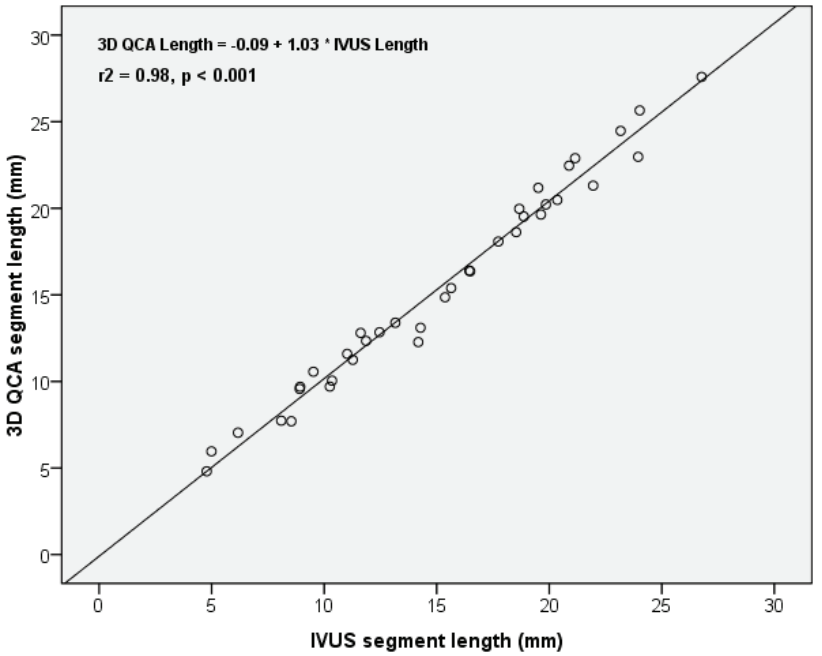

Figure 5-4. Correlation between 3D QCA and IVUS measurements.

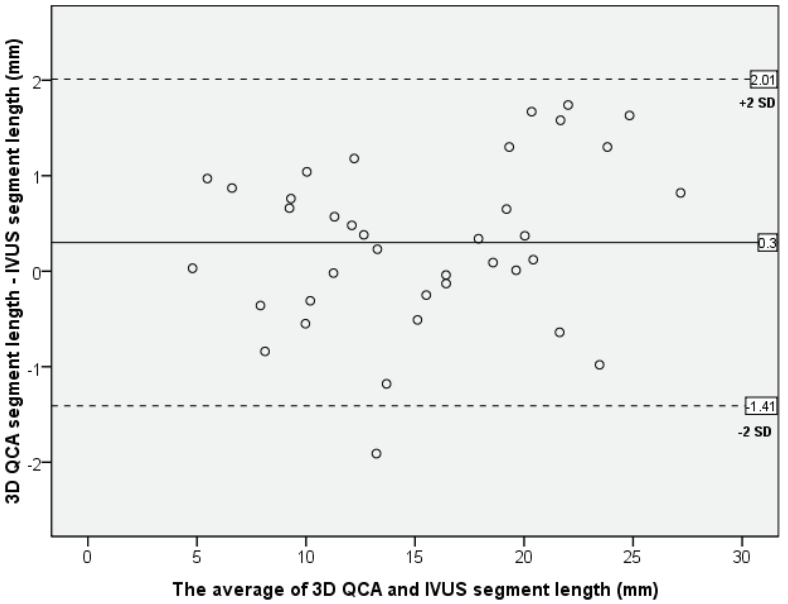

Figure 5-5. Bland-Altman plot of 3D QCA and IVUS measurements.

Bland-Altman plot in Figure 5-5 also shows a good correlation between the measurements from the two imaging modalities. 3D QCA segment length was slightly longer than IVUS segment length (Difference:

Chapter 5

0.30 ± 0.86 mm, p = 0.040). No specific pattern occurred in the difference between the two measurements, with respect to the average of the two measurements. Statistical test also showed that the difference was not correlated with the average value of the segment lengths measured from the two imaging modalities (p = 0.141). However, the difference in the two measurements was correlated with the accumulated curvature of the segment (p = 0.015). A scatter plot of the difference with respect to the accumulated curvature of the segment of interest is given by Figure 5-6. The linear regression equation is: Difference = -0.21 + 0.20 * Accu_curvature (r^2 = 0.16, p < 0.015). In other words, there was a systematic increase in the difference in the segment lengths measured from the two imaging modalities, as the accumulated curvature of the segment increased. After subtracting the systematic increase from the original difference, the average difference of the two measurements decreased to 0.00 ± 0.78 mm (p = 0.977).

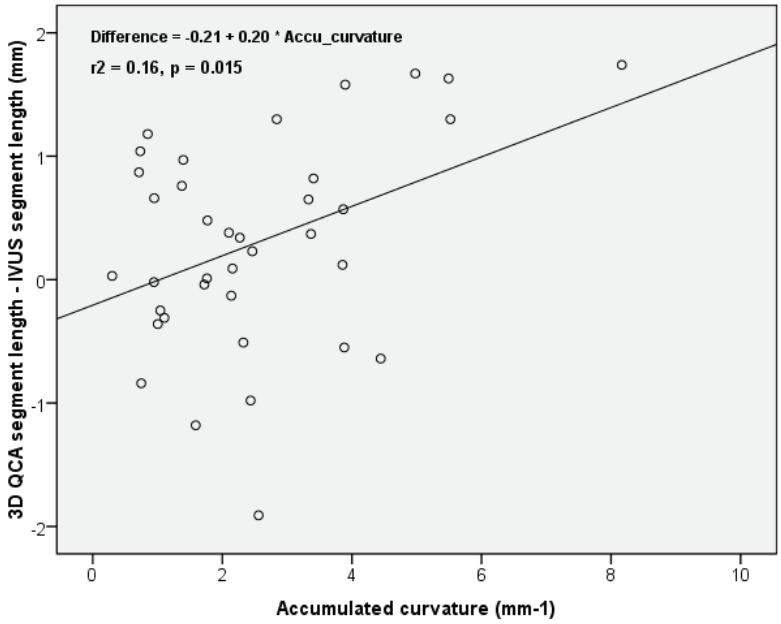

Figure 5-6. Correlation between the accumulated curvature of the segment and the difference in segment lengths measured from the two imaging modalities.

The average 2D QCA segment length for the 37 vessel segments of interest was 14.41 ± 5.88 mm versus 15.42 ± 6.02 mm for the 3D segment length. A scatter plot of the difference in the segment lengths measured from 3D and 2D QCA is given by Figure 5-7. The difference ranged from -0.35 mm to 4.01 mm, with an average value of 1.01 ± 1.05 mm, while the amount of foreshortening in the 2D analysis ranged from -

3% to 25%, with an average foreshortening of 7% ± 6%. Negative value meant that the 2D segment length was overestimated, which was caused by the out-of-plane magnification error in the 2D analysis [9].

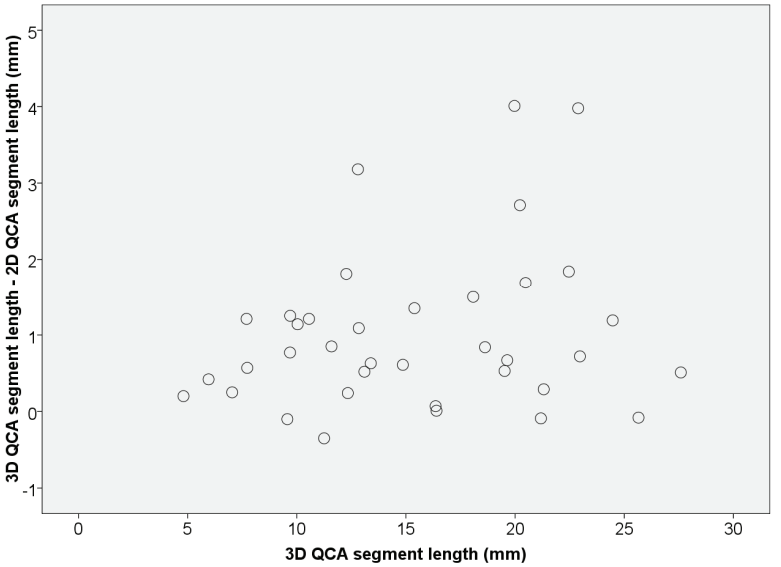

Figure 5-7. The difference in 3D QCA and 2D QCA measurements

5.5 Discussions

Coronary angioplasty is an invasive procedure to open obstructed arteries under the guidance of X-ray angiography. Despite the tremendous success of the procedure in the instant treatment of coronary artery disease, a higher risk of restenosis due to the suboptimal stent selection and deployment has hampered the translation of the procedure success into long-term outcomes [17-19]. The drug-eluting stents (DES) have proven to be able to reduce the in-stent restenosis after the intervention [20-22]; however, the efficacy depends on complete lesion coverage, and therefore requires appropriate stent selection [17,23]. The ad hoc solution of deploying additional stents when the first-select stent turns out to be of insufficient length could reduce the minimum stent area (MSA) and increase the dose of drug release on the overlapping area, which have been demonstrated to be associated with an increased risk of restenosis and thrombosis [24]. In addition, the total expense for the treatment will increase significantly. A stent of excessive length will unnecessarily change the behavior of the over-stented vessel segments, which could result in undesirable results, e.g., covering a sidebranch [25], or may have a negative influence on the motion of the vessel segments due to the imposed stiffness of the stent in the vessel and may even lead to fracture of the stent. Accurate assessment of arterial segment length is thus of

great importance for the selection of appropriate stent length required during coronary interventions. In general, one can say that the amount of metal in the segment should be minimized given a particular segment that must be scaffolded for the sake of cost-effectiveness and additional risks.

Quantitative coronary angiography (QCA) [11,26,27] was introduced in early '80 as a more objective and reproducible approach to overcome the subjectivity of visual estimation (eyeballing) and to reduce the variability in assessing the vessel dimensions from angiographic images. The conventional approach is to perform QCA on the selected 2D end-diastolic image frame by using a calibration approach, e.g., the catheter or isocenter calibration. Since the calibration factor only holds true for one particular plane perpendicular to the central projection axis, and this procedure assumes that the obstructed vessel segment lies in that particular plane; significant error due to the out-of-plane magnification [9] could exist when the assumption is not satisfied during the image acquisitions. Besides, due to the 2D representation of the 3D vascular structures, 2D QCA has inherent limitations in assessing curved segment length due to vessel foreshortening. The amount of foreshortening in 2D QCA depends on the vessel tortuosity and the experience of the operators in choosing the so-called optimal viewing angles [1,2] during image acquisitions. Significant vessel foreshortening in the length assessment by performing 2D QCA on the operator-selected view from standard clinical acquisitions has been reported [5,6,28] and the decision making could be changed by using the 3D QCA in the stent selection [5]. Our validation results also shows that 2D QCA by using isocenter calibration approach has an average of 7% foreshortening with respect to the 3D QCA measurements.

Intravascular ultrasound has been regarded as an adjunct tool for the selection of stent size and for the guidance of coronary interventions. In additional to the luminal imaging, IVUS also provides a wealth of other data including vessel wall composition. However, the additional expenses and the fact that these are often not covered by insurance companies, make that IVUS is not a standard option in many countries. The 3D angiographic reconstruction of course cannot provide information about the vessel wall composition, but only on lumen measurements, both diameters and length. However, the great advantage of the 3D QCA is that it requires no additional acquisition from routine angiographic projections and the execution time for the whole 3D reconstruction and analysis in our solution is just a few seconds on a standard PC. In addition, our software package is very robust, requires minimal user-interaction and provides also information about optimal viewing angles [8]. This in-vivo validation study showed that the segment length

measured from 3D QCA correlated well with the measurements from IVUS. Bland-Altman analysis also showed a good correlation between the two measurements, with a slightly longer segment length in the 3D QCA measurements. The difference could be partly explained by the fact that 3D QCA segment length was measured from the vessel centerline while IVUS segment length was measured from the transducer pullback path. Due to the bending of IVUS catheter inside the vessel, the transducer pullback path could be shifted significantly away from the vessel centerline to reach a state of minimum bending energy, especially for the curved vessel segments. It has been reported that there was a significant delay from the moment the IVUS pullback machine was switched on and the moment the transducer tip really started to move [29]. This phenomenon could be explained by the stretching of the catheter to the minimum energy state before the transducer really started its pullback and hence, the transducer pullback path was expected to be shorter than the vessel centerline. The amount of difference between the vessel centerline and the transducer pullback path depended on the tortuosity of the vessel segment. Our finding confirmed that the difference in segment lengths measured from 3D QCA and IVUS was correlated with the accumulated curvature of the segment. After refining the difference by the correlation, the average difference of the two measurements decreased further to 0.00 ± 0.78 mm (p = 0.977).

Although it was not the primary goal of this study, the finding of the correlation between the accumulated curvature and the difference in 3D QCA and IVUS segment lengths also demonstrated the feasibility of registering IVUS and angiographic image data by mapping the distance from the IVUS pullback path to the 3D vessel centerline [30] and hence, to skip the reconstruction of the catheter pullback path from the angiographic images, which was not a trivial task in many clinical acquisitions. To the best of the authors' knowledge, it was the first finding in such a correlation, which also indicated that the length assessment from IVUS could be much shorter than the true segment length for curved vessel segments and hence, needed to be adjusted for the selection of interventional devices if based on IVUS data alone.

In addition to the vessel curvature, vessel diameter and in particular plaque eccentricity could also change the catheter pullback path, which might impact on the assessment of segment length from IVUS. On the contrary, our 3D QCA software package corrects for these artifacts by measuring the length of the approximated healthy arterial centerline, i.e., the so-call reference centerline, which is a standard module in our QCA software packages and which calculates the length of the centerline in the vessel as if there was no obstruction.

Work from the Thoraxcenter has also demonstrated a good correlation between the segment length from another 3D QCA software package [3] and the IVUS measurements. However, a slight underestimation of the segment length was reported by that software package, compared with the IVUS measurements. The difference in their results and our results could be partly explained by the facts that different data and different analytical software packages were used in these two studies. New in our study is the correlation between the accumulated curvature of the vessel segment and the difference in segment lengths measured from the two imaging modalities.

5.6 Limitations

A relatively small number of patients were included in this retrospective study. Since the comparisons were performed on a segment by segment basis, the final analyses included a total of 37 segments of interest, which we believe is sufficient to demonstrate the accuracy in assessing arterial segment length, given the small variations in the assessments.

The results of 2D QCA segment length were limited to the two projection views selected for the 3D reconstruction. There was no guarantee that the optimal view for the 2D analysis was one of the projection views. In addition, we have used the isocenter calibration versus the usual catheter calibration approach.

The IVUS transducer pullback was not ECG gated, which could influence the results of length measurements from the IVUS images. In addition, only one IVUS transducer pullback system was investigated in this study. Early literatures have shown that the accuracy of length measurements using different pullback systems could be different [31].

5.7 Conclusions

The 3D QCA software package could accurately assess arterial segment length. The difference in segment lengths measured from 3D QCA and IVUS was correlated with the accumulated curvature of the segment.

5.8 References

1. Dumay AM, Reiber JHC, Gerbrands JJ. Determination of optimal angiographic viewing angles: basic principles and evaluation study. IEEE Trans Med Imaging 1994;13:13–24.
2. Green NE, Chen SY, Hansgen AR, et al. Angiographic views used for percutaneous coronary interventions: a three-dimensional analysis of physician-determined vs. computer-generated views. Catheter Cardiovasc Interv 2005; 64:451–459.

3. Schuurbiers JC, Lopez NG, Ligthart J, et al. In vivo validation of CAAS QCA-3D coronary reconstruction using fusion of angiography and intravascular ultrasound (ANGUS). Catheter Cardiovasc Interv 2009; 73:620–626.
4. Wahle A, Wellnhofer E, Mugaragu I, et al. Assessment of diffuse coronary artery disease by quantitative analysis of coronary morphology based upon 3-D reconstruction from biplane angiograms. IEEE Trans Med Imaging 1995; 14:230–241.
5. Gollapudi RR, Valencia R, Lee SS, et al. Utility of three-dimensional reconstruction of coronary angiography to guide percutaneous coronary intervention. Catheter Cardiovasc Interv 2007; 69:479–482.
6. Rittger H, Schertel B, Schmidt M, et al. Three-dimensional reconstruction allows accurate quantification and length measurements of coronary artery stenoses. EuroIntervention 2009; 5:127–132.
7. Bruining N, Tanimoto S, Otsuka M, et al. Quantitative multi-modality imaging analysis of a bioabsorbable poly-L-lactid acid stent design in the acute phase: a comparison between 2 and 3D-QCA, QCU and QMSCT-CA. EuroIntervention 2008; 4:285–291.
8. Tu S, Koning G, Jukema W, et al. Assessment of obstruction length and optimal viewing angle from biplane X-ray angiograms. Int J Cardiovasc Imaging 2010; 26:5–17.
9. Koning G, Hekking E, Kemppainen JS, et al. Suitability of the Cordis StabilizerTM marker guide wire for quantitative coronary angiography calibration: An in vitro and in vivo study. Catheter Cardiovasc Interv 2001; 52:334–341.
10. Mintz GS, Nissen SE, et al. American College of Cardiology clinical expert consensus document on standards for acquisition, measurement and reporting of intravascular ultrasound studies (IVUS). J Am Coll Cardiol 2001; 37:1478–1492.
11. Reiber JHC, Serruys PW, Kooijman CJ, et al. Assessment of short-, medium-, and long-term variations in arterial dimensions from computer-assisted quantitation of coronary cineangiograms. Circulation 1985; 71:280–288.
12. Janssen JP, Koning G, De Koning PJH, et al. A new approach to contour detection in X-ray arteriograms: The wavecontour. Investigative radiology 2005; 40:514–520.
13. Reiber JHC, Zwet PM van der, Koning G, et al. Accuracy and precision of quantitative digital coronary arteriography : observer-, short-, and medium-term variabilities. Cathet Cardiovasc Diagn 1993; 28:187–198.
14. Tu S, Koning G, Tuinenburg JC, et al. Coronary angiography enhancement for visualization. Int J Cardiovasc Imaging 2009; 25:657–667.
15. Sapidis N, Farin G. Automatic fairing algorithm for B-spline curves. Computer-aided design 1990; 22:121–129.
16. Dijkstra J, Koing G, Reiber JHC. Quantitative measurements in IVUS images. Int J Cardiac Imaging 1999; 15:513–522.
17. Costa MA, Angiolillo DJ, Tannenbaum M, et al. Impact of stent deployment procedural factors on long-term effectiveness and safety of sirolimus-eluting stents (final results of the multicenter prospective STLLR trial). Am J Cardiol 2008; 101:1704–1711.
18. Lemos PA, Saia F, Ligthart JM, et al. Coronary restenosis after sirolimus-eluting stent implantation: morphological description and mechanistic analysis from a consecutive series of cases. Circulation 2003; 108:257–260.
19. Aminian A, Kabir T, Eeckhout E. Treatment of drug-eluting stent restenosis: An emerging challenge. Catheter Cardiovasc Interv 2009; 74:108–116.
20. Moses JW, Leon MB, Popma JJ, et al. Sirolimus-eluting stents versus standard stents in patients with stenosis in a native coronary artery. N Engl J Med 2003; 349:1315–1323.
21. Stone GW, Ellis SG, Cox DA, et al. A polymer-based, paclitaxel-eluting stent in patients with coronary artery disease. N Engl J Med 2004; 350:221–231.

22. Stone GW, Moses JW, Ellis SG, et al. Safety and efficacy of sirolimus- and paclitaxel-eluting coronary stents. N Engl J Med 2007; 356:998–1008.
23. Fujii K, Carlier SG, Mintz GS, et al. Stent underexpansion and residual reference segment stenosis are related to stent thrombosis after sirolimus-eluting stent implantation: An intravascular ultrasound study. J Am Coll Cardiol 2005; 45:995–998.
24. Finn AV, Kolodgie FD, Harnek J, et al. Differential response of delayed healing and persistent inflammation at sites of overlap sirolimus- or paclitaxel-eluting stents. Circulation 2005; 112:270–278.
25. Colombo A, Stankovic G, Moses JW. Selection of coronary stents. J Am Coll Cardiol 2002; 40:1021–1033.
26. Reiber JHC, Tuinenburg JC, Koning G, et al. Quantitative coronary arteriography. In: Coronary Radiology 2nd Revised Edition, Oudkerk M, Reiser MF (Eds.), Series: Medical Radiology, Sub series: Diagnostic Imaging, Baert AL, Knauth M, Sartor K (Eds.). Springer-Verlag, Berlin-Heidelberg, 2009:41-65.
27. Goktekin O, Kaplan S, Dimopoulos K, et al. A New Quantitative Analysis System for the Evaluation of Coronary Bifurcation Lesions: Comparison with Current Conventional Methods. Catheter Cardiovasc Interv 2007; 69:172–180.
28. Bruining N, Tanimoto S, Otsuka M, et al. Quantitative multi-modality imaging analysis of a bioabsorbable poly-L-lactic acid stent design in the acute phase: a comparison between 2- and 3D-QCA, QCU and QMSCT-CA. EuroIntervention 2008; 4:285–291.
29. Rotger D, Radeva P, Canero C, et al. Corresponding IVUS and Angiogram Image Data. Proceedings of Computers in Cardiology 2001; 28:273–276.
30. Tu S, Koning G, Zheng H, et al. Coronary intervention planning by fusing angiogram and IVUS. Presented at Dutch Society for Pattern Recognition and Image Processing, Leiden, 2009.
31. Tanaka K, Carlier SG, Mintz GS, et al. The accuracy of length measurements using different intravascular ultrasound motorized transducer pullback systems. Int J Cardiovasc Imaging 2007; 23:733–738.

CHAPTER 6

In-vivo Assessment of Optimal Viewing Angles from X-ray Coronary Angiography

This chapter was adapted from:

In-vivo Assessment of Optimal Viewing Angles from
X-ray Coronary Angiography
Shengxian Tu, Peiyuan Hao, Gerhard Koning, Xianglong Wei,
Xudong Song, Aihua Chen, Johan H. C. Reiber
EuroIntervention. 2011,
Volume 7, Issue 1, Pages 112-120.

ABSTRACT

Aims: To propose and validate a novel approach to determine the optimal angiographic viewing angles for a selected coronary (target) segment from X-ray coronary angiography, without the need to reconstruct the whole coronary tree in three-dimension (3D), such that subsequent interventions are carried out from the best view.

Methods: The method starts with standard QCA of the target segment in two angiographic views (either biplane or 2 monoplane views). Next, the target vessel is reconstructed in 3D, and candidate viewing angles characterized by minimal foreshortening of the target vessel are calculated and proposed to the user. In a very simple and intuitive manner, the possible overlap of the target vessel and other coronary segments can be assessed. As a result, those candidate views which would result in significant overlap with other coronary segments are rejected and the best candidate view can be selected. A retrospective study including 67 patients, who underwent both coronary angiography and stenting procedures, was set up for the validation. The accuracy of overlap prediction was validated by comparing the predicted overlap results with the true overlap conditions on the available angiographic views (TEST views) acquired during coronary angiography. In addition, the percentages of foreshortening for the views proposed by the new approach (Software Viewing Angle, SVA) and the views used during the stent deployment (Expert Viewing Angle, EVA) were calculated, respectively. Two experienced interventional cardiologists evaluated the success of SVA with respect to EVA. The evaluation results were graded into five values ranging from -2 to 2 with a step of 1 and the average graded value from the two interventional cardiologists was defined as the score point for the evaluated case.

Results: The overlap prediction algorithm successfully predicted the overlap condition for all 235 TEST views. The accuracy of overlap prediction was 100%. The average difference in SVA and EVA was 22.3º±12.3º. EVA was associated with a much more foreshortening of the target vessel than SVA (8.9%±8.2% vs. 1.6%±1.5%, $p < 0.001$). The average score point for evaluating the success of SVA with respect to EVA was 0.94±0.80 ($p < 0.001$), indicating that the interventional cardiologists were in favor of the optimal views determined by the proposed approach compared with the views used during the actual intervention.

Conclusion: The proposed approach is able to accurately and quickly determine the optimal viewing angles for the on-line support of coronary interventions.

6.1 Introduction

Coronary angioplasty is an interventional procedure directed at opening obstructed arteries under the guidance of X-ray angiography. Despite the tremendous success of the procedure in the instant treatment of coronary artery disease, the occurrence of stent underexpansion or incomplete lesion coverage due to suboptimal stent selection and deployment techniques could significantly increase the risks of restenosis and thrombosis [1-4], hampering the translation of the procedural success into long-term positive outcomes.

Choosing appropriate angiographic views during coronary interventions is one of the important steps in the stent deployment and positioning, especially for complex bifurcation stenting. Optimal viewing angles are characterized by having minimal foreshortening of the target segment, ànd having minimal overlap with other coronary segments. Currently, three-dimensional quantitative coronary angiography (3D QCA) has been regarded as an adjunct tool for the determination of optimal viewing angles [5-9]. However, to the best knowledge of the authors, all the existing approaches would require that the whole coronary tree be reconstructed in order to calculate both foreshortening ànd possible overlap of the target vessel with other coronary vessels, and that requires a significant effort and time which is not available during the actual interventional procedure. Contrary to the existing methods, we have been looking for an approach that is able to predict the possible overlap between the target vessel and other coronary vessel segments without the need to carry out a 3D reconstruction of the entire coronary tree.

In this manuscript we propose and validate such a new approach for the rapid assessment of the optimal viewing angles of a target vessel including the assessment of the possible overlap with other coronary segments without the need to reconstruct the entire coronary tree in 3D. Given the efficiency of the procedure, we believe that it will be suitable very much for on-line support in the catheterization laboratory. The basic principles of the approach and the results of the validation will be described in the following paragraphs.

6.2 Materials and Methods

6.2.1 Population

At the Zhujiang Hospital affiliated to the Southern Medical University (About 800 coronary interventions are performed annually) in Guangzhou, China, 68 patients who underwent both coronary angiography and interventional stenting procedures between May and October, 2009 were selected for this retrospective study. Inclusion criteria were: 1) patients

had no prior history of coronary artery bypass surgery; 2) interventions were performed by interventional cardiologists with at least 10 years of experience in interventional cardiology; 3) angiographic images were recorded by X-ray angiograms with digital image intensifier (flat-panel).

The first stented vessel segment was chosen as the target vessel to be reconstructed and analyzed. Among 68 selected patients, 1 patient was excluded from the study due to the lack of a second angiographic view for the 3D reconstruction. Therefore, in total we studied 67 target vessels (LAD n=32, LCX n=15, RCA n=20). Angiographic images were recorded at 25 frames/s by a monoplane digital X-ray system (AXIOM-Artis, Siemens, Germany). All parameters required for the 3D reconstruction were stored in DICOM files.

6.2.2 Three-dimensional angiographic reconstruction

From the routine coronary angiography acquisitions, two image sequences acquired at two arbitrary angiographic views with at least 25 degrees apart in viewing angles were selected for the reconstruction. The 3D angiographic reconstruction consists of four major steps: 1) select the end-diastolic image frames with the vessel lumen well filled with contrast from the two image sequences as projection views for the subsequent 3D reconstruction; 2) identify one to three reference points, e.g., markers on the catheter and sidebranches, on both projection views for automated correcting of system distortions introduced by the isocenter offset and the respiration-induced heart motion [6,10]; 3) manually define the vessel segment of interest and extract its lumen contours and derived centerlines using our extensively validated QCA algorithms [11-13] in the two angiographic views; and 4) reconstruct the 3D centerline and cross-sections after refining the correspondence between the two extracted centerlines [6]. In case of poor angiographic image quality, image enhancement techniques [14] could be used to increase the visibility of detailed image structures for the identification of reference points in step 2.

An example of system distortions in the image geometry for the 3D reconstruction is given in Figure 6-1. The catheter tip and the bifurcation in the left circumflex artery (LCX) were identified as reference points and their epipolar lines, each being the projection of the X-ray beam directed towards a particular point on one of the projection view onto the second projection view [15], were presented in the two projection views (1 RAO, 34 Caudal and 28 RAO, 26 Caudal, respectively). Due to the system distortions, the epipolar lines did not go through their corresponding reference points. After applying the automated correction for the system distortion, the epipolar lines went right through their corresponding

reference points in both projection views (Figure 6-2), demonstrating the success and quality of this automated procedure.

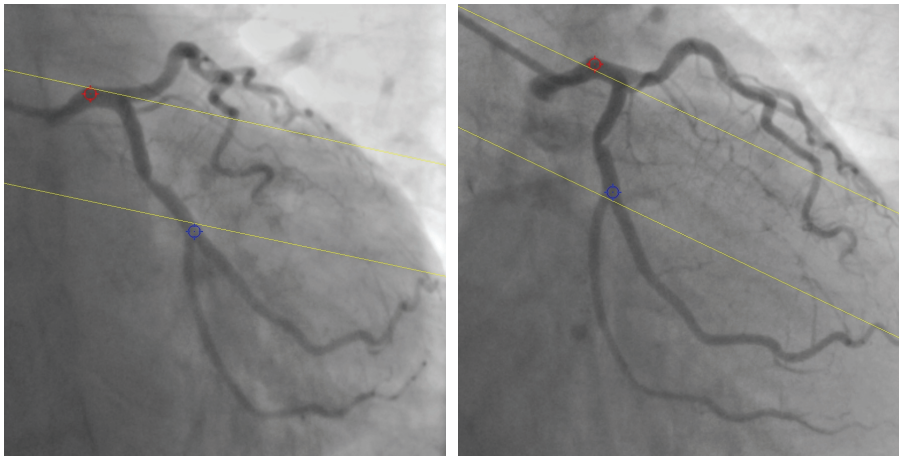

Figure 6-1. System distortion in the image geometry for the 3D reconstruction: Left image is the first projection view (1 RAO, 34 Caudal); Right image is the second projection view (28 RAO, 26 Caudal). The epipolar lines did not go through their corresponding reference points, being the red and blue landmarks.

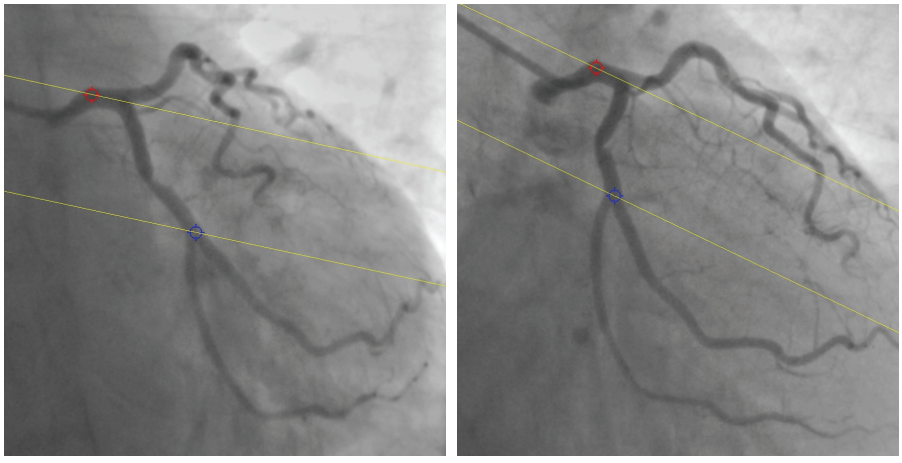

Figure 6-2. Automated correction of system distortion in the image geometry for the 3D reconstruction: The epipolar lines went right through their corresponding reference points in both projection views after the correction.

Figure 6-3 (a) and (b) show the extracted 2D lumen contours and derived centerlines for the target vessel in the LCX, superimposed on the first and second projection views, respectively. Figure 6-3 (c) shows the 3D reconstructed target vessel under the view 35 LAO, 37 Caudal. The target vessel segment has a 3D length of 16.24 mm, a percent area obstruction of 59.4% and derived percent diameter obstruction of 39.5%.

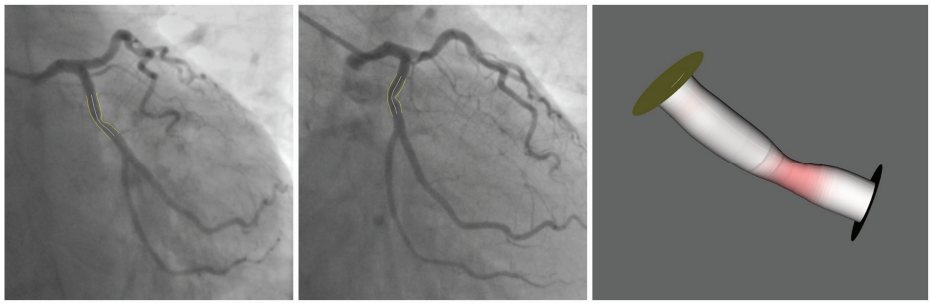

Figure 6-3. The extracted 2D contours and the 3D reconstructed target vessel: (a) and (b) are the two projection views with the superimposed 2D contours and centerlines; (c) is the 3D reconstructed target vessel under 35 LAO, 37 Caudal.

6.2.3 The determination of optimal viewing angles

After the 3D reconstruction has been carried out, the amount of foreshortening of the target vessel for a selected view can easily be determined from the reconstructed centerlines. Given a viewing rotation angle α and angulation angle β, the percentage of foreshortening P_f for a set of centerline pieces C, being the lines connecting two consecutive centerline points, is calculated by the following formula:

$$P_f(\alpha,\beta)=\frac{\sum_{i=1}^{n}|c_i|\left(1-\sin(\theta_i)\right)}{\sum_{i=1}^{n}|c_i|}\times 100\% \qquad (1)$$

, where c_i is the tangent vector of the i-th centerline piece and θ_i is the angle between c_i and the viewing vector associated with the viewing angle of α and β.

Those viewing angles characterized by minimal percentage of foreshortening of the diseased part (e.g. stented subsegment) of the target vessel are selected as candidate viewing angles. In our implementation, the regression plane, that intersects the center of the target vessel, is first calculated based on the condition that the sum of the distances from the plane to all the centerline points of the target vessel is maximized. Then, the 5 viewing angles on the regression plane with minimum foreshortening and at least 15 degrees apart were automatically selected as the candidate viewing angles.

In the next step, we propose a novel algorithm to predict the overlap between the diseased part of the target vessel and other unreconstructed coronary segments under each of the selected candidate viewing angles. Based on such data one can exclude or better reject those viewing angles associated with significant overlap, i.e., overlap between the target vessel

and major coronary arteries or their main branches, which could in practice significantly influence the visibility of the target vessel.

The principle of the overlap prediction algorithm can best be described and later illustrated by using the image geometry in the angiographic projection. Suppose that the target vessel overlaps with a vessel segment *S* under a particular viewing direction *n*. If the target vessel is virtually shifted in 3D along the viewing direction *n,* it will eventually intersect with segment *S*, and this can be checked by their projections from the two available angiographic views. On the contrary, if the two projections of the shifted target vessel in the two angiographic views never intersect with segment *S* at the same time, while the target vessel is shifted virtually along the viewing direction *n*, there will be no overlap between the target vessel and segment *S* in the viewing direction *n*.

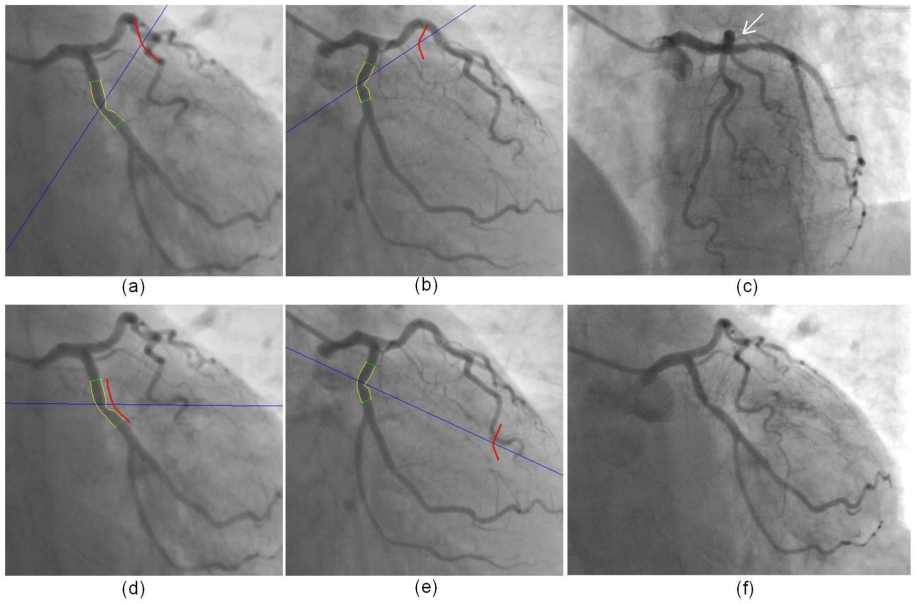

Figure 6-4. Comparisons of the predicted results from the overlap prediction algorithm with the true overlap in the available angiographic views: (a) and (b) predicted that the proximal part of the target vessel overlapped with the mid LAD under the viewing angle of 29 LAO, 18 Cranial; (c) shows the angiographic image acquired at this view of 29 LAO, 18 Cranial, confirming that the proximal part of the target vessel overlaps with the mid LAD; (d) and (e) predicted that there was no overlap of the target vessel with the unreconstructed vessel segments under the viewing angle of 1 LAO, 34 Caudal; (f) shows the angiographic image acquired at 1 LAO, 34 Caudal; conclusion: there is no overlap.

The aforementioned conceptualization can best be illustrated by the example of Figure 6-4. The trajectory (the blue lines going though the center of the target vessel) corresponding to the specified viewing angle is

projected onto each of the two angiographic views that were used for the 3D reconstruction, e.g., Figure 6-4 (a) and (b). The target vessel (represented by means of its centerline in the two angiographic views) is shifted virtually along the trajectory and the possible overlap can be determined by the way the shifted target vessels intersect with the projections of other vessel segments in the two angiographic views. In this case, the algorithm predicted significant overlap of the target vessel with the mid left anterior descending (LAD) artery under the view of 29 LAO, 18 Cranial, because the shifted target vessels, represented by the short curves colored in red in Figure 6-4 (a) and (b), intersected with the mid LAD at the same time. Figure 6-4 (c) shows the angiographic image acquired at that particular view of 29 LAO, 18 Cranial, and this confirms that the proximal part of the target vessel overlaps with the mid LAD (indicated by the arrow). Figure 6-4 (d) and (e) predicted that there was no overlap of the target vessel with other unreconstructed vessel segments under the view of 1 LAO, 34 Caudal, because the shifted target vessels never intersected with the same vessel segment at the same time. Figure 6-4 (f) shows the angiographic image acquired at 1 LAO, 34 Caudal, and clearly, the target vessel does not have any overlap with other vessel segments.

6.2.4 Validation of overlap prediction

For each patient studied, 3 to 6 angiographic projections (hereafter denoted as TEST views) were selected to validate the accuracy of the proposed overlap prediction algorithm; the number of TEST views were dependent on the total number of views recorded for a particular patient. The selection procedure was performed before the 3D angiographic reconstruction took place to guarantee that it was a blinded procedure. Next, the 3D target vessel was reconstructed and its overlap condition, i.e., whether the target vessel had any overlap with other vessel segments or not, under each of the TEST views was calculated by the prediction algorithm. The results were then compared with the true overlap condition in the available angiographic projections.

6.2.5 Validation of optimal viewing angles

The difference in the optimal viewing angles determined by the proposed approach (hereafter denoted as Software Viewing Angle, SVA) and the viewing angles used during the stent deployment in the actual intervention (hereafter denoted as Expert Viewing Angle, EVA) was determined by calculating the angle between the viewing vectors associated with SVA and EVA, respectively. In addition, the percentages of

foreshortening of the target vessel under the SVA and EVA were calculated and compared.

Two interventional cardiologists with 12 and 8 years of experience in interventional cardiology independently evaluated the success of SVA, with respect to EVA. After carefully reviewing all the angiographic projections for each patient and the 3D reconstructed target vessel under the different viewing angles, the interventional cardiologists were requested to choose one of the following five candidate options:

1) SVA is significant worse than EVA;
2) SVA is slightly worse than EVA;
3) SVA is not much different from EVA;
4) SVA is slightly better than EVA;
5) SVA significant better than EVA.

These five candidate options were graded into five values ranging from -2 to 2 with a step of 1. The average graded value of the two interventional cardiologists was defined as the score point for the evaluated case. The sign of the score point indicates which viewing angle is better: positive for the viewing angle determined by the proposed approach and negative for the viewing angle used during the actual intervention.

6.3 Statistics

Quantitative data were presented as mean ± standard deviation, while the accuracy of the overlap prediction was presented as the percentage of successful predictions for all TEST views. The foreshortening of the target vessel under SVA and EVA were compared using the paired *t*-test. The sign of the score point for the evaluation of the success of SVA with respect to EVA was tested by using the Wilcoxon Signed Ranks test. A 2-sided *p*-value of <0.01 was considered to be significant. All statistical analyses were carried out by using a statistical software package (SPSS, version 16.0; SPSS Inc; Chicago, IL, USA).

6.4 Results

6.4.1 Overlap prediction

A total of 235 TEST views from 67 patients were selected to validate the accuracy of the proposed overlap prediction algorithm. The algorithm successfully predicted the overlap condition for all the 235 TEST views. The accuracy of overlap prediction, therefore, was 100%.

6.4.2 Optimal viewing angle

In 16 (23.9%) of the cases both interventional cardiologists decided that SVA was significant better than EVA, while in none of the cases the interventional cardiologists found SVA worse than EVA. The frequencies of the graded evaluation results from the two interventional cardiologists are presented in Figure 6-5. Note also that the two interventional cardiologists scored very similar. In addition, one can say that in about 60% of the cases they clearly favor the SVA approach. The average score point for the success of SVA with respect to EVA was 0.94±0.80. Statistical tests showed that the sign of the score point was positive ($p < 0.001$), indicating that the interventional cardiologists were in favor of the viewing angles determined by the proposed approach as compared to the viewing angles used during the actual intervention.

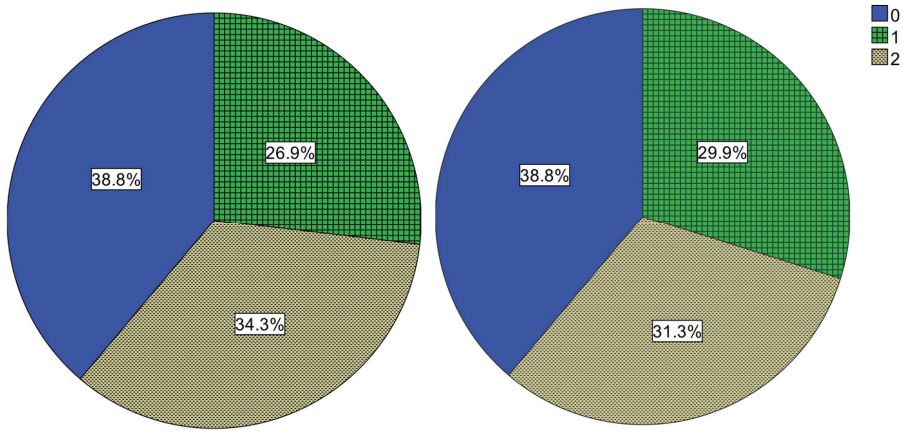

Figure 6-5. The proportions of the graded evaluation results from the two interventional cardiologists: Left is from the first cardiologist; Right is from the second cardiologist.

The difference in SVA and EVA ranged from 2.1º to 54.1º, with an average difference of 22.3º±12.3º. The percentage of foreshortening of the target vessels under SVA ranged from 0.2% to 7.4%, with an average value of 1.6%±1.5%, while the percentage of foreshortening of the same target vessels under EVA ranged from 0.4% to 40.1%, with an average value of 8.9%±8.2%. In other words, the viewing angles used during the actual intervention were associated with a much higher percentage of foreshortening than the optimal viewing angles determined by the proposed approach (Difference: 7,2%±8.2%, $p < 0.001$). The average foreshortening under EVA in the LAD, LCA, and RCA were 7.5%±7.1%, 11.1%±7.6%, and 9.3%±10.2%, respectively. The frequencies of EVA

associated with <10%, 10%-20%, and >20% foreshortening in different coronary segments are presented in Figure 6-6. In all, 7 (10.4%) target vessel had more than 20% foreshortening in the image projections during the actual intervention, while 19 (28.4%) target vessels had 10%-20% foreshortening and 41 (61.2%) target vessels had less than 10% foreshortening. On the contrary, in 60 (89.6%) target vessels had less than 3% foreshortening under the viewing angles proposed by our approach.

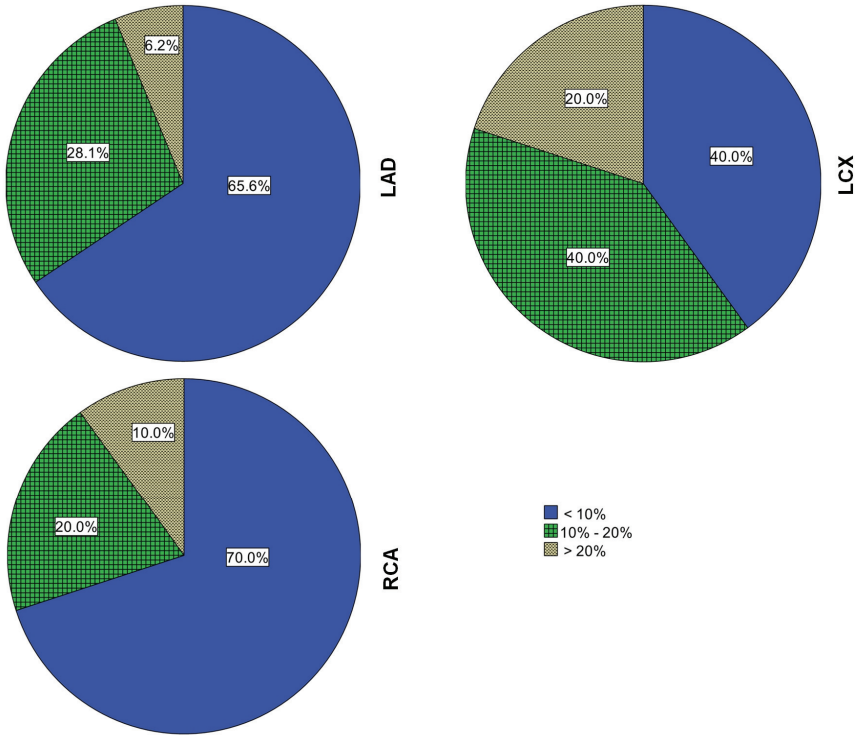

Figure 6-6. The proportions of EVA associated with different vessel foreshortening in the LAD, LCX, and RCA.

Scatter plots for the distributions of SVA and EVA in different coronary segments are presented in Figure 6-7. The data suggest that the distribution of EVA is more concentrated than SVA, reflecting the fact that in general the interventionalists choose one of the more commonly used angiographic viewing angles [16] and only slightly adjust it to use in the stent deployment. On the contrary, SVA distributes more evenly, indicating that there is significant variability in the optimal viewing angles based on the actual anatomy of the individual patient.

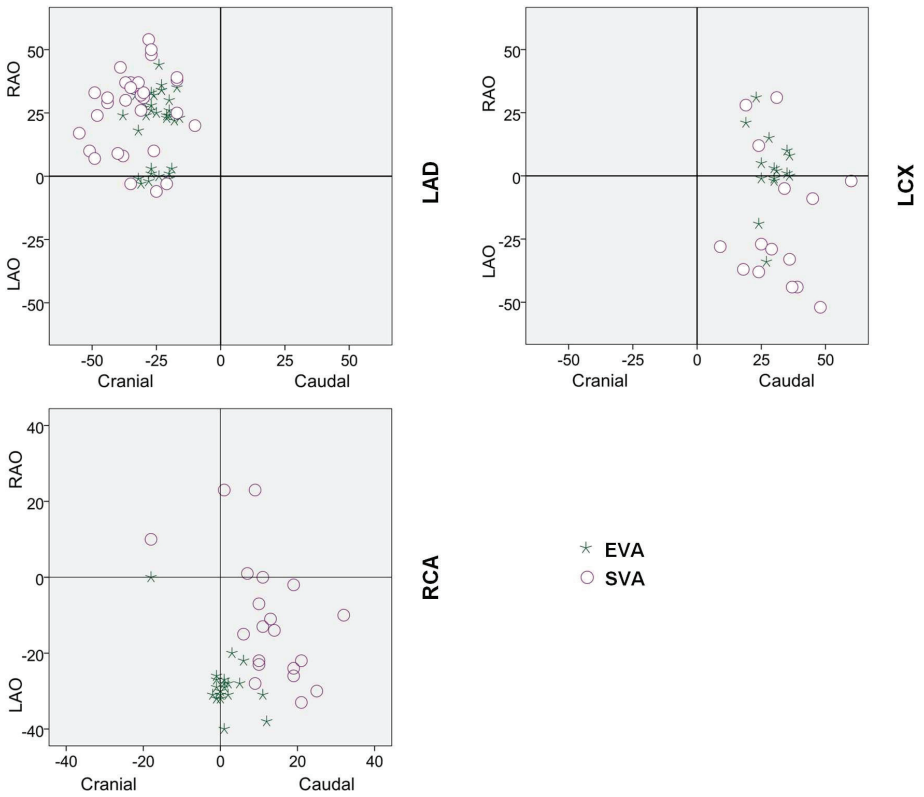

Figure 6-7. The distributions of SVA and EVA in the LAD, LCX, and RCA.

6.5 Discussions

Drug-eluting stents (DES) have proven to be able to reduce the in-stent restenosis rate after the intervention [17-19]; however, the efficacy depends on complete lesion coverage, and therefore requires appropriate stent selection and deployment techniques [1,20]. The ad hoc solution of deploying additional stents when the first-select stent turns out to be of insufficient length or being deployed at suboptimal positions could reduce the minimum stent area and increase the dose of drug released in the overlapping area, which have been demonstrated to be associated with increased risks of restenosis and thrombosis [21]. In addition, the suboptimal stent deployment due to the unreliability in achieving the optimal viewing angle could result in undesirable results, e.g., stent protrusion into the main vessel or incomplete lesion coverage at the ostium when stenting the obstructed segment at the ostium of a sidebranch [2]. In routine clinical practice, the optimal viewing angle is subjectively selected by adjusting the rotation angle (LAO/RAO) and angulation angle (Cranial/Caudal) of the X-ray gantry. This "trial-and-error" approach could significantly increase the amount of contrast

medium administration and the radiation exposure to the patient and staff. Besides, due to the variable anatomy of the individual patient combined with the variable orientation of the heart in the thorax, there is no guarantee that the chosen angle will optimally visualize the target vessel during the stent deployment. In some cases, the identification of optimal viewing angles based on 2D angiographic projections is extremely challenging. Computer-aided stent selection and positioning are thus of great importance for support of coronary interventions in catheterization laboratories, especially with the increasing complexity of coronary interventions.

Three-dimensional quantitative coronary angiography based on routine angiographic projections has emerged as a new tool to increase the assessment capabilities for both diagnostic and interventional cardiology. It has been presented that by resolving a number of additional limitations of standard two-dimensional (2D) analysis [11,22], such as elimination of foreshortening and out-of-plane magnification error [23], 3D QCA could be used to accurately assess the vessel segment length [24-27] and change the decision making in stent selection [24]. In addition, the 3D angiographic reconstruction enables the subsequent automated determination of optimal viewing angles, which has been demonstrated to be associated with much less vessel foreshortening as compared to the operator-selected views [9] and hence, to enhance the capacities for the support of coronary interventions.

Despite the many advantages that have been demonstrated by using 3D angiographic reconstruction to determine the optimal viewing angles [6-9], the practical usage has been hampered by the fact that the calculation of optimal viewing angles with minimal foreshortening does not say anything about possible overlap with other vessel segments, rendering such optimal view possibly useless. To actually calculate the possible overlap with other segments would require the reconstruction of the whole coronary tree in 3D. Since the reconstruction of the whole coronary tree from routine angiographic acquisitions not only requires a significant amount of time, but also imposes significant requirements on the angiographic image quality, e.g., without significant overlap between any of two visualized vessel segments, it is difficult to apply this approach in routine clinical practice.

To come up with an efficient and pragmatic solution, we have developed a new approach to determine the optimal viewing angles ànd minimize any possible overlap; in our approach we only need to reconstruct the target vessel. This new algorithm can easily predict the overlap conditions of the target vessel and other unreconstructed vessel segments, without the need to reconstruct the whole coronary tree in 3D.

The execution time for the whole 3D reconstruction and overlap prediction is less than 1 minute on a standard PC. Although the calculation of optimal viewing angles could not reduce the need of multiple views to thoroughly study the lesion in pre-intervention, it provides the best view for the stent deployment and positioning during the intervention, which could be extremely difficult to realize based on the 2D X-ray angiography, especially in complex bifurcation stenting procedures. An example case can be observed in stenting the ostium of the sidebranch [28]: inappropriate view used in stent deployment might lead to stent protrusion into the main vessel or incomplete stent coverage at the ostium. Figure 6-8 shows the 3D reconstructed bifurcation under different viewing angles. Figure 6-8 (a) and (b) show the angiographic view and the 3D reconstructed bifurcation under 31 RAO, 33 Cranial, respectively. It is very clear from the 3D view that the visualization of the ostium of the diagonal branch is not optimal. Positioning a stent at the ostium of the diagonal branch based on this viewing angle might result in undesirable results. Figure 6-8 (c) shows the 3D bifurcation under the optimal viewing angle of 40 LAO, 56 Cranial. The visualization of the ostium of the diagonal branch has greatly improved and optimized.

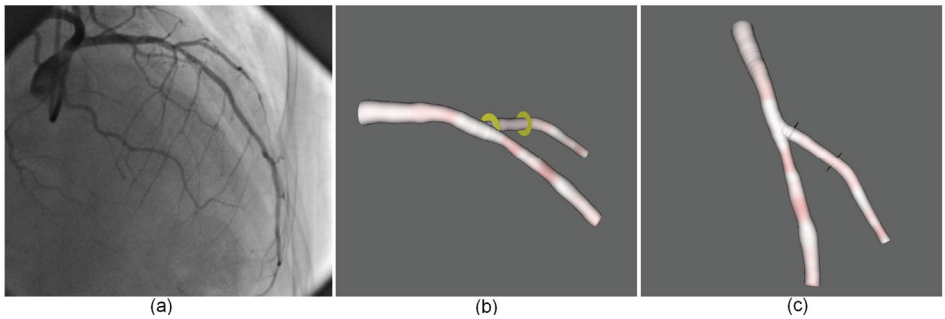

Figure 6-8. The visualization of a bifurcation under different views: (a) is the angiographic view under 31 RAO, 33 Cranial; (b) is the 3D reconstructed bifurcation under 31 RAO, 33 Cranial; (c) is the 3D reconstructed bifurcation under the optimal viewing angle of 40 LAO, 56 Cranial.

In 60 (89.6%) of 67 target vessels in our study population, the proposed approach was able to determine the optimal viewing angles with less than 3% foreshortening and without overlap with major coronary branches which could influence the visibility of the target vessel; On the other hand, the experienced interventionalists were able to select a view with less than 3% foreshortening in only 19 (28.4%) target vessels and with more than 10% foreshortening in 26 (38.8%) target vessels. The optimal imaging of the LCX based on the experience of the interventionalists was the most challenging: 60% of the target vessels had more than 10% foreshortening under the viewing angles used during

the actual intervention. These findings were similar to the results presented by Green in [9]. The difference was that we found that the LAD, instead of the RCA, had the least foreshortening under the viewing angles used during the actual intervention. This difference could be partly explained by the facts that different data were used and different interventionalists were involved in these two studies. We would also like to point out that 19 angiograms were excluded from their study due to the technical insufficiency for the 3D reconstruction of the whole coronary tree, while only 1 angiogram of insufficient acquisitions for the 3D reconstruction of the target vessel needed to be excluded in our study.

One major limitation of this work is that it was a retrospective study and hence, the observers were not blinded to the approach when comparing the two different viewing angles. Therefore, prospective studies are still needed to fully validate the advantages of the proposed approach in stent deployment and positioning during coronary interventions. However, the current results are very encouraging.

6.6 Conclusions

The proposed overlap prediction algorithm can accurately predict the overlap condition between the target vessel and the unreconstructed vessel segments. Our new approach is able to accurately and quickly determine the optimal viewing angles, which makes it suitable for the on-line support of coronary interventions.

6.7 References

1. Costa MA, Angiolillo DJ, Tannenbaum M, et al. Impact of stent deployment procedural factors on long-term effectiveness and safety of sirolimus-eluting stents (final results of the multicenter prospective STLLR trial). Am J Cardiol 2008; 101:1704–1711.
2. Lemos PA, Saia F, Ligthart JM, et al. Coronary restenosis after sirolimus-eluting stent implantation: morphological description and mechanistic analysis from a consecutive series of cases. Circulation 2003; 108:257–260.
3. Aminian A, Kabir T, Eeckhout E. Treatment of drug-eluting stent restenosis: An emerging challenge. Catheter Cardiovasc Interv 2009; 74:108–116.
4. Colombo A, Stankovic G, Moses JW. Selection of coronary stents. J Am Coll Cardiol 2002; 40:1021–1033.
5. Dumay AM, Reiber JHC, Gerbrands JJ. Determination of optimal angiographic viewing angles: basic principles and evaluation study. IEEE Trans Med Imaging 1994; 13:13–24.
6. Tu S, Koning G, Jukema W, et al. Assessment of obstruction length and optimal viewing angle from biplane X-ray angiograms. Int J Cardiovasc Imaging 2010; 26:5–17.
7. Sadamatsu K, Sagara S, Yamawaki T, et al. Three-dimensional coronary imaging for the ostium of the left anterior descending artery. Int J Cardiovasc Imaging 2009; 25:223–228.
8. Garcia JA, Movassaghi B, Casserly IP, et al. Determination of optimal viewing regions for X-ray coronary angiography based on a quantitative analysis of 3D reconstructed models. Int J Cardiovasc Imaging 2009; 25:455–462.

9. Green NE, Chen SY, Hansgen AR, et al. Angiographic views used for percutaneous coronary interventions: a three-dimensional analysis of physician-determined vs. computer-generated views. Catheter Cardiovasc Interv 2005; 64:451– 459.
10. Wahle A, Wellnhofer E, Mugaragu I, et al. Assessment of Diffuse Coronary Artery Disease by Quantitative Analysis of Coronary Morphology Based upon 3-D Reconstruction from Biplane Angiograms. IEEE Trans Med Imaging 1995; 14:230–241.
11. Reiber JHC, Serruys PW, Kooijman CJ, et al. Assessment of short-, medium-, and long-term variations in arterial dimensions from computer-assisted quantitation of coronary cineangiograms. Circulation 1985; 71:280–288.
12. Janssen JP, Koning G, De Koning PJH, et al. A new approach to contour detection in X-ray arteriograms: The wavecontour. Investigative radiology 2005; 40:514–520.
13. Reiber JHC, Zwet PM van der, Koning G, et al. Accuracy and precision of quantitative digital coronary arteriography: observer-, short-, and medium-term variabilities. Cathet Cardiovasc Diagn 1993; 28:187–198.
14. Tu S, Koning G, Tuinenburg JC, et al. Coronary angiography enhancement for visualization. Int J Cardiovasc Imaging 2009; 25:657–667.
15. Dumay ACM. Image Reconstruction from Biplane Angiographic Projections. Dissertation 1992, Delft University of Technology.
16. Mario CD, Sutaria N. Coronary angiography in the angioplasty era: projections with a meaning. Heart 2005; 91:968–976.
17. Moses JW, Leon MB, Popma JJ, et al. Sirolimus-eluting stents versus standard stents in patients with stenosis in a native coronary artery. N Engl J Med 2003; 349:1315–1323.
18. Stone GW, Ellis SG, Cox DA, et al. A polymer-based, paclitaxel-eluting stent in patients with coronary artery disease. N Engl J Med 2004; 350:221–231.
19. Stone GW, Moses JW, Ellis SG, et al. Safety and efficacy of sirolimus- and paclitaxel-eluting coronary stents. N Engl J Med 2007; 356:998–1008.
20. Fujii K, Carlier SG, Mintz GS, et al. Stent underexpansion and residual reference segment stenosis are related to stent thrombosis after sirolimus-eluting stent implantation: An intravascular ultrasound study. J Am Coll Cardiol 2005; 45:995–998.
21. Finn AV, Kolodgie FD, Harnek J, et al. Differential response of delayed healing and persistent inflammation at sites of overlap sirolimus- or paclitaxel-eluting stents. Circulation 2005; 112:270–278.
22. Lansky A, Tuinenburg J, Costa M, et al. Quantitative Angiographic Methods for Bifurcation Lesions: A Consensus Statement from the European Bifurcation Group. Catheter Cardiovasc Interv 2009; 73:258–266.
23. Koning G, Hekking E, Kemppainen JS, et al. Suitability of the Cordis StabilizerTM marker guide wire for quantitative coronary angiography calibration: An in vitro and in vivo study. Catheter Cardiovasc Interv 2001; 52:334–341.
24. Gollapudi RR, Valencia R, Lee SS, et al. Utility of three-dimensional reconstruction of coronary angiography to guide percutaneous coronary intervention. Catheter Cardiovasc Interv 2007; 69:479–482.
25. Rittger H, Schertel B, Schmidt M, et al. Three-dimensional reconstruction allows accurate quantification and length measurements of coronary artery stenoses. EuroIntervention 2009; 5:127–132.
26. Bruining N, Tanimoto S, Otsuka M, et al. Quantitative multi-modality imaging analysis of a bioabsorbable poly-L-lactid acid stent design in the acute phase: a comparison between 2 and 3D-QCA, QCU and QMSCT-CA. EuroIntervention 2008; 4:285–291.

27. Tu S, Huang Z, Koning G, et al. A novel three-dimensional quantitative coronary angiography system: In-vivo comparison with intravascular ultrasound for assessing arterial segment length. Catheter Cardiovasc Interv 2010; 76: 291–298.
28. Vigna C, Biondi-Zoccai G, Amico CM, et al. Provisional T-drug-eluting stenting technique for the treatment of bifurcation lesions: clinical, myocardial scintigraphy and (late) coronary angiographic results. J Invasive Cardiol 2007; 19:92–97.

CHAPTER 7

In-vivo Assessment of Bifurcation Optimal Viewing Angles and Bifurcation Angles by Three-dimensional (3D) Quantitative Coronary Angiography

This chapter was adapted from:

In-vivo Assessment of Bifurcation Optimal Viewing Angles and Bifurcation Angles by Three-dimensional (3D) Quantitative Coronary Angiography
Shengxian Tu, Jing Jing, Niels R. Holm, Kevin Onsea, Tao Zhang, Tom Adriaenssens, Christophe Dubois, Walter Desmet, Leif Thuesen, Yundai Chen, Johan H. C. Reiber

International Journal of Cardiovascular Imaging
Epub Ahead of Print

ABSTRACT

Background: Evaluation and stenting of coronary bifurcation lesions may benefit from optimal angiographic views. The anatomy-defined bifurcation optimal viewing angle (ABOVA) is characterized by having an orthogonal view of the bifurcation, such that overlap and foreshortening at the ostium are minimized. However, due to the mechanical constraints of the X-ray systems, certain deep angles cannot be reached by the C-arm. Therefore, second best or, so-called obtainable bifurcation optimal viewing angle (OBOVA) has to be used as an alternative. This study assessed the distributions of ABOVA and OBOVA using 3D quantitative coronary angiography (QCA) in a typical patient population. In addition, the bifurcation angles in four main coronary bifurcations were assessed and compared.

Methods: Patients with obstructive coronary bifurcation disease were included in this multicenter registry. A novel and validated 3D QCA software package was applied to reconstruct the bifurcations and to calculate the bifurcation angles in 3D. A list of optimal viewing angle candidates including ABOVA was also automatically proposed by the software. In a next step, the operator selected the best viewing angle as OBOVA, while applying a novel overlap prediction approach to assure no overlap between the target bifurcation and other major coronary arteries.

Results: A total of 194 bifurcations from 181 patients were assessed. The ABOVA could not be reached in 56.7% of the cases; being 40 (81.6%), 40 (78.4%), 9 (17.6%), and 21 (48.8%) cases for LM/LAD/LCx, LAD/Diagonal, LCx/OM, and PDA/PLA, respectively. Both ABOVA and OBOVA distributed sparsely with large ranges of variance: LM/LAD/LCx, 5±33 RAO, 47±35 Caudal versus 4±39 LAO, 35±16 Caudal; LAD/Diagonal, 4±38 RAO, 50±14 Cranial versus 14±28 LAO, 33±5 Cranial; LCx/OM, 21±32 LAO, 27±17 Caudal versus 18±31 LAO, 25±13 Caudal; PDA/PLA, 34±21 LAO, 36±21 Cranial versus 28±25 LAO, 29±15 Cranial. LM/LAD/LCx had the smallest proximal bifurcation angle (128° ±24°) and the largest distal bifurcation angle (80° ±21°), as compared with LAD/Diagonal (151° ±13° and 48° ±16°), LCx/OM (146° ±18° and 57° ±16°), and PDA/PLA (145° ±19° and 59° ±17°).

Conclusion: Large variabilities in optimal viewing angles existed for all main coronary bifurcations. The anatomy-defined bifurcation optimal viewing angle could not be reached in-vivo in roughly half of the cases due to the mechanical constraints of the current X-ray systems. Obtainable bifurcation optimal viewing angle should be provided as an alternative or second best. The bifurcation angles in the left main bifurcation demonstrated the largest variabilities.

7.1 Introduction

Bifurcation lesions are frequent and account for approximately 15% to 20% of all percutaneous coronary interventions (PCI) performed worldwide [1,2]. The treatment remains challenging with a tendency towards increased restenosis and stent thrombosis [3]. Correct assessment of bifurcation lesion anatomy, especially the ostia of branches, is essential in the choice of treatment strategy. Indeed, meticulous positioning of a sidebranch stent is of uttermost importance to ensure complete ostial lesion coverage and to limit the protrusion of the stent in the main vessel. Currently, X-ray coronary angiography is predominantly used in daily routine to establish the diagnosis and guide PCI. The conventional approach for diagnostic angiography uses a rigid set of multiple standard angiographic views [4], while the modern approach requires immediate interpretation of the first angiographic images, followed by the acquisition of those views that maximally expose the lesion severity and preferably with minimal overlap and foreshortening. In order to obtain the optimal views, operators will interactively adjust the rotation angle (left anterior oblique/right anterior oblique, LAO/RAO) and the angulation angle (Cranial/Caudal) guided by the X-ray images. This "trial-and-error" approach could significantly increase the volume of contrast medium used and the radiation exposure to the patient and staff. Besides, due to the variable anatomy of each individual patient combined with the variable orientation of the heart in the thorax, the chosen angle can be quite different from the true optimal viewing angle [5, 6].

Recently developed three-dimensional quantitative coronary angiography (3D QCA) systems enabled the automated determination of bifurcation optimal viewing angles, i.e., the angle characterized by having an orthogonal view of the bifurcation including the ostium, minimizing the vessel foreshortening and overlap [7]. However, this orthogonal view is uniquely determined by the anatomy of the individual bifurcation. Due to the mechanical constraints of the X-ray systems, this anatomy-defined bifurcation optimal viewing angle (ABOVA) might have deep angles, which possibly cannot be reached by the C-arm or might be associated with an unacceptable radiation exposure to the operator. In addition, the possible overlap by other major coronary arteries could significantly influence the visualization of the bifurcation, rendering such an ABOVA less useful [5]. Therefore, second best or, obtainable bifurcation optimal viewing angle (OBOVA) has to be used as an alternative to resolve the aforementioned limitations. This study assessed the distributions of ABOVA and OBOVA using three-dimensional quantitative coronary angiography (3D QCA) in four main coronary bifurcations. The proximal bifurcation angle, i.e., the take-off angle, and the distal bifurcation angle, i.e., the carina angle, at

the end-diastolic (ED) phase in these four main coronary bifurcations were also assessed and compared.

7.2 Methods

7.2.1 Study population

A total of 187 patients with obstructive coronary bifurcation disease in four main coronary bifurcations (LM/LAD/LCx, LAD/Diagonal, LCx/OM, and PDA/PLA) were retrospectively included in this study at three medical centers (Department of Cardiology, Chinese PLA General Hospital, Beijing, China; Department of Cardiology, Aarhus University Hospital, Skejby, Aarhus, Denmark; and Department of Cardiovascular Diseases, University Hospitals Leuven, Leuven, Belgium). Inclusion criteria were: 1) X-ray angiographic images were acquired by digital image intensifiers (flat-panel systems); 2) Two angiographic projections at least 25° apart with the lumen well filled with contrast dye were recorded before the target bifurcation was revascularized; and 3) The bifurcation was not totally occluded.

Angiographic images were recorded by different X-ray systems (AXIOM-Artis, Siemens Medical Systems, Erlangen, Germany; AlluraXper, Philips Medical Systems, Best, the Netherlands; and Innova 3100, GE Medical Systems, USA). X-ray images were stored in DICOM format at a resolution of 512×512 or 1024×1024 pixels. All parameters required by the 3D angiographic reconstruction were automatically recorded by the X-ray systems.

7.2.2 Bifurcation optimal viewing angles

An optimal viewing angle in the X-ray angiographic systems consists of two parts: rotation angle (LAO/RAO) and angulation angle (Cranial/Caudal). In this study, the viewing angle was defined as not reachable by the C-arm if the rotation angle was larger than 90 LAO or 50 RAO, or if the angulation angle was larger than 40 Cranial or 40 Caudal.

Three-dimensional angiographic reconstruction was performed using a novel and validated 3D QCA software package (prototype version, Medis medical imaging systems bv, Leiden, the Netherlands) [8,9]. The 3D bifurcation reconstruction procedure consisted of the following steps: 1) two image sequences acquired at two arbitrary angiographic views with projection angles at least 25° apart were loaded; 2) properly contrast-filled ED frames of these angiographic image sequences were selected; 3) one to three anatomical markers, e.g., bifurcations, were identified as reference points in the two angiographic views for the automated correction of angiographic system distortions [7]; 4) the target bifurcation

was defined and automated 2D lumen edge detection was performed using our extensively validated QCA algorithms [10,11]; and 5) automated 3D reconstruction and modeling techniques were performed. The resulting bifurcation surface modeled with bean-shape cross-sections in the bifurcation core and elliptical cross-sections in the three segments was generated and visualized in a color-coded fashion. Bifurcation angles and a list of optimal viewing angle candidates including the ABOVA were automatically reported. The ABOVA was characterized by having an orthogonal view of the bifurcation [7], and in such a way that the foreshortening and overlap between the main vessel and the sidebranch at the ostium were minimized. However, overlaps by other major coronary arteries could still deteriorate the quality of the projection when using ABOVA as the projection angle. Therefore, in a next step, a novel overlap prediction algorithm described in our previous study [5] was used to predict the overlap condition.

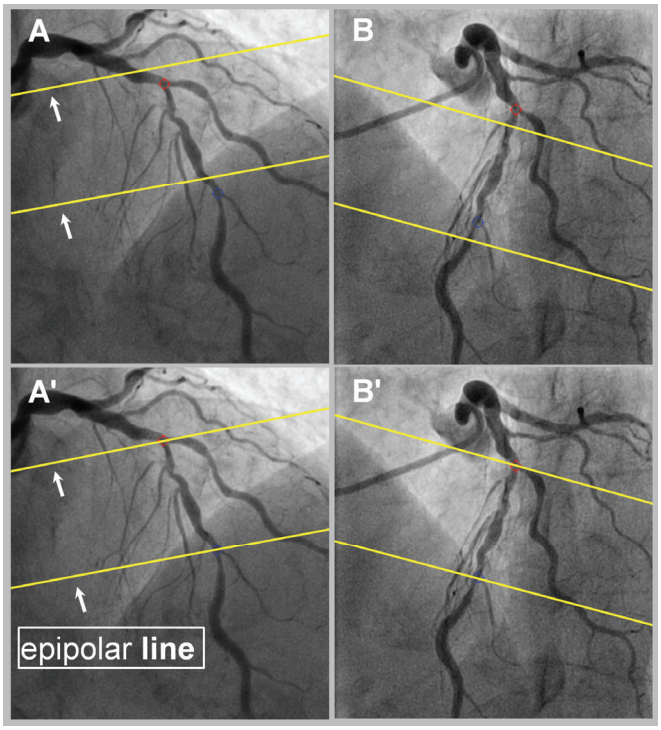

Figure 7-1. Automated correction of system distortions in the image geometry for the 3D angiographic reconstruction: A and B were the two angiographic views (15 RAO, 33 Cranial and 31 LAO, 31 Cranial) used for the 3D reconstruction. The two epipolar lines did not go through their corresponding reference points, being the red and blue landmarks at the bifurcations, indicating system distortions were present. A' and B' show the results after the automated correction of the system distortions: The two epipolar lines now go right through their corresponding red and blue reference points in both angiographic views.

An example of correcting system distortions in the image geometry for the 3D angiographic reconstruction is given in Figure 7-1. The two bifurcations in the left anterior descending artery (LAD) were identified as reference points and their epipolar lines, being the projection of the X-ray beam directed towards a particular point on one of the projections onto the second projection [12], were superimposed in the two angiographic views by Figures 7-1A and 7-1B. Due to the system distortions, the epipolar lines did not go through their corresponding reference points. Figures 7-1A' and 7-1B' show the results after the automated correction of system distortions: The epipolar lines now go right through their corresponding reference points in both angiographic views, demonstrating the success of this automated procedure.

Figure 7-2 shows the two angiographic views with the overlap prediction results and the reconstructed LAD/Diagonal bifurcation in 3D. Figures 7-2A and 7-2B show the two angiographic views (15 RAO, 33 Cranial and 31 LAO, 31 Cranial) with lumen contours superimposed on the LAD/Diagonal bifurcation and the result of the overlap prediction at ABOVA, being 7 RAO, 55 Cranial. The two trajectories (blue lines) in A and B did not intersect with the same region of any major coronary artery in the two angiographic views, indicating that there was no overlap between the obstructed subsegment of the LAD and other major coronary arteries at ABOVA. C shows the reconstructed LAD/Diagonal bifurcation at ABOVA. The proximal and distal bifurcation angles were 161º and 57º, respectively. The subsegment of the LAD between the two green markers had a length of 14.9 mm in 3D and a foreshortening of 4.9% at ABOVA. The overlap between the LAD and the Diagonal at the ostium was minimal. However, despite the fact that this ABOVA is characterized by minimal foreshortening and overlap, this ABOVA cannot be reached by the C-arm for practical, mechanical reasons. Therefore, a second best or, another obtainable viewing angle with limited foreshortening and minimal overlap was selected from the list of optimal viewing angle candidates as OBOVA. In this case, 9 LAO, 40 Cranial was chosen as OBOVA and the LAD/Diagonal bifurcation at OBOVA is shown in C. Although the subsegment of the LAD had more foreshortening at OBOVA as compared with ABOVA (11.4% vs 4.9%), the overlap between the LAD and the Diagonal at the ostium was still minimal. Figures 7-2A' and 7-2B' show the overlap prediction result for the subsegment with other unreconstructed coronary arteries. The shifting centerlines (red curves) along the trajectories (blue lines) in the two angiographic views did not intersect with any major coronary artery at the same time, indicating that there was no overlap between the subsegment of the LAD and other major coronary arteries at OBOVA. In other words, OBOVA was associated with

minimal overlap and slightly more foreshortening as compared with ABOVA. However, a very important practical issue is that it can be reached by the X-ray systems.

The 3D angiographic reconstruction and analyses were performed independently by four well-trained 3D QCA analysts. To guarantee the reliability of the 3D bifurcation reconstruction, all reconstruction results were reviewed by one experienced 3D QCA analyst. If the results were considered unreliable, the cases were excluded. Unreliability was mainly caused by: 1) The anatomical markers, e.g., bifurcations, used to correct system distortions were not accurately identified in the two angiographic images due to vessel overlap; 2) Suboptimal correspondence between the two angiographic views was established when the so-called perspective viewing angle, i.e., the angle between the epipolar line and the long-axis of the vessel [8], was almost zero for the entire vessel segment.

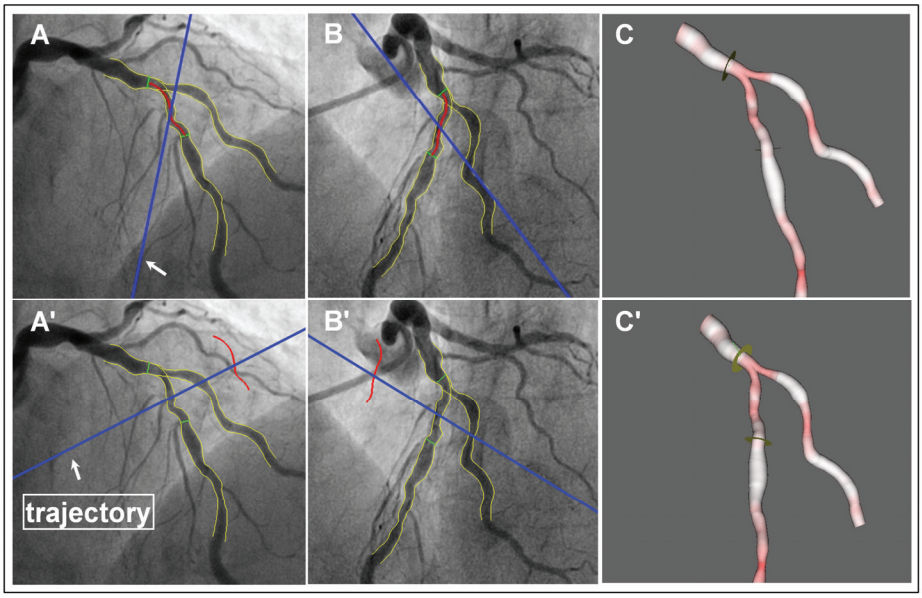

Figure 7-2. 3D reconstructed bifurcation at ABOVA and OBOVA: A and B shows the two angiographic views with lumen contours superimposed on the LAD/Diagonal bifurcation and the overlap prediction result at ABOVA, being 7 RAO, 55 Cranial. The trajectories (blue lines) indicated that there was no overlap between the obstructed subsegment of LAD and other major coronary arteries at ABOVA. C shows the reconstructed bifurcation at ABOVA. The subsegment of LAD between the two green markers had a length of 14.9 mm and a foreshortening of 4.9% at ABOVA. A' and B' shows the overlap prediction result at OBOVA, being 9 LAO, 40 Cranial. The trajectories (blue lines) and the shifting centerlines (red curves) along the trajectories indicated that there was no overlap between the subsegment and other major coronary arteries at OBOVA. C' shows the reconstructed bifurcation at OBOVA. The same subsegment of LAD had a foreshortening of 11.4%. There was no overlap between the LAD and the Diagonal at the ostium.

7.3 Statistics

Quantitative data were presented as mean difference ± standard deviation. Due to the unique anatomy of the left main bifurcation, the comparison of bifurcation angles among the four main coronary bifurcations (groups) was performed by the following procedure: The left main bifurcation group was compared with each of the other three groups using Mann-Whitney U test. In addition, Kruskal-Wallis U test was used initially to test the overall equality of means in the other three groups. Multiple pairwise comparisons of group means were then carried out using Mann-Whitney U test. A 2-sided *p*-value of <0.05 was considered to be significant. All statistical analyses were carried out using SPSS software package (PASW version 18.0.0, 2009; SPSS Inc, Chicago, IL).

7.4 Results

A total of 200 bifurcations with obstructive coronary disease were included for analysis. Of all, the analyses of 6 bifurcations were excluded since the reliability of the 3D bifurcation reconstruction was not approved by the experienced 3D QCA analyst, resulting in a total of 194 bifurcations from 181 patients in the final analyses. Baseline characteristics are given in Table 1. In short, the assessed bifurcations included 49 (25.3%) LM/LAD/LCx, 51 (26.3%) LAD/Diagonal, 51 (26.3%) LCx/OM, 43 (22.2%) PDA/PLA. The ostium of the daughter branches was involved in 147 (75.8%) (main vessel) and 112 (57.7%) (sidebranch).

Table1. Baseline Characteristics

Patient	n = 181
Age	61 (39-88)
Male/Female	145/36
Bifurcation	n = 194
LM/LAD/LCx	49 (25.3%)
LAD/Diagonal	51 (26.3%)
LCx/OM	51 (26.3%)
PDA/PLA	43 (22.2%)
Lesion classifications*	
(1, 0, 0)	14 (7.2%)
(0, 1, 0)	35 (18.0%)
(0, 0, 1)	14 (7.2%)
(1, 1, 0)	33 (17.0%)
(1, 0, 1)	19 (9.8%)
(0, 1, 1)	23 (11.9%)
(1, 1, 1)	56 (28.9%)

*Medina classification by visual assessment. LM = Left Main; LAD = Left Anterior Descending; LCx = Left Circumflex Artery; OM = Obtuse Marginal; RCA = Right Coronary Artery; PDA = Posterior Descending Artery; PLA = Posterolateral Artery.

The overlap of the bifurcation with other major coronary arteries at ABOVA was uncommon. Only 3 PDA/PLA bifurcations had overlap with the proximal right coronary artery (RCA), while the other three main coronary bifurcations had no overlap when projected at ABOVA. However, ABOVA could not be reached in 110 (56.7%) of the cases; being 40 (81.6%), 40 (78.4%), 9 (17.6%), and 21 (48.8%) cases for LM/LAD/LCx, LAD/Diagonal, LCx/OM, and PDA/PLA, respectively. Figure 7-3 and 7-4 show the distributions of ABOVA and OBOVA in the four main coronary bifurcations, respectively. Quantitative data are presented in Table 2. Both ABOVA and OBOVA distributed sparsely with large ranges of variation for all the main coronary bifurcations: LM/LAD/LCx, 5±33 RAO, 47±35 Caudal vs 4±39 LAO, 35±16 Caudal; LAD/Diagonal, 4±38 RAO, 50±14 Cranial vs 14±28 LAO, 33±5 Cranial; LCx/OM, 21±32 LAO, 27±17 Caudal vs 18±31 LAO, 25±13 Caudal; PDA/PLA, 34±21 LAO, 36±21 Cranial vs 28±25 LAO, 29±15 Cranial.

The bifurcation angles could not be calculated in 4 cases of the left main bifurcations due to a very short left main trunk. In the remaining 190 bifurcations, the proximal bifurcation angle (PBA) in LM/LAD/LCx was smaller than any of the other three bifurcations, being 128º±24º vs 151º±13º (p < 0.001) in LAD/Diagonal, 146º±18º (p < 0.001) in LCx/OM, and 145º±19º (p = 0.001) in PDA/PLA, respectively. The distal bifurcation angle (DBA) in LM/LAD/LCx was larger than any of the other three bifurcations, being 80º±21ºvs 48º±16º(p < 0.001) in LAD/Diagonal, 57º±16º (p < 0.001) in LCx/OM, and 59º±17º (p < 0.001) in PDA/PLA, respectively. The PBAs in LAD/Diagonal, LCx/OM, and PDA/PLA were not statistically different (p = 0.133). However, the DBA in LAD/Diagonal was smaller as compared with LCx/OM (p = 0.004) and PDA/PLA (p = 0.001), while the DBAs in LCx/OM and PDA/PLA were not statistically different (p = 0.673).

Table2. Bifurcation Dimensions Assessed by 3D Quantitative Coronary Angiography

	ABOVA		OBOVA		BA	
	Rotation*	Angulation†	Rotation*	Angulation†	PBA	DBA
LM/LAD/LCx	5±33	47±35	-4±39	35±16	128±24‡	80±21
LAD/Diagonal	4±38	-50±14	-14±28	-33±5	151±13	48±16
LCx/OM	-21±32	27±17	-18±31	25±13	146±18	57±16
PDA/PLA	-34±21	-36±21	-28±25	-29±15	145±19	59±17

*Positive value represents Right Anterior Oblique and negative value represents Left Anterior Oblique; †Positive value represents Caudal and negative value represents Cranial. ‡Angle between LM and LCx. ABOVA = Anatomy-defined bifurcation optimal view angle; OBOVA = Obtainable bifurcation optimal viewing angle; BA = Bifurcation angle; PBA = Proximal bifurcation angle; DBA = Distal bifurcation angle.

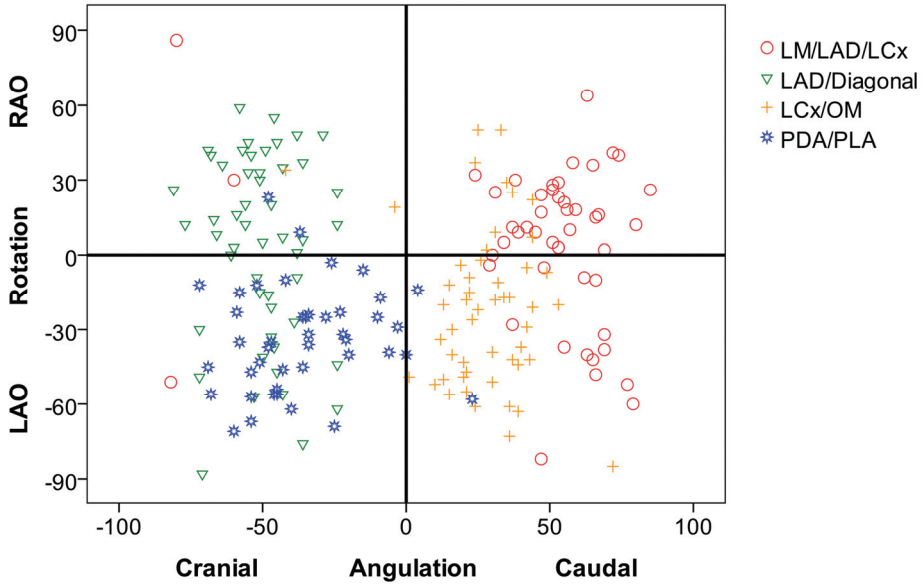

Figure 7-3. The distribution of the anatomy-defined bifurcation optimal viewing angle (ABOVA): The ABOVA distributed sparsely with large ranges of variation for all main coronary bifurcations. n = 194.

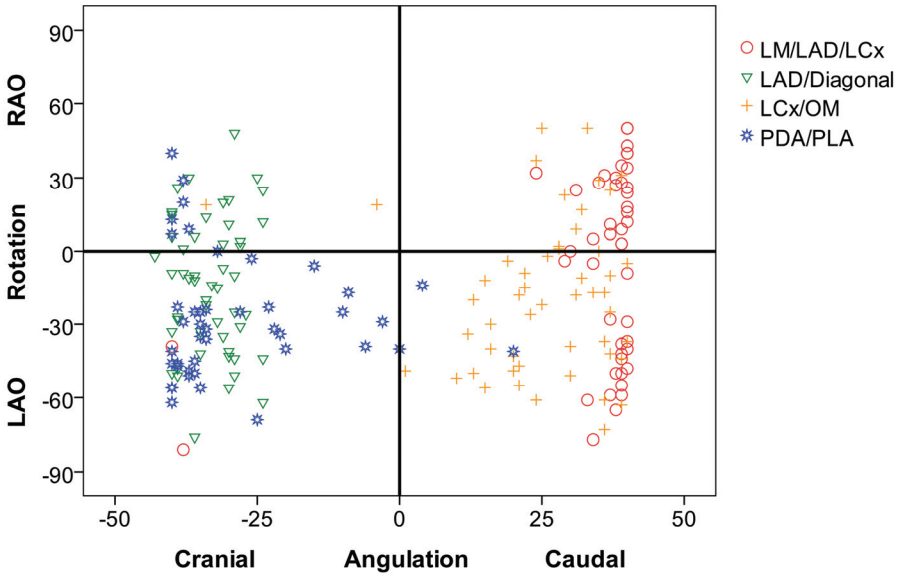

Figure 7-4. The distribution of the obtainable bifurcation optimal viewing angle (OBOVA): The OBOVA distributed sparsely with large ranges of variation for all main coronary bifurcations. n = 194.

7.5 Discussions

This study found that both ABOVA and OBOVA distributed sparsely with large ranges of variation in all main coronary bifurcations, indicating that there are no fixed views that can uniformly optimize the visualization of the main coronary bifurcations. The true bifurcation optimal view is subject to the unique anatomy of each individual bifurcation. Given the fact that the viewing angles should be within the reach of the X-ray systems, the optimal view for the left main bifurcation distributes mainly at the Caudal view (35±16 Caudal) but spreads across the LAO/RAO view (4±39 LAO); the optimal view for LAD/Diagonal distributes mainly at the Cranial view (33±5 Cranial), but spreads across the LAO/RAO view (14±28 LAO); the optimal view for LCx/OM distributes mainly at the Caudal view (25±13 Caudal), but spreads across the LAO/RAO view (18±31 LAO); the optimal view for PDA/PLA distributes mainly at the Cranial view (29±15 Cranial) and the LAO view (28±25).

Three-dimensional quantitative coronary angiography based on routine angiographic projections has emerged as a surrogate to determine optimal viewing angles in the catheterization laboratory. Green [6] evaluated 156 vessel segments and found that vessel foreshortening ranged from 0 to 50% in the expert-recommended views, while the computer-generated optimal views had only 0.5±1.2% foreshortening and less than 2% overlap. Tu [5] evaluated 67 target vessels by applying a novel overlap prediction approach to avoid overlap in the target vessels and found that the expert viewing angle (EVA) was associated with much more foreshortening as compared with the software viewing angle (SVA), being 8.9±8.2% vs. 1.6±1.5% ($p < 0.001$). The success of SVA with respect to EVA was also evaluated by two experienced interventional cardiologists and the results were clearly in favor of SVA. Despite the fact that promising results were demonstrated by this new imaging technique, it should be borne in mind that these results were only applied to straight vessels and hence cannot directly be transferred to the more complex bifurcation anatomy [13]. The automated assessment of vessel foreshortening depends on the type of lesion and the number of affected segments. For correct assessment of lesion severity and subsequent precise stent positioning, it might be more critical to minimize overlap between the main vessel and the sidebranch at the ostium.

In a recent study, Tu [3] proposed to use the orthogonal view of the bifurcation as the bifurcation optimal view, since it minimizes the foreshortening and overlap at the ostium. In addition, atherosclerotic plaques occur preferably at the outer lateral wall of the bifurcation, i.e., the site opposite to the carina, where flow is more turbulent and endothelial shear stress is lower. When plaques do involve the carina,

they are likely to develop at a later stage of atherosclerosis, as a result of circumferential plaque expansion from the lateral wall [14]. Therefore, the orthogonal viewing angle, i.e., ABOVA, might also expose the lesion severity at its maximum. Nevertheless, ABOVA only minimizes the overlap between the main vessel and the sidebranch at the ostium. Other major coronary arteries could also overlap with the target bifurcation when projected at ABOVA, possibly leading to significant impediment of the visualization of the target bifurcation. To our knowledge, the overlap between the main coronary bifurcations and other coronary arteries at ABOVA has not been documented. Therefore, in this study, we applied the overlap prediction approach to investigate whether this overlap would frequently occur in the general population. To our surprise, the overlap of the bifurcation with other major coronary arteries at ABOVA was uncommon. Only 3 PDA/PLA bifurcations overlapped with the proximal RCA, while the other three main coronary bifurcations had no overlap when projected at ABOVA. This finding further enforces the usefulness of ABOVA. However, due to the mechanical constraints of the current X-ray systems, ABOVA could not be reached in 56.7% of the population. This occurred more frequent in LM/LAD/LCx (81.6%) and LAD/Diagional (78.4%), followed by PDA/PLA (48.8%) and was uncommon in LCx/OM (17.6%). These data suggest that in about half of the population, a second optimal view, i.e., OBOVA, should be used as an alternative by the current X-ray systems. When choosing the second optimal view, priority should be given to minimize the overlap between the main vessel and the sidebranch at the ostium and to maximally expose the lesion severity. In other words, OBOVA for the bifurcation might not be the view elongating the ostial segments at the maximum.

To date, very limited evidence regarding with the use of bifurcation optimal viewing angles in coronary angiography is available in literature. Schlundt [15] demonstrated a case in which sidebranch stenting was performed using the on-line 3D reconstruction of the LAD/Diagonal bifurcation to obtain the optimal view with minimal foreshortening and overlap. Sadamatsu [16] reconstructed 18 left main bifurcations in 3D and selected the optimal views based on foreshortening and overlap. The authors reported that the optimal views were superior to the routine projections in all cases. However, the views were selected to optimize the visualization of the ostial LAD, possibly neglecting the visualization of the LCx. Therefore, these views do not represent the optimal views for the left main bifurcation in the general patient population. To our knowledge, the distributions of ABOVA and OBOVA in main coronary bifurcations have not been previously documented.

Another finding of this study is that the proximal bifurcation angles (PBAs) as assessed by 3D QCA in LAD/Diagonal, LCx/OM, and PDA/PLA were very much comparable and not statistically different (p = 0.133), being 151°±13°, 146°±18°, and 145°±19°, respectively. However, the distal bifurcation angles (DBAs) in LAD/Diagonal was smaller than LCx/OM (p = 0.004) and PDA/PLA (p = 0.001), being 48°±16° vs 57°±16°, and 59°±17°, respectively. The left main bifurcation had the smallest PBA (128°±24°) and the largest DBA (80°±21°).

Bifurcation angle is an important baseline anatomical characteristic for many randomized bifurcation studies [17]. At present, however, bifurcation angles have been quantified mainly on the basis of 2D angiographic images, entailing great dependence on the angiographic viewing angle. 3D QCA was proposed to overcome this limitation by measuring the angles in 3D. Tu showed in a bench study that 3D QCA was able to measure bifurcation angles with high accuracy and low variability on a wide range of acquisitions angles [4]. In this study the same 3D QCA software package was used to assess the bifurcation angles in-vivo. Our results are very similar to a previous study by Pflederer [18] who evaluated the natural distribution of DBA in 100 patients using multidetector computer tomography (80º±27º in LM/LAD/LCx, 46º±19º in LAD/Diagonal, 48º±24º in LCx/OM, and 53º±27º in PDA/PLA). However, another study by Girasis [17] evaluated 266 left main bifurcations using another 3D QCA software package and reported smaller PBA (105.9º±21.7º) and larger DBA (95.6º±23.6º), as compared with our results. This can be explained by differences in patients and 3D QCA software packages. Since 3D bifurcation reconstruction based on routine angiographic projections needs to correct for various system distortions in-vivo [3], different software packages addressing this issue in different approaches might generate discrepancy in the assessed dimensions. In addition, there is no official guideline in the acquisition of angiographic images dedicated for 3D QCA in a broad clinical setting, making the interpretation of different clinical studies difficult.

7.6 Limitations

The study is clearly limited by its retrospective in-vivo design. It could therefore not assess whether the applications of bifurcation optimal viewing angles reduced radiation exposure and the volume of contrast medium used, nor improved the diagnosis and outcome of interventional procedures. Further prospective studies and randomized clinical trials are warranted before definite conclusions on the added clinical value of software-guided bifurcation optimal viewing angles can be drawn.

7.7 Conclusions

Large variabilities in optimal viewing angles existed for all main coronary bifurcations. The anatomy-defined bifurcation optimal viewing angle could not be reached in-vivo in roughly half of the cases due to the mechanical constraints of current X-ray systems. Obtainable bifurcation optimal viewing angle should be provided as an alternative or second best. The bifurcation angles in the left main bifurcation demonstrated the largest variabilities.

7.8 References

1. Iakovou I, Ge L, Colombo A. Contemporary stent treatment of coronary bifurcations. J Am Coll Cardiol 2005; 46:1446–1455.
2. Suzuki N, Angiolillo DJ, Kawaguchi R, Futamatsu H, Bass TA, Costa MA. Percutaneous coronary intervention of bifurcation coronary disease. Minerva Cardioangiol 2007; 55:57–71.
3. Lemos PA, Saia F, Ligthart JMR, Arampatzis CA, Sianos G, Tanabe K, et al. Coronary restenosis after sirolimus-eluting stent implantation: morphological description and mechanistic analysis from a consecutive series of cases. Circulation 2003; 108:257–260.
4. Mario CD, Sutaria N. Coronary angiography in the angioplasty era: projections with a meaning. Heart 2005; 91:968–976.
5. Tu S, Hao P, Koning G, Wei X, Song X, Chen A, Reiber JHC. In-vivo assessment of optimal viewing angles from X-ray coronary angiograms. EuroIntervention 2011; 7:112-120.
6. Green NE, Chen SY, Hansgen AR, Messenger JC, Groves BM, Carroll JD. Angiographic views used for percutaneous coronary interventions: a three-dimensional analysis of physician-determined vs. computer-generated views. Catheter Cardiovasc Interv 2005; 64:451– 459.
7. Tu S, Koning G, Jukema W, Reiber JHC. Assessment of obstruction length and optimal viewing angle from biplane X-ray angiograms. Int J Cardiovasc Imaging 2010; 26:5–17.
8. Tu S, Holm N, Koning G, Maeng M, Reiber JHC. The impact of acquisition angle difference on three-dimensional quantitative coronary angiography. Catheter Cardiovasc Interv 2011; 78:214-222.
9. Tu S Holm NR, Koning G, Huang Z, Reiber JHC. Fusion of 3D QCA and IVUS/OCT. Int J Cardiovasc Imaging 2011; 27:197–207.
10. Reiber JHC, Serruys PW, Kooijman CJ, Wijns W, Slager CJ, Gerbrands JJ, Schuurbiers JC, den Boer A, Hugenholtz PG. Assessment of short-, medium-, and long-term variations in arterial dimensions from computer-assisted quantitation of coronary cineangiograms. Circulation 1985; 71:280–288.
11. Joan C. Tuinenburg, Gerhard Koning, Andrei Rareş, Johannes P. Janssen, Alexandra J. Lansky, Johan H. C. Reiber. Dedicated bifurcation analysis: basic principles. Int J Cardiovasc Imaging 2011; 27: 167–174.
12. Dumay ACM. Image Reconstruction from Biplane Angiographic Projections. Dissertation 1992; Delft University of Technology.
13. Lansky A, Tuinenburg J, Costa M, Maeng M, Koning G, Popma J, et al, on behalf of the European Bifurcation Angiographic Sub-Committee. Quantitative angiographic methods for bifurcation lesions: a consensus statement from the European Bifurcation Group. Catheter Cardiovasc Interv 2009; 73:258-266.
14. Giannoglou GD, Antoniadis AP, Koskinas KC, Chatzizisis YS. Flow and atherosclerosis in coronary bifurcations. EuroIntervention 2010; 6(J):16-23.
15. Schlundt C, Kreft JG, Fuchs F, Achenbach S, Daniel WD, Ludwig J. Three-dimensional on-line reconstruction of coronary bifurcated lesions to optimize side-branch stenting. Catheter Cardiovasc Interv 2006; 68:249–253.

16. Sadamatsu K, Sagara S, Yamawaki T, Tashiro H. Three-dimensional coronary imaging for the ostium of the left anterior descending artery. Int J Cardiovasc Imaging 2009; 25:223–228.
17. Girasis C, Serruys PW, Onuma Y, Colombo A, Holmes DR Jr, Feldman TE, Bass EJ, Leadley K, Dawkins KD, Morice MC. 3-Dimensional bifurcation angle analysis in patients with left main disease: a substudy of the SYNTAX trial (SYNergy Between Percutaneous Coronary Intervention with TAXus and Cardiac Surgery). JACC Cardiovasc Interv 2010; 3:41-48.
18. Pflederer T, Ludwig J, Ropers D, Daniel WG, Achenbach S. Measurement of coronary artery bifurcation angles by multidetector computed tomography. Invest Radiol 2006; 41:793-798.

CHAPTER

8

Co-registration of Three-dimensional Quantitative Coronary Angiography and Intravascular Ultrasound or Optical Coherence Tomography

This chapter was adapted from:

Fusion of 3D QCA and IVUS/OCT
Shengxian Tu, Niels R. Holm, Gerhard Koning,
Zheng Huang, Johan H.C. Reiber
International Journal of Cardiovascular Imaging. 2011,
Volume 27, Issue 2, Pages 197-207.

ABSTRACT

Background: The fusion of quantitative coronary angiography (QCA) and intravascular ultrasound (IVUS)/optical coherence tomography (OCT) depends to a great extend on the co-registration of X-ray angiography (XA) and IVUS/OCT. In this work a new and robust three-dimensional (3D) segmentation and registration approach is presented and validated.

Methods and Materials: The approach starts with standard QCA of the vessel of interest in the two angiographic views (either biplane or 2 monoplane views). Next, the vessel of interest is reconstructed in 3D and registered with the corresponding IVUS/OCT pullback series by a distance mapping algorithm. The accuracy of the registration was retrospectively evaluated on 12 silicone phantoms with coronary stents implanted, and on 24 patients who underwent both coronary angiography and IVUS examinations of the left anterior descending artery. Stent borders or sidebranches were used as markers for the validation. While the most proximal marker was set as the baseline position for the distance mapping algorithm, the subsequent markers were used to evaluate the registration error. The correlation between the registration error and the distance from the evaluated marker to the baseline position was analyzed.

Results: The XA-IVUS registration error for the 12 phantoms was 0.03 ± 0.32 mm (p = 0.75). One OCT pullback series was excluded from the phantom study, since it did not cover the distal stent border. The XA-OCT registration error for the remaining 11 phantoms was 0.05 ± 0.25 mm (p = 0.49). For the in-vivo validation, 2 patients were excluded from the study due to insufficient image quality for the analysis. In total 78 sidebranches were identified from the remaining 22 patients and the registration error was evaluated on 56 markers. The registration error was 0.03 ± 0.45 mm (p = 0.67). The error was not correlated to the distance between the evaluated marker and the baseline position (p = 0.73).

Conclusion: The new XA-IVUS/OCT co-registration approach is a straightforward and reliable solution to combine X-ray angiography and IVUS/OCT imaging for the assessment of the extent of coronary artery disease. It provides the interventional cardiologist with detailed information about vessel size and plaque composition at every position along the vessel of interest, making this a suitable tool during the actual intervention.

8.1 Introduction

Over the past decades, the continuous developments in coronary visualization and quantitative systems have been motivated by the increasing need to better understand and assess coronary atherosclerosis and by the on-line need for support of coronary interventions in cardiac catheterization laboratories. Recently developed three-dimensional quantitative coronary angiography (3D QCA) systems aimed to resolve some of the limitations in conventional two-dimensional (2D) analysis [1-3] and hence, to extend its capacity and reliability in assessing the true dimensions of coronary vascular structures. It has been demonstrated that 3D QCA can accurately assess vessel segment length and diameter [4-7], as well as the optimal viewing angles [8-10] for the subsequent interventional procedure. By using 3D QCA and based on such more accurate 3D data, clinical decision making can be affected, thus possibly leading to a more efficient and economic usage of stents in percutaneous coronary intervention (PCI) [11]. This may have significant impact in today's cost-constrained health care systems.

Despite the fact that the 3D angiographic reconstruction has important potential values, the foremost limitation of X-ray angiography-based systems remains the inability to image beyond the vessel lumen as only the contrast lumen is visualized. In other words, the 3D reconstructed vessel remains a lumenogram, though with better 3D capabilities. Thus, early stages of plaque formation may not be evident with X-ray angiography due to the occurrence of coronary artery remodeling [12], and vulnerable plaques cannot be recognized for possible implementations of measures to prevent these from rupturing. These limitations have been well addressed by intracoronary imaging techniques, among which grey scale intravascular ultrasound (IVUS) is a well-established and validated modality. IVUS provides a wealth of information including vessel wall composition, which is crucial to the assessment of coronary atherosclerosis. Later on, the role of intracoronary imaging techniques was greatly enhanced by the radio-frequency data analysis for plaque characterization and optical coherence tomography (OCT) for the assessment of the thin fibrous cap atheromas and malapposition of stent struts. These new imaging techniques have extended the imaging capabilities in the assessment of coronary artery disease. However, the fact that intracoronary imaging does not preserve the natural 3D vessel shape could lead to erroneous interpretations. Although a longitudinal view (L-View) is available in most IVUS/OCT consoles to provide an overview of the pullback series, the presentation of the L-View by stacking cross-sectional images along a straightened version of the catheter

pullback trajectory is a very unnatural way of conceptualization. As a result, the interpretation can be quite challenging.

Given the different but complementary perspectives provided by X-ray angiography (XA) and IVUS/OCT, the fusion/integration of the two imaging modalities by using XA as a roadmap while exploiting detailed vessel wall information from IVUS/OCT will benefit the interpretation of coronary artery disease and the guidance of coronary interventions. Currently, if IVUS/OCT is performed at the diagnostic stage, the treatment planning is determined to a great extent by the IVUS/OCT interpretation. However, since XA fluoroscopy is still the only imaging tool available during stent deployment and positioning; the interventionalist must mentally establish the correspondence between XA and IVUS/OCT images. This spatial corresponding process is not always easy, especially for coronary artery disease at the early stages or for long diffused arteries, when lumen narrowing is not clearly evident and no sidebranch is present at the neighborhood of the lesion. Thus, XA-IVUS/OCT integrated systems are currently requested in the market to better support coronary interventions. The clinical applicability of such fused/integrated systems depends to a great extend on the reliability and robustness of the co-registration approach. Once a reliable correspondence between the X-ray angiography and IVUS/OCT images is established, the issue of fusing/integrating information from the two image modalities becomes relevant.

In the following paragraphs our approach for the 3D angiographic reconstruction and co-registration with IVUS/OCT is described and the results of both phantom and in-vivo validations are presented.

8.2 Three-dimensional Angiographic Reconstruction

Accurate and robust 3D angiographic reconstruction is the foremost important step in the XA-IVUS/OCT co-registration. Early research on 3D reconstruction can be traced back to decades ago [13, 14]. However, clinical systems were announced only in recent years and there have not been widespread acceptance of such systems in routine clinical practice. One of the reasons is due to the fact that mechanical distortions in X-ray systems and noisy angiographic images in routine clinical acquisitions could significantly affect the reliability and robustness of the 3D reconstruction and analysis. For monoplane X-ray angiographic acquisitions, the shift of the whole coronary tree due to the patient's respiration or the non-isocentric condition could greatly deteriorate the system's reliability. Such system distortions should be corrected before or during the 3D angiographic reconstruction.

A number of approaches [13-15] have been proposed to correct for angiographic system distortions. Ideally, a couple of reliable features (landmarks), e.g., catheter tip and sidebranches, should be identified on the two angiographic views as reference points for the correction of system distortions. However, the practical applicability of such approaches in on-line applications has been hampered by the efforts in identifying many reliable features, which turned out to be too time consuming or even impossible to find such reliable features on the two angiographic views, especially when there were many overlaps from different vessel segments. To guarantee the reliability in the identification of reference points has already been a non-trivial task.

To come up with a more practical and attractive workflow, we have developed a new approach by using only one to three reference points for the correction of system distortions. In case of the presence of small perspective viewing angles for noisy angiographic images, the reliability and robustness of the angiographic reconstruction are further improved by constructing a distance transformation matrix and by searching for the optimal corresponding path in the matrix to refine the correspondence between the two angiographic views [8]. The approach has been validated with high accuracy in both phantom and in-vivo datasets [5, 8]. In short, the 3D angiographic reconstruction consists of only a few major steps: 1) load two image sequences acquired at two arbitrary angiographic views at least 25 degrees apart in viewing angles; 2) select the end-diastolic image frames with the vessel lumen well filled with contrast from the two image sequences for the subsequent 3D reconstruction; 3) identify one to three reference points in both angiographic views for the automated correction of system distortions; 4) manually define the vessel segment of interest and extract its contours and centerlines using our extensively validated QCA algorithms [1,16,17] in the two angiographic views; 5) reconstruct the arterial centerline and cross-sections in 3D after refining the correspondence between the two extracted centerlines.

An example of system distortions in the image geometry for the 3D angiographic reconstruction is given in Figure 8-1 (a) and (b). The two bifurcation points (carina) in the left anterior descending artery (LAD) were identified as reference points and their epipolar lines, being the projection of the X-ray beam directed towards a particular point on one of the projections onto the second projection [13], were presented in the two angiographic views (31 RAO, 33 Cranial and 31 LAO, 30 Cranial, respectively). Due to the system distortions, the epipolar lines did not go through their corresponding reference points. After applying the automated correction of the system distortions, as shown in Figure 8-1 (c) and (d), the epipolar lines now go right through their corresponding

reference points in both angiographic views, demonstrating the success of this automated procedure.

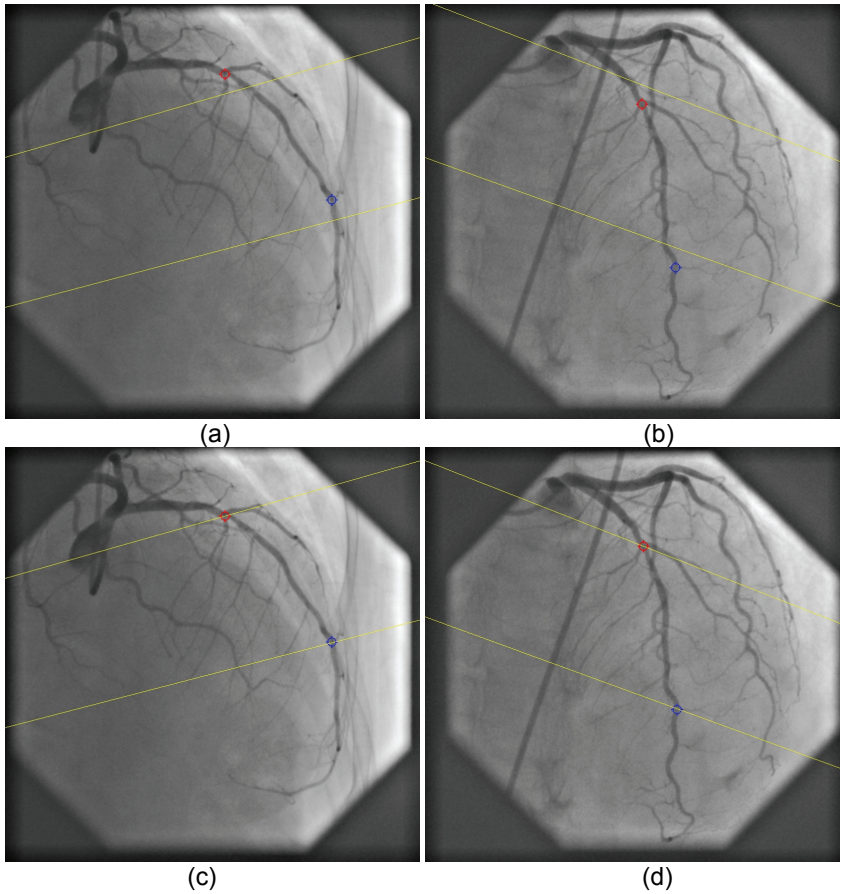

Figure 8-1. Automated correction of system distortions in the image geometry for the 3D angiographic reconstruction: (a) and (b) are the two angiographic views (31 RAO, 33 Cranial and 31 LAO, 30 Cranial) selected for the 3D reconstruction. Before the correction, the two epipolar lines did not go through their corresponding reference points, being the red and blue landmarks. (c) and (d) show the results after the automated correction of the system distortion. The two epipolar lines now go right through their corresponding reference points in both projection views.

Figure 8-2 (a) and (b) show the segment of interest in the LAD and its extracted 2D contours, superimposed on the two angiographic views. Figure 8-2 (c) shows the 3D reconstructed segment of interest under the viewing angle of 29 RAO, 9 Cranial. The subsegment (defined by the two superimposed markers) in the reconstructed vessel has a length of 16.10 mm, per cent diameter obstruction of 38.0%, and per cent area obstruction of 56.7%.

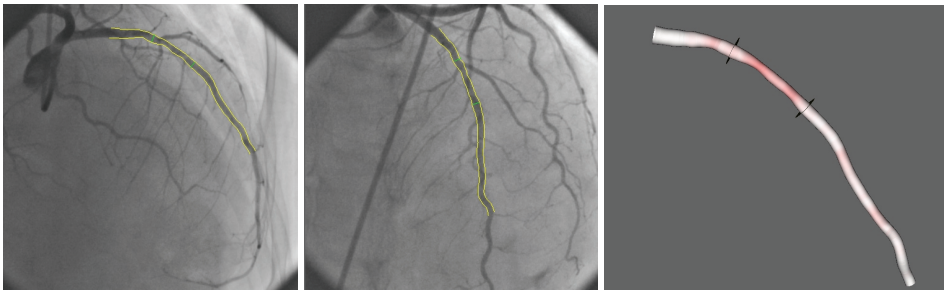

(a) (b) (c)

Figure 8-2. The extracted 2D contours and the 3D reconstructed vessel segment of interest: (a) and (b) are the two angiographic views with the superimposed 2D contours; (c) is the 3D reconstructed vessel segment under 29 RAO, 9 Cranial.

8.3 XA-IVUS/OCT Registration

Under the condition that the motorized transducer pullback with constant speed is used in the IVUS/OCT image acquisition, the rationale for the co-registration of XA images with IVUS/OCT pullback series is to use the spatial relationship between vessel segment (by means of lumen or centerline) and IVUS/OCT pullback trajectory. Conventional registration approaches [18-20] would require the reconstruction of the IVUS/OCT imaging catheter from two angiographic views acquired, and assume it to be the pullback trajectory so that the IVUS/OCT cross-sectional images can be aligned along the trajectory. This is not a trivial task due to the difficulty in segmenting both IVUS/OCT catheter and vessel lumen and the requirement of a second angiographic view for the IVUS/OCT catheter, which is not always included in the current workflow. The assumption of IVUS/OCT transducer path as pullback trajectory could also be jeopardized by the fact that spatial displacement of the catheter could occur inside the vessel after the pullback machine is switched on, in order to reach the state of minimum bending energy. It has been reported that there was significant delay from the moment the IVUS pullback machine was switched on and the moment the transducer tip really started to move [20].

In order to have a rapid and straightforward solution for the on-line XA-IVUS/OCT registration that could assist coronary interventions and would fit most into the current workflow in catheterization laboratories, we have taken a different approach by estimating the corresponding IVUS/OCT cross-sectional image from the reconstructed vessel centerline, based on the curvature information and hence, to skip the reconstruction of the pullback trajectory. The approach only requires the operator to reconstruct the vessel centerline from the angiographic images (which is a standard module in 3D QCA software packages) and register it with IVUS/OCT pullback series by indicating a baseline position in the vessel centerline that corresponds to the same axial position in IVUS/OCT. Such

baseline positions can be found in anatomical or mechanical landmarks visualized in both angiographic and IVUS/OCT images, e.g., sidebranches or stent borders. In case of blurred X-ray angiographic images, image enhancement techniques [21] can be used to increase the visibility of detailed image structures.

Figure 8-3. The XA-OCT co-registration and quantification

After the registration, the markers superimposed on the angiographic views and the IVUS/OCT L-View are now synchronized. The interpretation of vessel dimensions becomes more comprehensive and the interventionalist now knows exactly where to position the stent under the guiding of X-ray images. An example of combing QCA and OCT imaging is given by Figure 8-3. After the registration, the planned stent position (landing zones) defined by the proximal and distal markers has been mapped onto the angiographic views (the two red markers that were superimposed on the angiographic views). In addition, the luminal contours were automatically detected in the OCT images by using a new minimum cost algorithm and the lumen diameter and area can be calculated and compared with the measurements from 3D QCA. In this example, the target vessel in the LAD has a minimum lumen diameter and area of 0.91 mm and 0.85 mm^2 from 3D QCA, while the OCT measurements at the same position are 0.95 mm and 0.99 mm^2, respectively.

8.4 VALIDATIONS

8.4.1 Phantoms validation

The accuracy of the registration was evaluated by acquiring a series of 12 different silicone phantoms (Via Biomedical, CA, USA) with coronary stents (Cypher Select+, Cordis, Johnson & Johnson, Miami Lakes, Fla., USA) placed by the culotte two-stent technique. Main branch intracoronary acquisitions were used for the registration with the 3D angiographic reconstruction. Stent borders were used as markers for the validation. While the proximal border was set as the baseline position for the distance mapping, the distal border was used to evaluate the registration error. The registration error was defined by the following protocol: Move a marker that was superimposed in the IVUS/OCT L-View to the position to be evaluated (in this case, the distal stent border); Move a second marker that was superimposed in the IVUS/OCT L-View to the position that corresponds to the same position to be evaluated in the angiographic views; The signed distance from the first to the second marker in the L-View was defined as the registration error.

For each phantom, the angiographic acquisitions were performed at two projections 60 degrees apart by a monoplane X-ray system (AXIOM-Artis, Siemens, Germany). The phantoms were filled with iodinated contrast media (Visipaque 270, GE Healthcare, WI, USA) during the acquisitions. Angiographic images were recorded at 25 frames/sec at a resolution of 512×512 pixels. To obtain IVUS images, the phantoms were immersed in water and acquisitions were performed at a constant pullback speed of 0.5 mm/s by using a 20 MHz transducer with a dedicated workstation (EagleEye Gold and s5, Volcano Corporation, Rancho Cordova, CA, USA) for 6 phantoms and a 40 MHz transducer with a dedicated workstation (Atlantis SR Pro and iLab, Boston Scientific, Boston, MA, USA) for the other 6 phantoms. IVUS images were recorded at 30 frames/sec and converted to DICOM format at a resolution of 512×512 pixels. To obtain OCT images, Fourier domain-OCT pullbacks were performed at 20 mm/sec by non-occlusive flushing technique using Visipaque 270 iodinated contrast media, and an OCT imaging catheter with a dedicated workstation (C7 Dragonfly and C7-XR, Lightlab Imaging, Westford, MA, USA). OCT images were recorded at 100 frames/sec and converted to DICOM format at a resolution of 1024×1024 pixels. Z-offset calibration was performed before converting to DICOM format for the subsequent analysis.

8.4.2 In-vivo validation

At the Department of Cardiology, Nanfang Hospital affiliated to the Southern Medical University in Guangzhou, China, 24 patients who underwent both angiographic and IVUS examinations of the left anterior descending artery (LAD) were retrospectively selected for the validation. Inclusion criteria were: 1) patients had no prior history of coronary artery bypass surgery; 2) motorized pullback was used during the IVUS image acquisition; 3) angiographic images were recorded by digital flat-panel X-ray acquisition systems.

Angiographic images were recorded at 25 frames/sec by a monoplane X-ray system (AXIOM-Artis, Siemens, Germany) at a resolution of 512×512 pixels. IVUS pullbacks were performed by using a motorized transducer pullback system (0.5 mm/s) with a rotating 40 MHz transducer catheter and 2.6 F imaging sheath (Boston Scientific, Boston, MA, USA). The sheath prevents direct contact of the imaging core with the vessel wall and increases the stability of the pullback procedure. All parameters required by the 3D angiographic reconstruction and the co-registration were stored in DICOM files.

Reliable anatomical landmarks in the LAD, e.g., ostia of diagonal or septal branches, were identified from both angiographic and IVUS images and used as reference markers for the validation study. When IVUS pullbacks covered the left main bifurcation and the ostium of the left circumflex artery (LCX) was well visualized in angiographic images (no significant overlap with the proximal LAD), the left main bifurcation point (carina) was included as a reference marker. The LAD (including the left main if applicable) was reconstructed from two angiographic views and registered with IVUS pullback series by the distance mapping algorithm. While the most proximal reference marker was set as the baseline position for the distance mapping, the subsequent markers were used to evaluate the registration error. The registration error was defined using the same protocol as used in the phantom validation. The correlation between the registration error and the distance from the evaluated marker to the baseline position was analyzed.

8.5 Statistics

Quantitative data are presented as mean ± standard deviation and the correlations were assessed by using Pearson's correlation coefficient. A 2-sided p-value of <0.05 was considered to be significant. All statistical analyses were carried out by using a statistical software package (SPSS, version 16.0; SPSS Inc; Chicago, IL, USA).

8.6 Results

8.6.1 Phantoms

The lengths of the 12 stents in the main branches ranged from 12.00 mm to 32.00 mm, with an average value of 22.92 ± 7.26 mm. The XA-IVUS registration error for the 12 IVUS pullbacks ranged from -0.33 mm to 0.57 mm, with an average value of 0.03 ± 0.32 mm (p = 0.75). For the OCT data, one pullback series was excluded from the study, since the pullback did not cover the distal stent border. The XA-OCT registration error for the remaining 11 OCT pullbacks ranged from -0.20 mm to 0.40 mm, with an average value of 0.05 ± 0.25 mm (p = 0.49).

8.6.2 In-vivo

From the 24 patients selected for the study, 2 patients were excluded due to insufficient image quality for the 3D angiographic reconstruction and the subsequent analysis. The baseline characteristics for the remaining 22 patients are summarized in Table I. A total of 78 reliable reference markers were identified from both angiographic and IVUS images. While the 22 most proximal markers were used as baseline positions for the distance mapping algorithm, the registration error was evaluated on the remaining 56 markers. The registration error ranges from -1.33 mm to 1.13 mm, with an average value of 0.03 ± 0.45 mm (p = 0.67). A scatter plot of the registration error is presented by Figure 8-4. The error is not correlated to the distance between the evaluated marker and the baseline position (p = 0.73).

TABLE I. Baseline Characteristics

Age (years)	60.5 ± 13.2
Gender (male, female)	17/5
1–vessel disease	13 (59%)
2–vessel disease	7 (32%)
3–vessel disease	2 (9%)
Target coronary artery (*n*)	
Left anterior descending	23
Diagonal branches	2
Left circumflex	5
Right coronary artery	3
Location (*n*)	
Proximal	12
Mid	12
Distal	9
Percent diameter obstruction (%)	48.66 ± 17.82

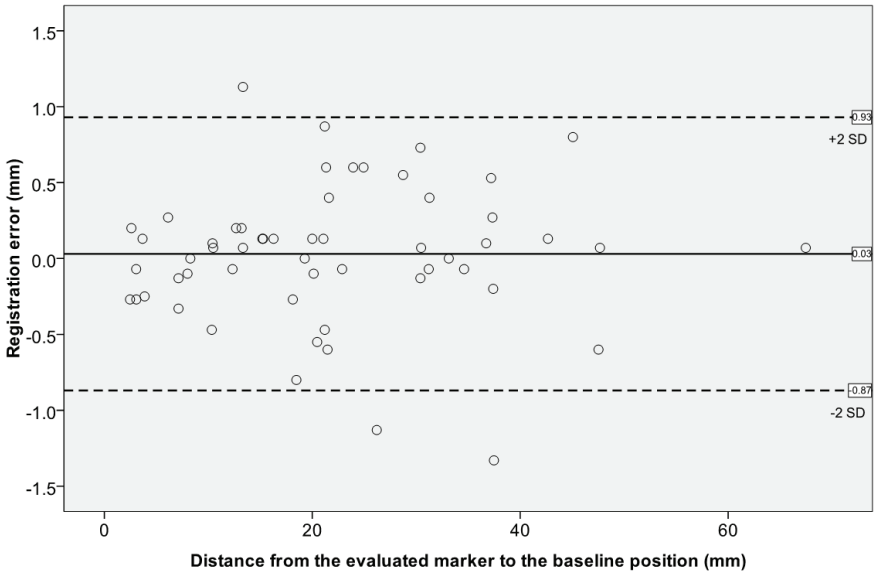

Figure 8-4 The registration error for the XA-IVUS co-registration

8.7 Discussions

The drug-eluting stents have proven to be able to reduce in-stent restenosis after coronary interventions [22-24]; however, the efficacy depends on the ability of the interventionalist to choose the optimal course of treatments and to implement the chosen course of action properly. Geographic mismatch due to suboptimal stent selection and positioning could significantly impact the short and long term outcomes of stenting procedures [25,26]. Sophisticated imaging and quantification tools are therefore demanded to guide the interventionalist to assess the true vessel dimensions, lesion location, and plaque extent for the optimization of stenting procedures.

Quantitative coronary angiography was first developed to quantify vessel motion and the effects of pharmacological agents on the regression and progression of coronary artery disease [27]. It has developed substantially over the past decades and has been applied worldwide for research and clinical purposes, in both off-line and on-line situations [2]. Recently developed 3D QCA systems based on routine angiographic projections have emerged as a new tool for the on-line guiding of coronary interventions. By resolving some of the well-known limitations in standard 2D analysis, e.g., vessel foreshortening and out-of-plane magnification [28], 3D QCA could provide more reliable assessments of segment length and diameter. In addition, the 3D angiographic reconstruction enables the subsequent automated determination of optimal viewing angles [8], which is considered useful in the stent

deployment and positioning, especially for bifurcation stenting. Due to the overlap of coronary branches, the evaluation of bifurcation lesions from series of 2D projection images could be quite challenging. An example of the optimal bifurcation viewing angle is given by Figure 8-5: (a) and (b) show the 2D angiographic projection and the 3D reconstructed bifurcation under 31 RAO, 33 Cranial, respectively. It is very clear from the 3D view that the visualization of the ostium of the diagonal branch under 31 RAO, 33 Cranial is not optimal. Deploying a stent to the ostium of the diagonal branch by using this viewing angle might result in undesirable results, e.g., stent protrusion into the LAD or incomplete stent coverage at the ostium. Figure 8-5 (c) shows the 3D bifurcation under the optimal viewing angle of 40 LAO, 56 Cranial. The visualization of the ostium of the diagonal branch has been significantly improved.

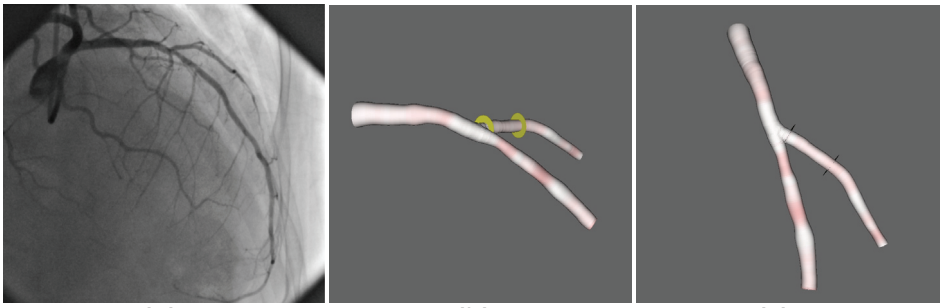

(a) (b) (c)

Figure 8-5. The visualization of a bifurcation under different views: (a) is the angiographic view under 31 RAO, 33 Cranial; (b) is the 3D reconstructed bifurcation under 31 RAO, 33 Cranial; (c) is the 3D reconstructed bifurcation under the optimal viewing angle of 40 LAO, 56 Cranial.

Thanks to the capacity and high resolution, IVUS and OCT have greatly improved our understanding of coronary atherosclerosis and the tissue responses after stent implantation. The role of IVUS/OCT in assessing plaque extent and distribution for optimal treatment planning has been well acknowledged. However, the ability to implement the course of planning has been limited by the difficulty in corresponding IVUS/OCT with XA images. For stenting procedures, accurate positioning of the stent is important to ensure complete lesion coverage and to prevent the undesirable responds to the stent expansion, e.g., when diffused lesions is heavily calcified at the lesion border. The current workflow by mentally mapping the landing zones from IVUS/OCT to XA could be quite challenging when no landmark is available in the neighborhood of the lesion. In other cases when the diseased vessel has multiple sidebranches, e.g., the LAD with many septal and diagonal branches, the mental mapping could be confused or even become completely mismatched due to the fact that not all sidebranches are well presented in the IVUS/OCT L-View. In such cases, the XA-IVUS/OCT co-registration could establish a point-to-point correspondence between XA

and IVUS/OCT images. As a result, the deployment of the stent to the targeted position is simplified.

Despite of its attractive clinical perspectives, the integration of XA and IVUS/OCT in the current setting of catheterization laboratories has been hampered by the fact that the major angiography vendors do not have IVUS/OCT in their portfolio. The data connectivity is a significant bottleneck for such integration to be used in on-line mode. It is desirable that the angiography and IVUS/OCT vendors will cooperate to make the integration clinically acceptable with a seamless workflow in the near future.

The XA-IVUS/OCT co-registration serves the primary but yet the most important step for the complete fusion of 3D QCA and IVUS/OCT, which could be used to correct for the error in assessing plaque volume introduced by vessel tortuosity [19]. In addition, in case of oblique imaging [29, 30] when the IVUS/OCT transducer catheter is not aligned parallel to the vessel centerline, the fusion of these two imaging modalities can minimize the overestimation of cross-sectional dimensions from IVUS/OCT images, especially for the curved vessel segments with large diameters. However, such clinical benefits still have to be established.

8.8 Limitations

The IVUS/OCT pullback procedures were not ECG-gated, therefore, the cardiac motion could have influenced the axial position of each IVUS/OCT cross-sectional image. However, by interpreting the pullback series in a couple of longitudinal views, it is possible to visually identify the cross-sections that were significantly influenced by the cardiac motion and, to avoid using those positions as markers for the co-registration. Besides, the ECG-gated pullback procedures are not practical to be included in routine clinical practice for being expensive and for prolonging the acquisition time [31].The faster pullback speed and higher frame rate acquisition achieved by the Fourier-domain OCT systems could further decrease the impact of the motion-induced artifacts [29].

The in-vivo validation is limited by the sample size and the usage of only one IVUS transducer pullback system. Early literatures have shown that the accuracy of in-vivo length measurements using different pullback systems could be different [32], therefore, the co-registration could be impacted. Extensive validations for the co-registration by using different transducer pullback systems are under investigation.

8.9 Conclusions

The new XA-IVUS/OCT registration approach is a straightforward and reliable solution for the integration/combination of X-ray angiographic and

IVUS/OCT imaging. It provides the interventionalist with detailed information about vessel size and plaque composition at every position along the vessel of interest, making this a suitable tool during the actual intervention.

8.10 References

1. Reiber JHC, Serruys PW, Kooijman CJ, et al. Assessment of short-, medium-, and long-term variations in arterial dimensions from computer-assisted quantitation of coronary cineangiograms. Circulation 1985; 71:280–288.
2. Reiber JHC, Tuinenburg JC, Koning G, et al. Quantitative coronary arteriography. In: Coronary Radiology 2nd Revised Edition, Oudkerk M, Reiser MF (Eds.), Series: Medical Radiology, Sub series: Diagnostic Imaging, Baert AL, Knauth M, Sartor K (Eds.). Springer-Verlag, Berlin-Heidelberg, 2009:41-65.
3. Goktekin O, Kaplan S, Dimopoulos K, et al. A New Quantitative Analysis System for the Evaluation of Coronary Bifurcation Lesions: Comparison with Current Conventional Methods. Catheter Cardiovasc Interv 2007; 69:172–180.
4. Rittger H, Schertel B, Schmidt M, et al. Three-dimensional reconstruction allows accurate quantification and length measurements of coronary artery stenoses. EuroIntervention 2009; 5:127–132.
5. Tu S, Huang Z. Koning G, et al. A novel three-dimensional quantitative coronary angiography system: In-vivo comparison with intravascular ultrasound for assessing arterial segment length. Catheter Cardiovasc Interv 2010; 76:291–298.
6. Bruining N, Tanimoto S, Otsuka M, et al. Quantitative multi-modality imaging analysis of a bioabsorbable poly-L-lactid acid stent design in the acute phase: a comparison between 2 and 3D-QCA, QCU and QMSCT-CA. EuroIntervention 2008; 4:285–291.
7. Schuurbiers JC, Lopez NG, Ligthart J, et al. In vivo validation of CAAS QCA-3D coronary reconstruction using fusion of angiography and intravascular ultrasound (ANGUS). Catheter Cardiovasc Interv 2009; 73:620–626.
8. Tu S, Koning G, Jukema W, et al. Assessment of obstruction length and optimal viewing angle from biplane X-ray angiograms. Int J Cardiovasc Imaging 2010; 26:5–17.
9. Green NE, Chen SJ, Hansgen AR, et al. Angiographic Views Used for Percutaneous Coronary Interventions: A Three Dimensional Analysis of Physician-Determined vs. Computer-Generated Views. Catheter Cardiovasc Interv 2005; 64: 451–459.
10. Sadamatsu K, Sagara S, Yamawaki T, et al. Three-dimensional coronary imaging for the ostium of the left anterior descending artery. Int J Cardiovasc Imaging 2009; 25:223-228.
11. Gollapudi RR, Valencia R, Lee SS, et al. Utility of three-dimensional reconstruction of coronary angiography to guide percutaneous coronary intervention. Catheter Cardiovasc Interv 2007; 69:479–482.
12. Glagov S, Weisenberg E, Zarins CK, et al. Compensatory enlargement of human atherosclerotic coronary arteries. N Engl J Med 1987; 316:1371-1375.
13. Dumay ACM. Image Reconstruction from Biplane Angiographic Projections. Dissertation 1992, Delft University of Technology.
14. Wahle A, Wellnhofer E, Mugaragu I, et al. Assessment of Diffuse Coronary Artery Disease by Quantitative Analysis of Coronary Morphology Based upon 3-D Reconstruction from Biplane Angiograms. IEEE Trans Med Imaging 1995; 14:230–241.
15. Chen SJ, Carroll JD, Messenger JC. Quantitative Analysis of Reconstructed 3-D Coronary Arterial Tree and Intracoronary Devices. IEEE Trans Med Imaging 2002; 21:724-740.

16. Janssen JP, Koning G, De Koning PJH, et al. A new approach to contour detection in X-ray arteriograms: The wavecontour. Investigative radiology 2005; 40:514–520.
17. Reiber JHC, van der Zwet PM, Koning G, et al. Accuracy and precision of quantitative digital coronary arteriography: observer-, short-, and medium-term variabilities. Cathet Cardiovasc Diagn 1993; 28:187–198.
18. Slager CJ, Wentzel JJ, Schuurbiers JCH., et al. True 3-Dimensional Reconstruction of Coronary Arteries in Patients by Fusion of Angiography and IVUS (ANGUS) and Its Quantitative Validation. Circulation 2000; 102:511-516.
19. Wahle A, Lopez JJ, Olszewski ME, et al. Plaque development, vessel curvature, and wall shear stress in coronary arteries assessed by X-ray angiography and intravascular ultrasound. Medical Image Analysis 2006; 10:615-631.
20. Rotger D, Radeva P, Canero C, et al. Corresponding IVUS and Angiogram Image Data. Proceedings of Computers in Cardiology 2001; 28:273–276.
21. Tu S, Koning G, Tuinenburg JC, et al. Coronary angiography enhancement for visualization. Int J Cardiovasc Imaging 2009; 25:657–667.
22. Moses JW, Leon MB, Popma JJ, et al. Sirolimus-eluting stents versus standard stents in patients with stenosis in a native coronary artery. N Engl J Med 2003; 349:1315–1323.
23. Stone GW, Ellis SG, Cox DA, et al. A polymer-based, paclitaxel-eluting stent in patients with coronary artery disease. N Engl J Med 2004; 350:221–231.
24. Stone GW, Moses JW, Ellis SG, et al. Safety and efficacy of sirolimus- and paclitaxel-eluting coronary stents. N Engl J Med 2007; 356:998–1008.
25. Fujii K, Carlier SG, Mintz GS, et al. Stent underexpansion and residual reference segment stenosis are related to stent thrombosis after sirolimus-eluting stent implantation: An intravascular ultrasound study. J Am Coll Cardiol 2005; 45:995–998.
26. Costa MA, Angiolillo DJ, Tannenbaum M, et al. Impact of stent deployment procedural factors on long-term effectiveness and safety of sirolimus-eluting stents (final results of the multicenter prospective STLLR trial). Am J Cardiol 2008; 101:1704–1711.
27. Brown BG, Bolson E, Frimer M, et al. Quantitative coronary angiography : estimation of dimensions, hemodynamic resistance, and atheroma mass of coronary artery lesions using arteriography in 256 nonoperated patients. Circulation 1977; 55:329-337.
28. Koning G, Hekking E, Kemppainen JS, et al. Suitability of the Cordis StabilizerTM marker guide wire for quantitative coronary angiography calibration: An in vitro and in vivo study. Catheter Cardiovasc Interv 2001; 52:334–341.
29. Sawada T, Shite J, Negi N, et al. Factors that influence measurements and accurate evaluation of stent apposition by optical coherence tomography. Assessment using a phantom model. Circ J 2009; 73:1841-1847.
30. Geselschap JH, Heilbron MJ, Hussain FM, et al. The effect of angulation on intravascular ultrasound imaging observed in vascular phantoms. J Endovasc Surg 1998; 5:126-133.
31. Bruining N, von Birgelen C, de Feyter PJ, et al. ECG-gated versus nongated three-dimensional intracoronary untrasound analysis: implications for volumetric measurements. Cathe Cardiovasc Diagn 1998; 43:254-260.
32. Tanaka K, Carlier SG, Mintz GS, et al. The accuracy of length measurements using different intravascular ultrasound motorized transducer pullback systems. Int J Cardiovasc Imaging 2007; 23:733–738.

CHAPTER 9

In-vivo Comparison of Arterial Lumen Dimensions Assessed by Co-registered Three-dimensional (3D) Quantitative Coronary Angiography, Intravascular Ultrasound and Optical Coherence Tomography

This chapter was adapted from:

In-vivo Comparison of Arterial Lumen Dimensions Assessed by Co-registered Three-dimensional (3D) Quantitative Coronary Angiography, Intravascular Ultrasound and Optical Coherence Tomography
Shengxian Tu, Liang Xu, Jurgen Ligthart, Bo Xu, Karen Witberg, Zhongwei Sun, Gerhard Koning, Johan H. C. Reiber, Evelyn Regar

International Journal of Cardiovascular Imaging
Epub Ahead of Print

ABSTRACT

Objectives: This study sought to compare lumen dimensions as assessed by 3D quantitative coronary angiography (QCA) and by intravascular ultrasound (IVUS) or optical coherence tomography (OCT), and to assess the association of the discrepancy with vessel curvature.

Background: Coronary lumen dimensions often show discrepancies when assessed by X-ray angiography and IVUS or OCT. One source of error concerns a possible mismatch in the selection of corresponding regions for the comparison. Therefore, we developed a novel, real-time co-registration approach to guarantee the point-to-point correspondence between the X-ray, IVUS and OCT images.

Methods: A total of 74 patients with indication for cardiac catheterization were retrospectively included. Lumen morphometry was performed by 3D QCA and by IVUS or OCT. For quantitative analysis, a novel, dedicated approach for co-registration and lumen detection was employed allowing for assessment of lumen size at multiple positions along the vessel. Vessel curvature was automatically calculated from the 3D arterial vessel centerline.

Results: Comparison of 3D QCA and IVUS was performed in 519 distinct positions in 40 vessels. Correlations were r=0.761, r=0.790, and r=0.799 for short diameter (SD), long diameter (LD), and area, respectively. Lumen sizes were larger by IVUS (p<0.001): SD, 2.51±0.58mm vs 2.34±0.56mm; LD, 3.02±0.62mm vs 2.63±0.58mm; Area, 6.29±2.77 mm^2 vs 5.08±2.34mm^2. Comparison of 3D QCA and OCT was performed in 541 distinct positions in 40 vessels. Correlations were r=0.880, r=0.881, and r=0.897 for SD, LD, and area, respectively. Lumen sizes were larger by OCT (p<0.001): SD, 2.70±0.65mm vs 2.57±0.61mm; LD, 3.11±0.72mm vs 2.80±0.62mm; Area 7.01±3.28mm^2 vs 5.93±2.66mm2. The vessel-based discrepancy between 3D QCA and IVUS or OCT long diameters increased with increasing vessel curvature.

Conclusions: Our comparison of co-registered 3D QCA and invasive imaging data suggests a bias towards larger lumen dimensions by IVUS and by OCT, which was more pronounced in larger and tortuous vessels.

9.1 Introduction

Coronary lumen dimensions often show discrepancies when assessed by X-ray angiography and invasive imaging such as intravascular ultrasound (IVUS) or optical coherence tomography (OCT) [1]. One source of error consists of a possible mismatch in the selection of corresponding regions for the comparison of different imaging modalities. Therefore, we developed a novel, real-time co-registration approach to guarantee the point-to-point correspondence between the X-ray, IVUS and OCT images. This study compared lumen size as assessed in-vivo by co-registered three-dimensional quantitative coronary angiography (3D QCA) and IVUS or OCT in both frame-based and vessel-based approaches. In addition, we hypothesized that the vessel-based discrepancy between 3D QCA and IVUS or OCT was associated with vessel curvature, a surrogate for vessel tortuosity, since tortuous vessels might change the alignment of the intracoronary imaging catheter inside the lumen, resulting in inaccurate lumen dimensions when the catheter was positioned obliquely (not parallel to the vessel long-axis direction). Therefore, vessel curvature was also assessed in this study and its association with the discrepancy between 3D QCA and IVUS/OCT was assessed. The looseness of the catheter, i.e., the space between the lumen-intima interface and the imaging catheter was used as a confounder to analyze the aforementioned association. The more space between the catheter and the lumen-intima interface, the more oblique the catheter could be positioned in tortuous vessels, possibly leading to more overestimation of lumen size by IVUS/OCT at certain regions. As a result, the discrepancy between 3D QCA and IVUS/OCT might increase. On the other hand, less catheter looseness creates less chance of oblique imaging. A catheter looseness of zero indicates that the imaging catheter fits tightly in the vessel. In such a case, IVUS/OCT images represent at every location the cross-section perpendicular to the vessel long-axis direction. The impact of vessel curvature on the discrepancy between 3D QCA and IVUS/OCT is then minimal or actually absent.

9.2 Methods

9.2.1 Study population

At the Catheterization Lab, National Center for Cardiovascular Diseases of China and Fu Wai Hospital in Beijing, China, and the Department of Cardiology, ErasmusMC in Rotterdam, the Netherlands, a total of 74 patients with indication for cardiac catheterization were retrospectively included in this study. Inclusion criteria were: 1) X-ray angiographic images were acquired by digital image intensifiers (flat-panel

systems). 2) Two angiographic projections at least 25 degrees apart with lumen well filled with contrast dye agent were recorded. 3) The vessel of interest was imaged with motorized IVUS or OCT pullbacks at constant pullback speeds. 4) The vessel of interest was not totally occluded and had no history of coronary bypass surgery. 5) If stents were present in the vessel of interest, the entire IVUS/OCT pullback series completely imaged another non-stented lesion.

Angiographic images were recorded by different X-ray systems (AXIOM-Artis, Siemens, Erlangen, Germany; AlluraXper, Philips, Best, the Netherlands; and Safair, Shimadzu, Kyoto, Japan). The angiographic images used for 3D QCA were acquired prior to inserting the guidewire and intracoronary imaging catheter. Grayscale IVUS imaging was carried out using a 40 MHz transducer and a 2.9 F imaging sheath with a dedicated workstation (Atlantis SR Pro and Galaxy, Boston Scientific, Boston, MA, USA). Images were recorded at 30 frames/s and converted to DICOM (Digital imaging and communications in medicine) format at a resolution of 512×512 pixels. OCT pullbacks were performed at 20 mm/s by non-occlusive flushing technique using a 2.7 F imaging catheter with a dedicated workstation (C7 Dragonfly and C7-XR, Lightlab Imaging, Westford, MA, USA). OCT images were recorded at 100 frames/s and converted to DICOM format at a resolution of 512×512 pixels. Z-offset calibration was performed before converting to DICOM format for the subsequent analysis.

9.2.2 Three-dimensional quantitative coronary angiography

3D angiographic reconstruction and quantitative analysis were performed by an experienced analyst using a novel and validated 3D QCA software package (prototype version, Medis medical imaging systems bv, Leiden, the Netherlands) [2-4]. The following steps were used as standard operation procedures in the study: 1) two image sequences acquired at two arbitrary angiographic views with projection angles at least 25 degrees apart were loaded; 2) automated calibration or manual catheter calibration if the so-called Pixel Spacing parameter was not recorded by the X-ray systems was performed; 3) properly contrast-filled end-diastolic (ED) frames of these angiographic image sequences were selected; 4) one to three anatomical markers, e.g., bifurcations, were identified as reference points in the two angiographic views for the automated correction of angiographic system distortions [5]; 5) the vessel segment of interest was defined and automated 2D lumen edge detection was performed using our extensively validated QCA algorithms [6-7]; 6) automated 3D reconstruction and modeling techniques were performed. The resulting lumen surface modeled with elliptical cross-sections and the

so-called reference surface modeled with circular cross-sections were generated. Quantitative data including the global parameters, e.g., lumen volume, diameter and area stenoses, and the local parameters at every position along the vessel segment of interest, e.g, short diameter, long diameter, and area were automatically reported.

An example of 3D angiographic reconstruction of the Left Circumflex Artery (LCx) is given in Figure 9-1. The two angiographic views acquired at 56 LAO, 19 Caudal and 13 RAO, 23 Caudal were used for the 3D reconstruction. The left top panels (Figure 9-1A and 9-1B) show the segment of interest in the LCx and its extracted 2D contours, superimposed on the two angiographic views. The left bottom panel (Figure 9-1C) shows the 3D reconstructed lumen surface in a color-coded fashion. In this case, the lesion at the proximal LCx had a minimum lumen diameter of 1.11 mm. The diameter and area stenoses were found to be 68.1% and 82.7%, respectively.

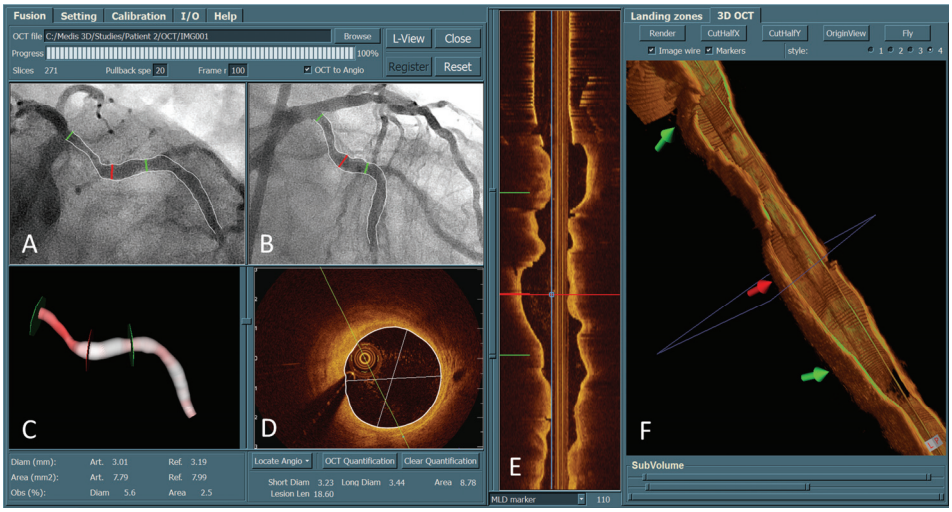

Figure 9-1. Three-dimensional coronary angiographic reconstruction and its registration with 3D OCT. After the registration, the corresponding markers in different views (A, B, C, E, and F) were synchronized, allowing the assessment of lumen dimensions from both imaging modalities at every corresponding position along the vessel segment.

9.2.3 Calculation of vessel curvature

Intuitively, vessel curvature is the amount by which the vessel deviates from being a straight tube. Tortuous or bended vessels have higher curvature than straight vessels. At every position along the tortuous vessel, there is a unique circle which best approximates the vessel segment. The radius of that circle is equal to the reciprocal of the curvature. To determine the curvature at each position along the vessel of

interest, the reconstructed arterial centerline was approximated by a parameterized Bezier curve, which is frequently used in modeling smooth curves/surfaces in computer graphics and related fields. In such a way the derivatives of the vessel were estimated by the Bezier curve and the curvature was calculated using the first and second derivatives. Figure 9-2 shows the curvature profile for the LCx segment reconstructed in Figure 9-1. The carina position of the LCx/OM (Obtuse Marginal) bifurcation has the highest curvature of 0.1082 mm^{-1}. The vessel curvature was defined as the average curvature for all the positions along the vessel of interest. In this case, the vessel curvature is 0.0615 mm^{-1} for the reconstructed segment.

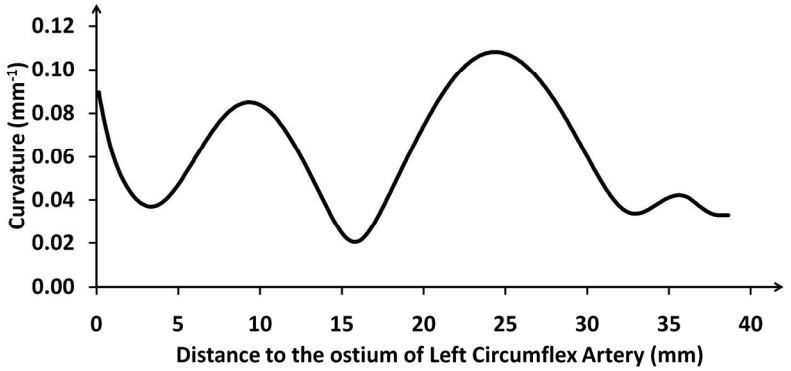

Figure 9-2. The curvature profile assessed from the 3D reconstructed Left Circumflex Artery. The average curvature is 0.0615 mm^{-1} for the reconstructed segment.

9.2.4 Registration of 3D QCA with IVUS or OCT

Over the past years we have developed and validated a real-time and straightforward approach for the on-line registration of 3D QCA with IVUS/OCT [8]. The approach only requires the reconstruction of arterial centerlines from two angiographic images (which is a standard module in 3D QCA software packages). The step of reconstructing the IVUS/OCT pullback trajectory as required by conventional approaches was replaced by a novel distance mapping algorithm which estimated the corresponding IVUS/OCT cross-sectional image for each position along the reconstructed arterial centerline, based on the accumulated curvature and lumen size as assessed from 3D QCA. By this approach, the disadvantage of using diluted contrast agent during angiographic image acquisitions, as required by conventional registration approaches [9-10] in order to simultaneously visualize the lumen and the imaging catheter, was resolved and as a result, the quality of 3D QCA was improved and less manual corrections were required in the lumen edge detection. Minimum user interactions were achieved in this registration approach by indicating only one

anatomical or mechanical landmark that was visualized in both X-ray and IVUS/OCT images, e.g., the carina of a bifurcation. After the registration, point-to-point correspondence between the X-ray and IVUS/OCT images was established and markers superimposed on different image views were synchronized. Figure 9-1 shows three positions with corresponding markers superimposed in the 2D and 3D angiographic views (A, B, and C) as well as the 3D OCT and longitudinal views (F and E).

The registration for all the vessels was performed by an experienced analyst and the results were verified by an expert in intracoronary imaging using landmarks available along the vessel of interest. In such a way the reliability of the registration was guaranteed.

9.2.5 Frame selection and quantitative IVUS/OCT analysis

A number of spatial positions including normal and obstructed cross-sections along the vessel of interest were selected for the quantitative analysis. A constant stepping interval depending on the length of the vessel of interest was initially applied in the selection procedure to guarantee that a couple of positions (at least 8) were selected for each vessel. If thrombosis, plaque erosion or dissection was identified in the selected frames, or if the corresponding vessel positions in the angiographic images had severe overlap that could jeopardize the reliability of the lumen contour delineation in QCA, the adjacent frames were selected. If predilation or thrombectomy was performed before intracoronary imaging, the injured sub-segments were excluded. Bifurcations were excluded as well since there was no well-established standard to compare bifurcation dimensions between 3D QCA and IVUS or OCT. In such a way a couple of reliably co-registered positions were analyzed for each vessel and the variability introduced by the analysis methodology itself was reduced. As a result, the comparisons reflected the systematic difference between 3D QCA and IVUS or OCT. For IVUS images, only frames that corresponded to the ED phase in the cardiac cycle were considered, since 3D QCA was also performed at the ED phase. A well validated algorithm integrated in a commercial software package (QIvus 2.1, Medis medical imaging systems bv, Leiden, the Netherlands) [11] was used for the IVUS segmentation and quantitative analysis. For quantitative OCT analysis, a new mincost algorithm was directly integrated in the registration software to automatically detect the lumen-intima interface from OCT images. The algorithm used the asymmetric sticks [12] to construct a matrix with each cell representing the edge strength/probability for the corresponding position. In a next step, a global optimization algorithm, the so-called mincost algorithm, was applied to find the optimal path (lumen-intima interface) with the

strongest edge strength. An example of comparing lumen dimensions as assessed from 3D QCA and OCT is given by Figure 9-1. In this case, short diameter, long diameter, and lumen area at the position indicated by the middle (red) marker were 3.23 mm, 3.44 mm, and 8.78 mm^2 by OCT, as compared with 3.01 mm, 3.30, and 7.79 mm^2 by 3D QCA.

Frame-based comparison between 3D QCA and IVUS or OCT was performed on all the selected positions. The mean lumen size calculated from all the selected positions for each vessel was used to represent the lumen size for that specific vessel and used for the vessel-based comparison. To assess the association of the discrepancy between 3D QCA and IVUS or OCT with vessel curvature, the confounder, i.e., the looseness of the IVUS/OCT imaging catheter, was derived, defined by the long lumen diameter minus the catheter diameter. Accordingly, larger lumen diameter yielded larger catheter looseness. Since lumen diameters were unknown in this study, the average value of the 3D QCA and IVUS/OCT long diameters was used to calculate the catheter looseness.

Quantitative IVUS/OCT analysis was performed on the selected corresponding positions by an analyst, who was unaware of the 3D QCA results. The measurements in the first 10 vessels were repeated by the same analyst one month later, and by a second analyst, both blinded to the earlier results. From these measurements, intra- and inter-observer variabilities were derived.

9.3 Statistics

3D QCA was compared with IVUS or OCT by using paired *t*-test, while the differences were evaluated by Bland-Altman plots. Quantitative data were presented as mean difference ± standard deviation and the correlations were assessed by using Pearson's correlation coefficient, providing the correlation coefficient (*R*) and the regression line. A 2-sided *p*-value of <0.05 was considered to be significant. Confounders independently influencing the vessel-based discrepancy between 3D QCA and IVUS or OCT were analyzed using a stepwise multiple linear regression. The intra- and interobserver variabilities were reported as mean difference ± standard deviation. All statistical analyses were carried out using SPSS software (PASW version 18.0.0, 2009; SPSS Inc, Chicago, IL).

9.4 Results

The baseline characteristics for the included patients and assessed vessels are given in Table 1. A total of 40 vessels (LAD = 35, LCx = 5, Diagonal = 1, RCA = 1) from 37 patients were included to compare lumen size by 3D QCA and by IVUS. In 4 of these vessels, manual calibration had

Table1. Baseline Characteristics

	IVUS	OCT
Patient	n = 37	n = 37
Age	55.8 (41-75)	60 (44-78)
Male/Female	26/11	21/16
Imaged vessel:	n = 40	n = 40
LAD/Diagonal/LCx/OM/RCA/RI	35/1/5/1/0/0	22/0/5/1/11/1
Stents in subsegment	19	1
Assessed lesion:		
Predilatated before intracoronary imaging	6	3
Ostial or bifurcation lesion	23	13
Diffused lesion	18	11
Calcified lesion	13	23
Diameter stenosis*	45.5(±12.5)%	45.4(±17.0)%
Lesion treated later by revascularization	24	25

*Assessments based on 3D QCA. LAD = Left Anterior Descending; LCx = Left Circumflex Artery; OM = Obtuse Marginal; RCA = Right Coronary Artery; RI = Ramus Intermedius.

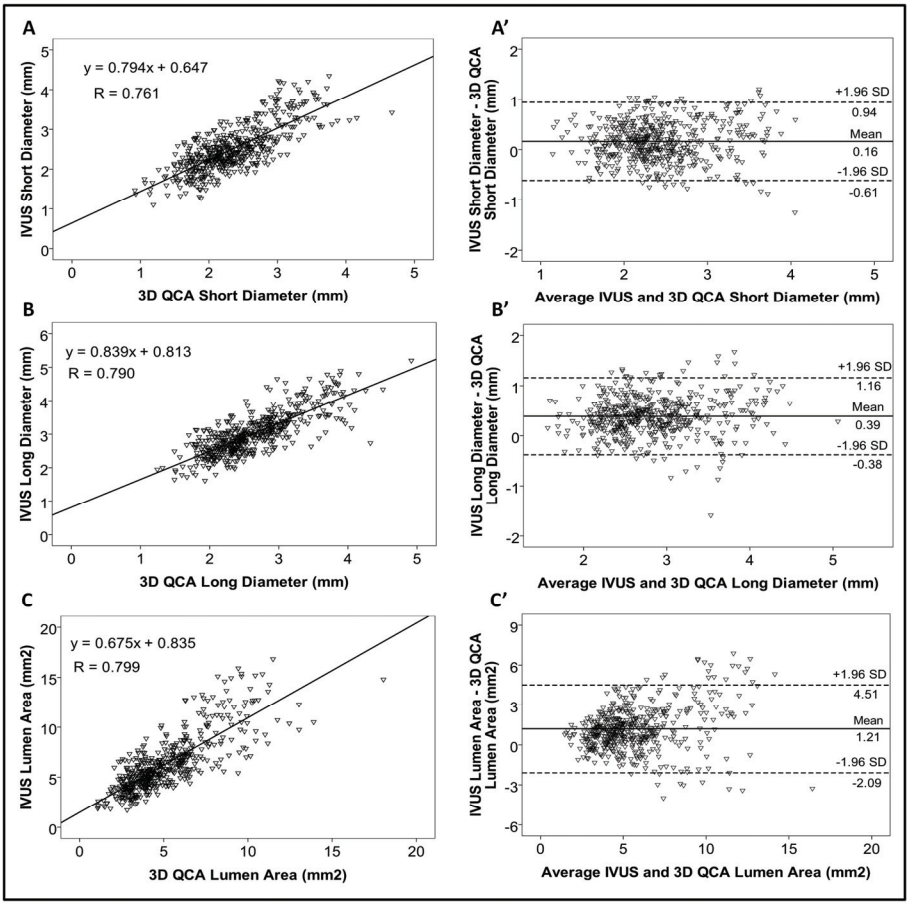

Figure 9-3. Frame-based comparison between 3D QCA and IVUS. Correlations in assessing short diameter (A), long diameter (B), and area (C). Bland-Altman plots show the differences of the measurements in short diameter (A'), long diameter (B'), and area (C'). There is an increasing bias towards larger discrepancy in long diameter and area at larger vessels. n = 519 in 40 vessels.

to be performed in the 3D angiographic reconstruction. For the remaining 36 vessels, automated calibration was applied. The segment of interest had a mean diameter stenosis of 45.5% as assessed from 3D QCA. 24 vessels were revascularized after the examinations. A total of 40 vessels (LAD = 22, LCx = 5, OM = 1, RCA = 11, Ramus Intermedius = 1) from the other 37 patients were included to compare 3D QCA and OCT. Automated calibration was applied for all the vessels in the 3D angiographic reconstruction. The assessed segments of interest had a mean diameter stenosis of 45.4% as assessed from 3D QCA. 25 vessels were revascularized after the examinations.

A total of 519 distinct positions were selected for the comparison between 3D QCA and IVUS in measuring short diameter (SD), long diameter (LD) and lumen area. Scatter plots of the comparison are presented in Figure 9-3. There were good correlations between 3D QCA and IVUS: SD (r=0.761, p<0.001); LD (r=0.790, p<0.001); Area (r=0.799, p<0.001). Bland-Altman plots in Figure 9-3B' and 9-3C' show that there was an increasing bias towards larger lumen size by IVUS, which was more pronounced in larger vessels. Quantitative data are presented in Table 2. Lumen sizes were larger by IVUS than by 3D QCA: SD 2.51±0.58 mm vs 2.34±0.56 mm (p<0.001); LD 3.02±0.62 mm vs 2.63±0.58 mm (p<0.001); Area 6.29±2.77 mm^2 vs 5.08±2.34 mm^2 (p<0.001) in frame-based analysis. The difference was 0.16 mm (6.6%) in SD, 0.39 mm (13.8%) in LD, and 1.21 mm2 (21.3%) in area. Vessel-based analysis showed similar discrepancies: SD 2.53±0.39 mm vs 2.35±0.37 mm (p<0.001); LD 3.05±0.43 mm vs 2.64±0.36 mm (p<0.001); Area 6.41±1.92 mm^2 vs 5.12±1.45 mm^2 (p<0.001).

Table 2. Comparison between 3D QCA and IVUS in Assessing Lumen Size

	IVUS	3D QCA	Difference (95% CI)	Intra-observer variability*	Inter-observer variability*
Positions, n = 519					
Short diameter (mm)	2.51±0.58	2.34±0.56	0.16 (0.13-0.20) †	0.022±0.131	0.025±0.097
Long diameter (mm)	3.02±0.62	2.63±0.58	0.39 (0.36-0.42) †	0.039±0.162	0.042±0.092
Lumen area (mm^2)	6.29±2.77	5.08±2.34	1.21 (1.07-1.35) †	0.124±0.534	0.134±0.356
Vessels, n = 40					
Short diameter (mm)	2.53±0.39	2.35±0.37	0.18 (0.10-0.26) †	-	-
Long diameter (mm)	3.05±0.43	2.64±0.36	0.41 (0.34-0.48) †	-	-
Lumen area (mm^2)	6.41±1.92	5.12±1.45	1.29 (0.95-1.63) †	-	-

*Observer variability was calculated from 136 positions from the first 10 vessels. CI = confidence interval; †p < 0.001.

A total of 541 distinct positions were selected for the comparison between 3D QCA and OCT. Scatter plots of the comparison are presented in Figure 9-4. Good correlations were found between 3D QCA and OCT:

SD (r=0.880, p<0.001); LD (r=0.881, p<0.001); Area (r = 0.897, p<0.001). Bland-Altman plots in Figure 9-4B' and 9-4C' show that there was an increasing bias towards larger lumen size by OCT, which was more pronounced in larger vessels. Quantitative data are presented in Table 3. Lumen sizes were larger by OCT than by 3D QCA: SD 2.70±0.65mm vs 2.57±0.61mm (p<0.001); LD 3.11±0.72mm vs 2.80±0.62mm (p<0.001); Area 7.01±3.28mm^2 vs 5.93±2.66mm^2 (p<0.001) in frame-based analysis. The difference was 0.14 mm (5.3%) in SD, 0.30 mm (10.2%) in LD, and 1.07 mm2 (16.5%) in area. Vessel-based analysis showed similar discrepancies: SD 2.71±0.46 mm vs 2.57±0.43 mm (p<0.001); LD 3.11±0.52 mm vs 2.81±0.45 mm (p<0.001); Area 7.02±2.34 mm^2 vs 5.94±1.91 mm^2 (p<0.001).

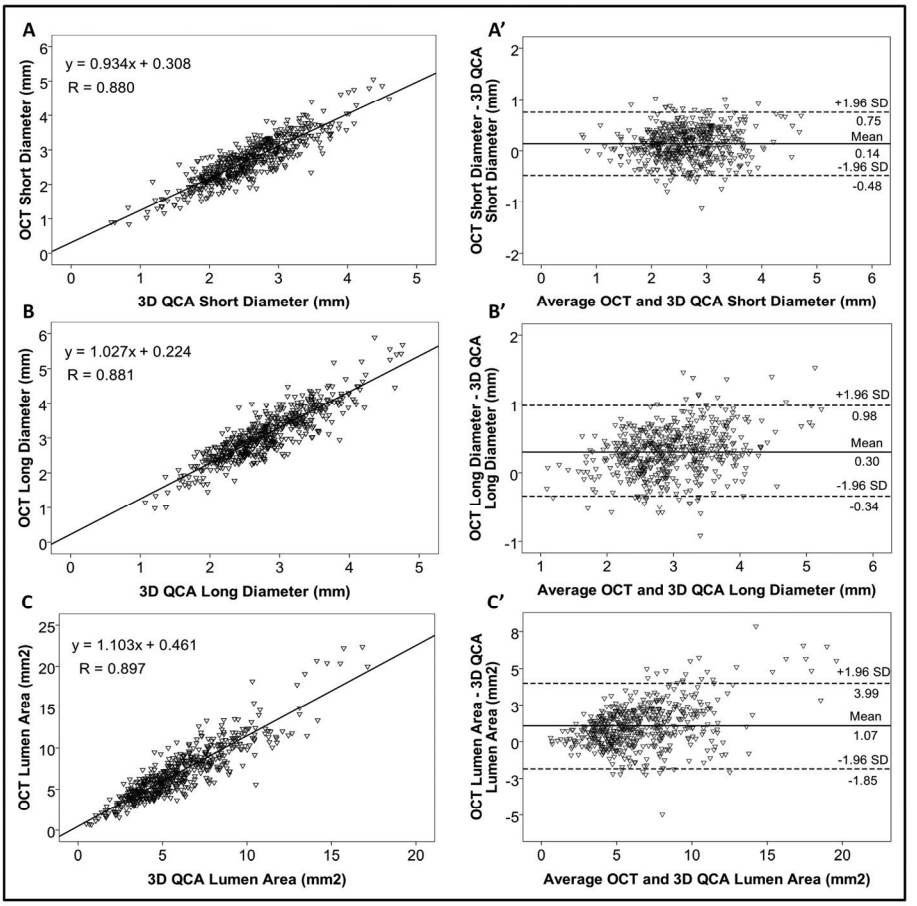

Figure 9-4. Frame-based comparison between 3D QCA and OCT. Correlations in assessing short diameter (A), long diameter (B), and area (C). Bland-Altman plots show the differences of the measurements in short diameter (A'), long diameter (B'), and area (C'). There is an increasing bias towards larger discrepancy in long diameter and area at larger vessels. n = 541 in 40 vessels.

Table 3. Comparison between 3D QCA and OCT in Assessing Lumen Size

	OCT	3D QCA	Difference (95% CI)	Intra-observer variability*	Inter-observer variability*
Positions, n = 541					
Short diameter (mm)	2.70±0.65	2.57±0.61	0.14 (0.11-0.16) †	0.000±0.013	0.003±0.029
Long diameter (mm)	3.11±0.72	2.80±0.62	0.30 (0.27-0.33) †	0.003±0.024	0.006±0.035
Lumen area (mm^2)	7.01±3.28	5.93±2.66	1.07 (0.95-1.20) †	0.002±0.039	0.021±0.059
Vessels, n = 40					
Short diameter (mm)	2.71±0.46	2.57±0.43	0.14 (0.09-0.19) †	-	-
Long diameter (mm)	3.11±0.52	2.81±0.45	0.30 (0.24-0.37) †	-	-
Lumen area (mm^2)	7.02±2.34	5.94±1.91	1.08 (0.80-1.37) †	-	-

*Observer variability was calculated from 165 positions from the first 10 vessels. CI = confidence interval; †$p < 0.001$.

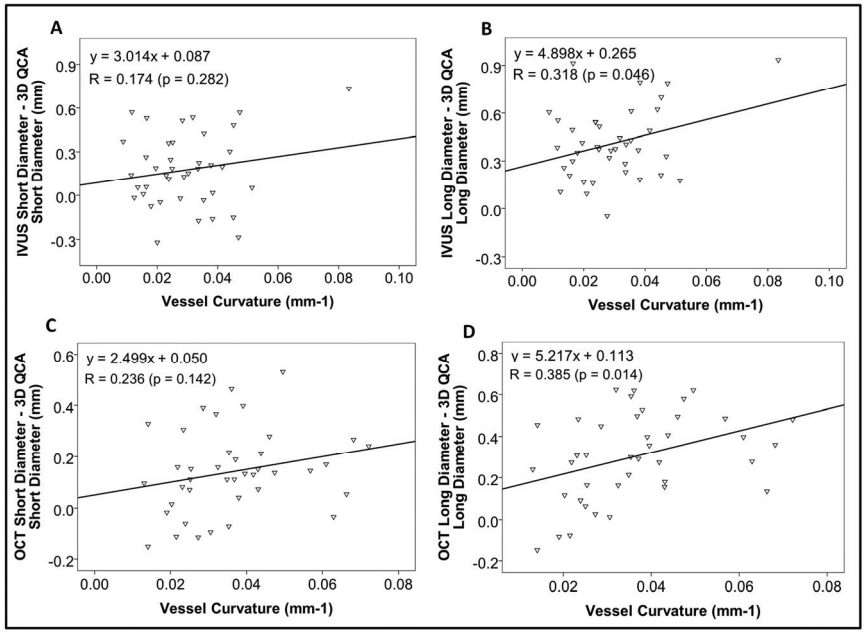

Figure 9-5. Vessel-based comparison between 3D QCA and IVUS/OCT. Correlations between 3D QCA and IVUS for short diameter (A) and long diameter (B). There is an increasing bias towards larger discrepancy in long diameter at higher vessel curvature. Correlations between 3D QCA and OCT for short diameter (C) and long diameter (D). There is also an increasing bias towards larger discrepancy in long diameter at higher vessel curvature. n = 40 vessels in 37 patients.

Figure 9-5 shows the vessel-based discrepancy between 3D QCA and IVUS/OCT with respect to the vessel curvature. There was a bias towards larger discrepancy in vessels with higher curvature, which was more pronounced for long diameter. The independent association of the discrepancy between 3D QCA and IVUS/OCT with vessel curvature and

catheter looseness is given by Table 4. The discrepancy in long diameters as assessed by 3D QCA and by IVUS was associated with vessel curvature (p = 0.02) and catheter looseness (p = 0.02). Linear regression equation was: (IVUS - 3D QCA) Long Diameter = 5.323 × Vessel Curvature + 0.204 × Catheter Looseness - 0.072. Similarly, the discrepancy in long diameters as assessed by 3D QCA and by OCT was associated with vessel curvature (p = 0.02) and catheter looseness (p = 0.04). Linear regression equation was: (OCT - 3D QCA) Long Diameter = 4.627 × Vessel Curvature + 0.137 × Catheter Looseness - 0.147.

Table 4. Independent Association of the Discrepancy between 3D QCA and IVUS/OCT Long Diameter with Vessel Curvature and Catheter Looseness

	IVUS - 3D QCA		OCT - 3D QCA	
	β* (95% CI)	p	β* (95% CI)	p
Vessel Curvature	5.32 (0.80 - 9.85)	0.02	4.63 (0.66 – 8.59)	0.02
Catheter Looseness	0.20 (0.04 - 0.37)	0.02	0.14 (0.10 – 0.26)	0.04

*Multiple linear regression adjusted for catheter looseness and vessel curvature. β indicates unstandardized β coefficient. CI = confidence interval; n = 40 vessels from 37 patients.

9.5 Discussions

Over the past years, the continuous development in coronary quantitative analysis has been motivated by the increasing need to better assess the true dimensions of vascular structures and by the on-line support of coronary interventions in the catheterization laboratories. It has been shown that suboptimal stent selection and deployment techniques were associated with significant risks of restenosis and thrombosis [13]. The choice of right stent size is thus important for the outcome of stenting procedures [14]. In modern catheterization laboratories, multiple imaging modalities including X-ray angiography and intracoronary imaging such as IVUS or OCT are widely available. However, when X-ray angiography is performed in conjunction with IVUS or OCT, lumen dimensions often show discrepancies in these imaging modalities. De Scheerder [15] reported smaller lumen size as assessed by IVUS in both normal and diseased coronary arteries, while Tsuchida [16] showed that IVUS measured larger lumen size in stented vessel, as compared with QCA. The difference to some extents can be attributed to the limitations in conventional QCA. To measure absolute lumen dimensions, the calibration procedure is required by conventional QCA, which can increase measurement variability and introduce the so-called out-of-plane magnification error [17]. When the vessel of interest is not aligned in the same plane as the calibration object, lumen size can be overestimated or

underestimated depending on the assessed position. Another important limitation in the assumption of circular cross-sections might lead to inaccurate assessments of lumen dimensions for noncircular lesions.

To address the limitations in conventional QCA, 3D QCA was proposed and developed. By restoring vascular structures in nature shape, 3D QCA was able to resolve some of these limitations, e.g., the vessel foreshortening and out-of-plane magnification errors, and reveal more details in the arterial cross-sections. In a bench study, Tu showed that 3D QCA was able to measure lumen dimensions with high accuracy and low variability on a wide range of acquisition angles [2]. When applied in patients with coronary artery disease, 3D QCA results agreed very well with vessel segment length as compared with IVUS using motorized pullback at constant pullback speed [4] and with true balloon length [18]. In addition, 3D QCA also enabled the so-called optimal viewing angles, which could be useful to minimize foreshortening and overlap in the ostial lesions and to guide interventional procedures [3, 5]. In short, 3D QCA is on the horizon to be used more often in routine clinical practice, due to the recent developments and support of automated calibration by most modern flat-panel X-ray systems. Particularly, 3D QCA can easily be integrated with IVUS or OCT to optimize the stent sizing and positioning during the interventional procedures [8]. While IVUS or OCT provides a wealth of information of the vessel wall, 3D QCA provides unique and complementary information including vessel tortuosity, curvature, and optimal viewing angles, et al. Such combined systems have high potential to be widely applied in routine clinical practice if a seamless workflow is implemented. It is thus desirable to understand the systematic discrepancy in order to interpret and combine different imaging modalities, especially for diffusely diseased vessels when coupled with IVUS/OCT imaging artifacts.

At present, however, limited evidence is available on the comparison between 3D QCA and IVUS or OCT. Bruining [19] evaluated 16 patients receiving a biodegradable stent and found that lumen diameter and area were smaller by IVUS than by 3D QCA. However, only vessel-based comparison was performed resulting in small sample size (11 vessels were evaluated by 3D QCA) and limited evidence. Schuurbiers [9] compared 3D QCA with IVUS on 1157 cross-sections in 10 coronary arteries using an offline co-registration tool, the ANGUS, to establish the correspondence between X-ray and IVUS images. The authors reported that 3D QCA systematically underestimated lumen area, as compared with quantitative IVUS. However, the evidence was limited by the fact that injection of diluted contrast agent during angiographic image acquisitions was required by ANGUS, which reduced the quality of the angiographic

images. To our knowledge, there is no direct comparison between 3D QCA and OCT in co-registered datasets. Therefore, we developed and used a novel, real-time co-registration approach to compare 3D QCA with IVUS and OCT. Our data demonstrated that both IVUS and OCT correlated well with 3D QCA in assessing lumen size at corresponding positions. The lumen size was larger by both IVUS and OCT, however, the agreement with 3D QCA tended to be slightly better by OCT than by IVUS: The differences between OCT and 3D QCA in short diameter, long diameter, and area were 0.14 mm (5.3%), 0.30 mm (10.2%), and 1.07 mm^2 (16.5%), respectively, while the differences between IVUS and 3D QCA were 0.16 mm (6.6%), 0.39 mm (13.8%), and 1.21 mm2 (21.3%), respectively. These results are in line with a recent study by Okamura [20], who evaluated the optical frequency domain imaging (OFDI) in comparison to IVUS and QCA in 19 patients undergoing stent implantation. The lumen area was found the largest by IVUS, followed by OFDI, and was the smallest by QCA. New in our study was that non-stented vessel segments were evaluated and 3D QCA was applied. Besides, a real-time co-registration approach was used to guarantee the point-to-point correspondence between different imaging modalities. Our results are also in agreement with previous studies by Gonzalo [1] and Suzuki [21], which showed that as compared with histology, both IVUS and OCT measured larger lumen size and the discrepancy was more pronounced by IVUS. Nevertheless, it should be borne in mind that our study does not allow a direct comparison between IVUS and OCT, since IVUS and OCT imaging were not performed in the same vessels. In addition, our study compared 3D QCA at the ED phase with OCT images which could correspond to any moment in the cardiac cycle, while 3D QCA was compared with IVUS images which were both selected at the ED phase. Last but not least, although the correspondence between different imaging modalities was established by the co-registration approach, the relatively slow pullback speed in IVUS imaging could increase local errors in the registration when coupled with patient respirations, resulting in a suboptimal match for the comparison between 3D QCA and IVUS.

Similar to the findings by Schuurbiers [9] in the comparison between 3D QCA and IVUS, our data also showed that the lumen area was larger by IVUS than by 3D QCA. However, the difference that we found by Bland-Altman plots indicated the discrepancy was more pronounced in larger vessels, while Schuurbiers reported that the trend (lumen area was larger in IVUS) tended to reverse in larger vessels (difference lumen area = 0.013 - 0.058 × average lumen area, $p< 0.05$). The difference could be explained by the fact that suboptimal angiographic image quality using diluted contrast agent was used by Schuurbiers, while we used

angiographic images with vessels well filled with contrast agent. In addition, different 3D QCA software packages and co-registration approaches were applied. Last but not least, there was no official guideline in the acquisition of angiographic images dedicated for 3D QCA in a broad clinical setting, making the interpretation of different studies difficult.

Another important finding of the present study was that vessel-based discrepancy between 3D QCA and IVUS or OCT tended to increase with the vessel curvature, especially in assessing long diameter. Tortuous vessels with high vessel curvature could lead to oblique imaging, i.e., the imaging catheter was positioned obliquely inside the lumen, and hence the circular lumen appeared elliptical in shape, resulting in overestimation of long diameter by IVUS or by OCT. This could partly explain our finding that the discrepancy between 3D QCA and IVUS or OCT was more pronounced in long diameter than in short diameter. Actually, the discrepancy in long diameter as demonstrated in this study was about two times larger than in short diameter, indicating that attention should be given when sizing the stent based on the long diameter from IVUS or OCT. An optimal stent selection should be applied from multiple assessments when combined with individual characteristics of the target vessel.

9.6 Limitations

The vessel-based comparison between different modalities was limited by the small sample size (n = 40). The ground truth of lumen size was not available for the comparison. In addition, 3D QCA was compared with IVUS and with OCT in different datasets and the study was limited by its retrospective in nature. For the 40 analyzed vessels from the patients undergoing IVUS imaging, intracoronary glyceryl trinitrate (GTN) was administered prior to the acquisitions of X-ray angiographic images used for 3D QCA and prior to IVUS imaging. However, for the 40 analyzed vessels from the patients undergoing OCT imaging, GTN was administrated prior to 3D QCA in 18 vessels and prior to OCT imaging in 20 vessels. GTN was not administrated or administrated after 3D QCA and OCT imaging in 16 vessels. For the rest, the information on whether and when GTN was administrated could not be retrieved. This could create bias in comparing IVUS and OCT. Therefore, further studies using the same coronary vessels are warranted before definite conclusions about the accuracy and agreement of these three major imaging modalities in the catheterization laboratory can be drawn.

9.7 Conclusions

Our comparison of co-registered 3D QCA and invasive imaging data suggested a bias towards larger lumen dimensions by IVUS and by OCT, which was more pronounced in larger and tortuous vessels.

9.8 References

1. Gonzalo N, Serruys PW, García-García HM, et al. Quantitative ex vivo and in vivo comparison of lumen dimensions measured by optical coherence tomography and intravascular ultrasound in human coronary arteries. Rev Esp Cardiol 2009; 62:615-624.
2. Tu S, Holm N, Koning G, Maeng M, Reiber JHC. The impact of acquisition angle difference on three-dimensional quantitative coronary angiography. Catheter Cardiovasc Interv 2011; 78:214-222.
3. Tu S, Jing J, Holm NR, Onsea K, Zhang T, Adriaenssens T, Dubois C, Desmet W, Thuesen L, Chen Y, Reiber JHC. In-vivo Assessment of Bifurcation Optimal Viewing Angles and Bifurcation Angles by Three-dimensional (3D) Quantitative Coronary Angiography. Int J Cardiovasc imaging 2011. Epub Ahead of Print. DOI: 10.1007/s10554-011-9996-x.
4. Tu S, Huang Z. Koning G, Cui K, Reiber JHC. A novel three-dimensional quantitative coronary angiography system: In-vivo comparison with intravascular ultrasound for assessing arterial segment length. Catheter Cardiovasc Interv 2010; 76:291-298.
5. Tu S, Hao P, Koning G, et al. In-vivo assessment of optimal viewing angles from X-ray coronary angiograms. EuroIntervention 2011; 7:112-120.
6. Reiber JHC, Serruys PW, Kooijman CJ, et al. Assessment of short-, medium-, and long-term variations in arterial dimensions from computer-assisted quantitation of coronary cineangiograms. Circulation 1985; 71: 280–288.
7. Joan C. Tuinenburg, Gerhard Koning, Andrei Rareş, Johannes P. Janssen, Alexandra J. Lansky, Johan H. C. Reiber. Dedicated bifurcation analysis: basic principles. Int J Cardiovasc Imaging 2011; 27: 167–174.
8. Tu S Holm NR, Koning G, Huang Z, Reiber JHC. Fusion of 3D QCA and IVUS/OCT. Int J Cardiovasc imaging 2011; 27:197–207.
9. 9. Schuurbiers JC, Lopez NG, Ligthart J, et al. In vivo validation of CAAS QCA-3D coronary reconstruction using fusion of angiography and intravascular ultrasound (ANGUS). Catheter Cardiovasc Interv 2009; 73:620–626.
10. Wahle A, Lopez JJ, Olszewski ME, et al. Plaque development, vessel curvature, and wall shear stress in coronary arteries assessed by X-ray angiography and intravascular ultrasound. Medical Image Analysis 2006; 10: 615-631.
11. Koning G, Dijkstra J, Birgelen C von, et al. Advanced contour detection for three-dimensional intracoronary ultrasound: a validation – in vitro and in vivo. Int J Cardiovasc Imaging 2002; 18:235-248.
12. Tu S, Koning G, Tuinenburg JC, et al. Coronary angiography enhancement for visualization. Int J Cardiovasc imaging 2009; 25:657–667.
13. Costa MA, Angiolillo DJ, Tannenbaum M, et al. Impact of stent deployment procedural factors on long-term effectiveness and safety of sirolimus-eluting stents (final results of the multicenter prospective STLLR trial). Am J Cardiol 2008; 101:1704–1711.
14. Gollapudi RR, Valencia R, Lee SS, et al. Utility of three-dimensional reconstruction of coronary angiography to guide percutaneous coronary intervention. Catheter Cardiovasc Interv 2007; 69:479–482.
15. De Scheerder I, De Man F, Herregods MC, et al. Intravascular ultrasound versus angiography for measurement of luminal diameters in normal and diseased coronary arteries. Am Heart J 1994; 127:243-251.

16. Tsuchida K, Serruys PW, Bruining N, et al. Two-year serial coronary angiographic and intravascular ultrasound analysis of in-stent angiographic late lumen loss and ultrasonic neointimal volume from the TAXUS II trial. Am J Cardiol 2007; 99:607-615.
17. Koning G, Hekking E, Kemppainen JS, et al. Suitability of the Cordis StabilizerTM marker guide wire for quantitative coronary angiography calibration: An in vitro and in vivo study. Catheter Cardiovasc Interv 2001; 52:334–341.
18. Rittger H, Schertel B, Schmidt M, et al. Three-dimensional reconstruction allows accurate quantification and length measurements of coronary artery stenoses. EuroIntervention 2009; 5:127–132.
19. Bruining N, Tanimoto S, Otsuka M, et al. Quantitative multi-modality imaging analysis of a bioabsorbable poly-L-lactid acid stent design in the acute phase: a comparison between 2 and 3D-QCA, QCU and QMSCT-CA. EuroIntervention 2008; 4:285–291.
20. Okamura T, Onuma Y, Garcia-Garcia HM, et al. First-in-man evaluation of intravascular optical frequency domain imaging (OFDI) of Terumo: a comparison with intravascular ultrasound and quantitative coronary angiography. EuroIntervention 2011; 6:1037-1045.
21. Suzuki Y, Ikeno F, Koizumi T, et al. In vivo comparison between optical coherence tomography and intravascular ultrasound for detecting small degrees of in-stent neointima after stent implantation. JACC Cardiovasc Interv 2008; 1:168-173.

CHAPTER 10

Summary and conclusions

10.1 Summary and Conclusions

Percutaneous coronary intervention (PCI) has undergone a remarkable evolution over the past decades. It is now regarded as one of the primary choices for the treatment of established ischemic heart disease. In addition to the continuous improvements in stent manufacturing, the impact of interventional techniques on the efficacy of the stenting procedure has gained increasing attentions. Suboptimal stent size selection and improper stent deployment may result in stent malapposition or incomplete lesion coverage; as a result, the risk of target vessel revascularization and thrombus formation can significantly increase. The conventional approach to assess coronary disease and to guide the subsequent intervention based only on two-dimensional angiographic images has been challenged. The modern approach requires the combination of multiple imaging modalities to be able to objectively assess coronary disease and to effectively guide the intervention, especially for patients with complex lesions.

This thesis focuses on the development and validation of a new three-dimensional quantitative coronary angiography (3D QCA) system including its derived clinical applications, e.g., the assessment of optimal viewing angles and bifurcation dimensions. Furthermore, based on the 3D angiographic reconstruction, intracoronary imaging devices such as intravascular ultrasound (IVUS) and optical coherence tomography (OCT) can be registered with the X-ray images, which provides the interventional

cardiologist with "roadmap" from 3D angiography and details of plaque composition and size at every position along the vessel of interest.

Image interpretation might benefits from high visualization quality. Due to the low-pass characteristics of X-ray systems, the visibility of coronary vascular structures in the acquired angiographic projections is often limited (images are blurred), especially when zooming in the interesting parts of the image to observe the details. **Chapter 2** presented a new nonlinear enhancement algorithm, the stick-guided lateral inhibition (SGLI), to enhance the visualization of vascular structures. The proposed algorithm simulated the enhancing mechanisms integrated in the eyes of human beings and of many animals. By integrating asymmetric sticks to approximate vessel edges for the guiding of the inhibition process, the algorithm had the ability to accentuate the intensity gradients of interesting vessel edges, while suppressing the increase of noise. The validation study on comparing SGLI with the conventional unsharp masking (UM) algorithm by 10 experienced QCA analysts and 9 cardiologists indicated that the SGLI algorithm performed significantly better than the UM algorithm.

Accurate and fast reconstruction of coronary vascular structures based on routine biplane angiographic acquisitions is often difficult when coupled with strong image noise and various system distortions including the isocenter offset, since the establishment of a good correspondence between the two angiographic projections, which is of utter most importance to the 3D angiographic reconstruction, is not a trivial work by using the epipolar line constraint under such difficult circumstances. **Chapter 3** presented a new approach using one to three reference points to correct for the isocenter offset. When small perspective viewing angles and noisy arterial contours were present, the use of the epipolar constraint to establish the correspondence was improved by building a distance transformation matrix and subsequently by searching the optimal corresponding path. The proposed 3D QCA system was validated using wire phantoms. The segment length assessed by 3D QCA correlated well with the true wire segment length ($r^2 = 0.999$) and the accuracy was 0.04 ± 0.25 mm ($P < 0.01$). Regarding with bifurcation optimal viewing angles, 3D QCA slightly underestimated the rotation angle (difference: -1.5º ± 3.6º, $P < 0.01$), while no significant difference was observed for the angulation angle (difference: -0.2º ± 2.4º, $P = 0.54$).

The lack of standard operation procedures and analysis data for 3D QCA has somehow precluded its wide application into current clinical practice. So far there is no official guideline in the angiographic acquisition dedicated for 3D QCA in a broad clinical setting. In general, the operator selects two angiographic views for the subsequent 3D reconstruction. The

optimal selection criteria remain unclear. Particularly, the impact of acquisition angle difference (AAD) of the two angiographic views on the 3D reconstruction and quantitative analysis has not been studied. **Chapter 4** investigated the impact of AAD on the vessel dimensions as assessed by 3D QCA using phantom experiments. X-ray angiographic images were recorded at multiple angiographic projections for a brass phantom and for a silicone bifurcation phantom. The projections were randomly matched and used for the 3D reconstruction and analysis. The study showed that AAD did not have significant impact on 3D QCA for circular moderate lesions. For the assessment of bifurcation dimensions, the correlation between AAD and 3D QCA was only significant for the distal bifurcation angle. The correlation was weak (R^2 = 0.256, p = 0.001, linear regression equation: Error = 0.043 × AAD – 0.590) and it indicated that the measurement error tended to increase as AAD became larger. In addition, the study also demonstrated that 3D QCA can be used to assess vessel dimensions, including diameter stenosis, reference diameter, lesion length, and bifurcation angles, with high accuracy and low variability in a wide range of acquisition angles.

IVUS has become one of the dominant imaging technologies used in the catheterization laboratories to understand vessel biology and to guide interventional procedures. During the procedure, arterial segment length can be reliably assessed when using motorized pullback in the image acquisition. **Chapter 5** compared arterial segment length as assessed in-vivo by 3D QCA and by IVUS using motorized pullback. 37 vessel segments of interest were identified from both angiographic and IVUS images. 3D QCA had an excellent correlation with IVUS (R^2 = 0.98, p < 0.001). However, the 3D QCA segment length was slightly longer than the IVUS segment length (15.42 ± 6.02 mm vs. 15.12 ± 5.81 mm, p = 0.040). The difference was found to be associated with the accumulated curvature of the assessed segment (p = 0.015). After refining the difference by the correlation, the average difference of the two measurements decreased from 0.30 ± 0.86 mm (p = 0.040) to 0.00 ± 0.78 mm (p = 0.977). On the other hand, an average foreshortening of 7% ± 6% was found in the 2D QCA measurements for the same segments, indicating that 3D QCA was superior to 2D QCA in assessing arterial segment length.

Optimal viewing angles are characterized by having minimal vessel foreshortening and overlap. Conventionally, in order to obtain the optimal views, operators have to interactively adjust the C-arm of the X-ray system guided by the 2D angiographic images. This "trial-and-error" approach could significantly increase the volume of contrast medium used and the radiation exposure to the patient and staff. Besides, due to the

variable anatomy of each individual patient combined with the variable orientation of the heart in the thorax, the chosen angle can be quite different from the true optimal viewing angle.

Chapter 6 presented a novel approach to predict vessel overlap and subsequently determine the optimal angiographic viewing angles for a selected coronary (target) segment from X-ray coronary angiography, without the need to reconstruct the whole coronary tree in 3D, such that subsequent interventions could be carried out from the best view, with no or minimal overlap. The approach was retrospectively validated in 67 patients who underwent both coronary angiography and stenting. The predicted overlap conditions were compared with the true overlap conditions on 235 available angiographic views and the result demonstrated that the accuracy of the overlap prediction was 100%. In addition, two experienced interventional cardiologists independently evaluated the success of the software viewing angle (SVA) with respect to the expert viewing angle (EVA). In about one third of the cases, the cardiologists chose that SVA was significantly better than EVA, while there was no case that the cardiologists chose that EVA was better. According to the quantitative comparison, SVA had much less foreshortening than EVA (1.6%±1.5% vs 8.9%±8.2%, $p < 0.001$). In short, the validation clearly demonstrated the advantage of our proposed approach as compared with the expert working views.

Correct assessment of bifurcation lesion anatomy, especially the ostia of branches, is essential to choose the right treatment strategy in PCI. The anatomy-defined bifurcation optimal viewing angle (ABOVA) is characterized by having an orthogonal view of the bifurcation, such that overlap and foreshortening at the ostium are minimized. However, due to the mechanical constraints of the X-ray systems, certain deep angles cannot be reached by the C-arm of the X-ray systems. In addition, ABOVA only minimizes the overlap between the main (parent) vessel and the sidebranch at the ostium. Other major coronary arteries could also overlap with the target bifurcation when projected at ABOVA, possibly leading to significant impediment of the visualization of the target bifurcation. In these cases, second best or, so-called obtainable bifurcation optimal viewing angle (OBOVA) has to be used as an alternative.

Chapter 7 studied the distributions of ABOVA and OBOVA as assessed by 3D QCA in a typical patient population including 194 obstructed bifurcations from three medical centers. The study found that ABOVA could not be reached by the X-ray systems in 56.7% of the patient population. This occurred more frequent in LM/LAD/LCx (81.6%) and LAD/Diagional (78.4%), followed by PDA/PLA (48.8%) and was uncommon in LCx/OM (17.6%). These data suggest that in about half of

the population, a second optimal view, i.e., OBOVA, should be used as an alternative. The study also demonstrated that both ABOVA and OBOVA distributed sparsely with large ranges of variation in all main coronary bifurcations, indicating that there are no fixed views that can always optimize the visualization of the main coronary bifurcations. The true bifurcation optimal view is subject to the unique anatomy of each individual bifurcation. Given the fact that the viewing angles should be within the reaching rang of the X-ray systems, the optimal view for the left main bifurcation distributes mainly at the Caudal view (35±16 Caudal) but spreads across the LAO/RAO view (4±39 LAO); the optimal view for LAD/Diagonal distributes mainly at the Cranial view (33±5 Cranial), but spreads across the LAO/RAO view (14±28 LAO); the optimal view for LCx/OM distributes mainly at the Caudal view (25±13 Caudal), but spreads across the LAO/RAO view (18±31 LAO); the optimal view for PDA/PLA distributes mainly at the Cranial view (29±15 Cranial) and the LAO view (28±25). Another finding of the study is that the proximal bifurcation angles (PBAs) as assessed by 3D QCA in LAD/Diagonal, LCx/OM, and PDA/PLA were very much comparable and not statistically different (p = 0.133), being 151°±13°, 146°±18°, and 145°±19°, respectively. However, the distal bifurcation angles (DBAs) in LAD/Diagonal was smaller than LCx/OM (p = 0.004) and PDA/PLA (p = 0.001), being 48°±16° vs 57°±16°, and 59°±17°, respectively. The left main bifurcation had the smallest PBA (128°±24°) and the largest DBA (80°±21°).

It has been well recognized for many years that despite the wide availability of the angiogram and the QCA, an angiogram is only a lumenogram, and that the disease is in the vessel wall. For proper decision making purposes, the interventionalist must combine the plaque information from invasive imaging technologies such as IVUS or OCT. However, the fact that these invasive imaging modalities do not preserve the vessel shape information could challenge the mental mapping of corresponding segments between X-ray angiography (XA) and IVUS or OCT, especially when no landmark was available on the segments of interest. **Chapter 8** presented a new approach for the on-line co-registration of 3D QCA with IVUS/OCT. The approach only required the operator to reconstruct the arterial centerline from two angiographic images. The step of reconstructing the IVUS/OCT pullback trajectory as required by conventional approaches was replaced by a distance mapping algorithm which estimated the corresponding IVUS/OCT cross-sectional image for each position along the reconstructed arterial centerline. By this approach, the disadvantage of using diluted contrast agent during angiographic image acquisitions, as required by conventional registration

approaches in order to simultaneously visualize the arterial lumen and the IVUS/OCT catheter, was resolved and as a result, the quality of 3D QCA was improved and less manual corrections were required in the lumen contour detection in 3D QCA. The approach was validated in 12 silicone phantoms scanned by XA, IVUS and OCT, and in 24 patients who underwent both diagnostic angiography and IVUS. Stent borders or vessel sidebranches were used to evaluate the registration error and the error was demonstrated to be quite small, being 0.03 ± 0.32 mm (p = 0.75) for the XA-IVUS phantom registration, 0.05 ± 0.25 mm (p = 0.49) for the XA-OCT phantom registration, and 0.03 ± 0.45 mm (p = 0.67) for the XA-IVUS in-vivo registration, respectively.

Coronary lumen dimensions often show discrepancies when assessed by X-ray angiography and by IVUS or OCT. At present, very limited evidence is available on the comparison between 3D QCA and IVUS or OCT. One source of error concerns a possible mismatch in the selection of corresponding regions for the comparison. **Chapter 9** used the proposed co-registration approach to eliminate the error concerning the possible mismatch and to compare lumen dimensions in 80 vessels from 74 patients by 3D QCA and by IVUS or OCT. The study demonstrated that both IVUS and OCT correlated well with 3D QCA in assessing lumen size at corresponding positions. The lumen size was larger by both IVUS and OCT, however, the agreement with 3D QCA tended to be slightly better by OCT than by IVUS: The differences between OCT and 3D QCA in short diameter, long diameter, and area were 0.14 mm (5.3%), 0.30 mm (10.2%), and 1.07 mm^2 (16.5%), respectively, while the differences between IVUS and 3D QCA were 0.16 mm (6.6%), 0.39 mm (13.8%), and 1.21 mm2 (21.3%), respectively. Another important finding of the study was that vessel-based discrepancy between 3D QCA and IVUS or OCT tended to increase with the vessel curvature, especially in assessing long diameter. Tortuous vessels with high vessel curvature could lead to oblique imaging, i.e., the imaging catheter was positioned obliquely inside the artery, and hence the circular lumen appeared elliptical in shape, resulting in overestimation of long diameter by IVUS or by OCT. This should be taken into consideration when using IVUS or OCT to determine the right stent size in clinical practice.

In conclusion, this thesis proposes several novel algorithms including X-ray angiographic image enhancement, 3D angiographic reconstruction, angiographic overlap prediction, and the co-registration of X-ray angiography with intracoronary imaging devices, such as IVUS and OCT. The algorithms have been integrated into prototype software packages that were installed and validated at a number of clinical centers around the world. The feasibility of using such software packages in typical clinical

population was verified, while the advantages and accuracy of the proposed algorithms were clearly demonstrated by phantoms and in-vivo clinical studies. In addition, based on the proposed approaches and the conducted studies, this thesis reports several findings including the impact of acquisition angle difference on 3D QCA, the clinical characteristics of bifurcation optimal viewing angles and bifurcation angles, and the discrepancy of lumen dimensions as assessed by 3D QCA and by IVUS or OCT. Having said so, we have realized our goals stated in Section 1.3.

10.2 Future Works

Coronary artery disease (CAD) is still one of the leading causes of mortality and mobility worldwide. The continuous drive for optimal patient care demands intuitive visualization of the coronary vascular structures as well as accurate and reproducible quantifications. While X-ray coronary angiography provides an excellent global overview of the coronary vascular structures, IVUS and OCT document detailed plaque composition and lesion extent in the vessel wall. This thesis has only addressed the problem of corresponding IVUS or OCT cross-sectional images with X-ray angiographic images. The complete fusion of these imaging modalities to visualize and quantify the vessel wall in naturally bended vessel shape has not yet been answered. Future works will be directed at developing new algorithms that are able to restore the vessel wall in the bended 3D shape. In addition, when IVUS or OCT imaging is performed at both the main (parent) vessel and the sidebranch, the images from the two pullbacks need to be merged and oriented in 3D at the bifurcation, in such a way that the anatomy of the bifurcation can be appreciated in high detail.

Despite the great advantage of imaging the complete coronary anatomy, the fusion of X-ray angiography and IVUS or OCT could only assess lesion severity from anatomical perspectives. Combined evaluation of coronary anatomy and myocardial ischemia has the potential to improve the diagnosis, which could translate into improved care of patients. Currently, fractional flow reserve (FFR) is regarded as the standard of reference to assess the functional severity of coronary stenosis in the catheterization laboratories. The integration of the co-registration approach with FFR might be the next step towards an optimal approach to assess ischemic CAD and to guide coronary interventions.

CHAPTER 11

Samenvatting en Conclusies

11.1 Samenvatting en conclusies

Percutane coronaire interventies (PCIs) hebben de afgelopen decades een enorme evolutie ondergaan. Deze techniek wordt nu als een van de primaire keuzes gezien voor de behandeling van ischemische hartziekten. Naast de continue verbetering en innovatie in de productie van de stents, is er ook continue aandacht om de interventionele technieken zelf te verbeteren en daarmee het succes van de interventie. Een suboptimale selectie van de stent afmetingen en een suboptimale stent-plaatsing kunnen resulteren in een stent-malappositie of incomplete bekleding van de vernauwing, hetgeen kan bijdragen aan een significante verhoging op de kans van een noodzakelijke revascularisatie in de toekomst, danwel trombus formatie met alle gevolgen vandien. De conventionele benadering voor het vaststellen van mogelijke afwijkingen in het coronaire vaatsysteem en de ondersteuning van de interventie middels de standaard twee-dimensionale angiografische röntgenbeelden, is aan verbetering toe. Met de moderne beschikbare technologieën moet op basis van een combinatie van verschillende beeldmodaliteiten op een meer objectieve manier de ernst van de coronaire afwijkingen vastgesteld kunnen worden en op een meer effectieve wijze de interventie ondersteund kunnen worden, in het bijzonder bij patiënten met complexe vernauwingen.

De focus van dit proefschrift is gericht op de ontwikkeling en validatie van een nieuw drie-dimensionaal systeem voor de kwantitatieve coronair angiografie (3D QCA) inclusief afgeleide klinische applicaties, zoals de bepaling van de optimale opnamehoeken en de afmetingen van

bifurcaties. Verder kunnen de beelden van intravasculaire opnametechnieken, zoals intravasculaire ultrageluid (IVUS) en optische coherentie tomografie (OCT) worden geregistreerd met de röntgenbeelden, zodat de interventie-cardioloog belangrijke additionele informatie verkrijgt tijdens de procedure, waarbij de 3D angiografie functioneert als een "roadmap" en de plakcompositie en nauwkeurige vaatwand afmetingen beschikbaar komen op iedere positie langs het desbetreffende vaattraject.

Visuele beeldinterpretatie wordt beter naarmate de beeldkwaliteit beter is. Vanwege de laagdoorlaat-karakteristieken van de röntgensystemen, is de visualisatie van de coronaire vaatstructuren in de opgenomen angiografische projecties vaak beperkt (beelden zijn relatief vaag), in het bijzonder wanneer ingezoomed wordt op interessante delen van het beeld om de details verder te bestuderen. In **hoofdstuk 2** wordt een nieuw niet-linear beeld-opscherpend algoritme gepresenteerd, het zogenaamde stick-guided lateral inhibition (SGLI) filter, waarmee de visualisatie van vasculaire structuren verbeterd wordt. Het voorgestelde algoritme simuleert de mechanismes zoals die ook plaatsvinden in de ogen van mensen en van vele diersoorten. Door de integratie van asymmetrische "stokjes" waarmee de lokale vaatwanden worden benaderd, is het algoritme in staat om de intensiteits-overgangen van vaatranden te accentueren, waarbij de toename in ruis wordt onderdrukt. Uit een evaluatiestudie waarbij het SGLI-algoritme is vergeleken met het conventionele unsharp-masking (UM) algoritme door 10 ervaren QCA analisten en 9 cardiologen, bleek dat het SGLI algoritme aanzienlijk beter scoorde dan het UM algoritme.

Nauwkeurige en snelle reconstructie van de coronaire vaatstructuren gebaseerd op routinematige biplane-angiografische opnamen is vaak moeilijk, vanwege sterke ruis in de beelden en de verschillende systeemvervormingen, zoals de isocenter offset. Het bepalen van een goede correspondentie tussen de beide angiografische projecties, welke cruciaal is voor de kwaliteit van de 3D angiografische reconstructie, is niet triviaal wanneer gebruik wordt gemaakt van de zogenaamde epipolar lijn correspondentie. In **hoofdstuk 3** wordt een nieuwe benadering gepresenteerd, waarbij één tot drie referentiepunten worden gebruikt om te corrigeren voor de isocenter offset. In gevallen van kleine hoekverschillen tussen de twee projecties en ruizige vaatcontouren, wordt het gebruik van de epipolar lijn correspondentie verbeterd door het formuleren van een "distance transformation matrix" gevolgd door het zoeken van een optimaal corresponderend pad. Het voorgestelde 3D QCA systeem is gevalideerd middels een draadfantoom. De segmentlengte bepaald met 3D QCA kwam goed overeen met de werkelijke segment

lengte (r^2 = 0.999) en de nauwkeurigheid en precisie waren 0.04 ± 0.25 mm (P < 0.01). Wat betreft de optimale opnamehoeken voor bifurcaties, onderschatte de 3D QCA enigszins de rotatiehoek (verschil: -1.5º ± 3.6º, P < 0.01), terwijl er geen significant verschil werd gevonden voor de angulatie hoek (verschil: -0.2º ± 2.4º, P = 0.54).

Het gebrek aan standard operation procedures (SOPs) en analyse gegevens voor 3D QCA heeft de brede toepassing in de klinische praktijk enigszins beperkt. Tot nu toe bestaat er geen officiële richtlijn voor de angiografische beeldacquisitie voor 3D QCA voor breed klinisch gebruik. Voor 3D QCA selecteert de analist twee angiografische opnamen, maar optimale selectiecriteria voor de opnamen zijn onduidelijk. In het bijzonder is de invloed van de angiografische hoekverschillen (AAD) tussen de beide opnamen op de 3D reconstructie en de afgeleide parameters nog nooit bestudeerd. **In hoofdstuk 4** wordt daarom de invloed van de AAD op de vaatafmetingen, berekend met 3D QCA, bestudeerd met behulp van fantoom experimenten. Röntgen-angiografische opnames van een koper fantoom en van een silicoon bifurcatie fantoom werden vastgelegd voor een groot aantal angiografische projecties. De projecties werden willekeurig gecombineerd en gebruikt voor de 3D reconstructie en analyse. De resultaten toonden dat de AAD geen significante invloed heeft op de resultaten van de 3D QCA voor circulaire en middelmatige vernauwingen. Voor de bepaling van de bifurcatie-afmetingen was de correlatie tussen AAD en 3D QCA parameters alleen significant voor de hoek tussen de distale vaten. De correlatie was zwak (R^2 = 0.256, p = 0.001, lineaire regressie vergelijking: fout = 0.043 × AAD – 0.590) en er werd een trend gevonden waarbij de meetfout groter werd naarmate de AAD hoek groter was. De studie demonstreerde ook duidelijk dat 3D QCA gebruikt kan worden voor de bepaling van de vaatafmetingen, inclusief diameter vernauwing, referentie-diameter, lengte van de vernauwing, en bifurcatiehoeken, met een hoge nauwkeurigheid en geringe variabiliteit in een groot bereik van opnamehoeken.

IVUS is één van de belangrijkste beeldtechnieken geworden in het catheterisatie laboratorium voor het begrip van de vaatwand anatomie en voor het ondersteunen van de interventie procedures. Gedurende de procedure kunnen lengte metingen nauwkeurig worden uitgevoerd, als de beeldacquisitie gebeurt met een zogenaamde motorized pullback, waarbij de catheter met constante snelheid middels een motortje wordt teruggetrokken. **In hoofdstuk 5** wordt de arteriële segmentlengte bepaald op basis van in-vivo 3D QCA en IVUS motorized pullback. 37 vaatsegmenten werden geïdentificeerd waarvoor zowel angiografische als overeenkomstige IVUS-beelden beschikbaar waren. Er werd een

uitstekende correlatie gevonden tussen de 3D QCA en de IVUS segment lengte (R^2 = 0.98, p < 0.001). De 3D QCA segment-lengte was echter iets langer dan de IVUS segment-lengte (15.42 ± 6.02 mm vs. 15.12 ± 5.81 mm, p = 0.040). Het verschil kan worden verklaard door de geaccumuleerde curvatuur van het desbetreffende segment (p = 0.015). Na correctie voor het verschil op basis van deze correlatie, nam het gemiddelde verschil af van 0.30 ± 0.86 mm (p = 0.040) tot 0.00 ± 0.78 mm (p = 0.977). Een gemiddelde verkorting van 7% ± 6% werd gevonden in de 2D QCA metingen voor dezelfde segmenten, hetgeen aangeeft dat de 3D QCA superieur is boven de 2D QCA voor het bepalen van de segment lengte.

Optimale opnamehoeken worden gekarakteriseerd door minimale verkorting en overlap van vaten. In de praktijk moet de interventie-cardioloog de C-arm van het röntgensysteem zodanig draaien dat de beste hoeken ontstaan op basis van de visuele interpretatie van de 2D angiografische beelden. Deze "trial-and-error" methode kan leiden tot een aanzienlijke toename van de hoeveelheid contrastvloeistof die aan de patiënt wordt toegediend en van de stralingsbelasting voor patiënt en het onderzoeks team. Daarnaast kan de gekozen opnamehoek zeer verschillend zijn van de werkelijk optimale hoek vanwege de variabele anatomie van iedere individuele patiënt en de variabele anatomie van het hart in de thorax.

In **hoofdstuk 6** is een nieuwe techniek gepresenteerd om de mate van vaatoverlap en vervolgens aan de hand van de standaard angiografische opnamen de optimale opnamehoeken van een geselecteerd coronair-segment te bepalen om de vaatoverlap te voorkomen, , zonder eerst de gehele coronairboom in 3D te moeten reconstrueren; op basis van die gegevens kunnen dan de interventies uitgevoerd worden met de beste aanzichten. Deze benadering is retrospectief gevalideerd in een populatie van 67 patiënten, die selectieve coronairangiografie en stentplaatsing ondergingen. De voorspelde overlap condities werden vergeleken met de werkelijke mate van overlap op een totaal van 235 beschikbare angiografische projecties, en de resultaten toonden aan dat de nauwkeurigheid van de overlap voorspelling 100% was. Daarnaast hebben twee ervaren interventie-cardiologen onafhankelijk van elkaar het succes van de software viewing angle (SVA) vergeleken met de expert viewing angle (EVA). In ongeveer eenderde van de gevallen gaven de cardiologen aan dat de SVA significant beter was dan de EVA, terwijl er geen situatie was waarbij de cardiologen besloten dat de EVA beter was. Op basis van kwantitatieve analyse, was de mate van verkorting met SVA veel kleiner was dan met EVA (1.6%±1.5% t.o.v 8.9%±8.2%, p < 0.001).

De juiste bepaling van de anatomie van de bifurcatievernauwing- in het bijzonder die van de ostia van zijtakken - is essentieel in de keuze van de juiste behandelstrategie in PCI. De op basis van de bifurcatie anatomie bepaalde optimale opnamehoek (ABOVA: anatomy-defined bifurcation optimal viewing angle) wordt gekarakteriseerd door een orthogonaal aanzicht van de bifurcatie, zodanig dat overlap en verkorting bij het ostium zijn geminimaliseerd. Vanwege de mechanische beperkingen van de röntgensystemen, kunnen echter bepaalde opname hoeken niet gerealiseerd worden door de C-arm van de röntgensystemen. Daarnaast minimaliseert de ABOVA alleen de overlap tussen de hoofdtak en de zijtak bij het ostium. Andere grote coronairvaten kunnen ook overlap vertonen met de doel-bifurcatie wanneer die geprojecteerd worden onder de ABOVA-hoek, hetgeen mogelijk kan leiden tot een significante beperking in de visualisatie van de doel-bifurcatie. In die gevallen moeten tweede keuzes of, zogenaamde haalbare bifurcatie optimale aanzichten (OBOVA: obtainable bifurcation optimal viewing angle) als alternatief worden gebruikt.

In **hoofdstuk 7** is de distributie van de ABOVA en OBOVA hoeken op basis van de 3D QCA bestudeerd in een patiëntenpopulatie uit drie medische centra, waarbij 194 bifurcaties met obstructies zijn geanalyseerd. Uit de studie bleek dat in 56.7% van de gevallen de ABOVA hoek niet kon worden gerealiseerd door het röntgensysteem. Dit betrof met name obstructies in de LM/LAD/LCx (81.6%) en LAD/Diagional (78.4%), gevolgd door de PDA/PLA (48.8%), maar nauwelijks in de LCx/OM (17.6%). Deze gegevens suggereren dat in ongeveer de helft van de gevallen een tweede optimaal aanzicht (een OBOVA) als alternatief moet worden gebruikt. Deze studie heeft ook aangetoond, dat de spreiding in de ABOVA en OBOVA hoeken voor alle coronaire bifurcaties groot is, en dat er dus geen standaard hoeken te vinden zijn waarbij de visualizatie van de coronaire bifurcaties altijd optimaal zijn. De werkelijke bifurcatie optimale view wordt bepaald door de unieke anatomie van iedere individuele bifurcatie. Gegeven de eis dat de aanzichten wel ingesteld moeten kunnen worden door het röntgensysteem, ligt de optimale hoek voor de hoofdtak bifurcatie vooral verdeeld rond caudaal (35±16 Caudal), maar met een grotere LAO/RAO spreiding (4±39 LAO); de optimale hoek voor de LAD/diagonaal ligt vooral rond craniaal (33±5 Cranial), maar veel meer variabel in de LAO/RAO richting (14±28 LAO); de optimale hoek voor de LCx/OM is vooral caudaal (25±13 Caudal), maar veel meer variabel in de LAO/RAO richting (18±31 LAO), terwijl tenslotte de optimale hoek voor de PDA/PLA vooral geconcentreerd is rond craniaal (29±15 Cranial) en LAO view (28±25). Een ander resultaat van deze studie is dat de proximale bifurcatie hoeken (PBAs) bepaald op basis van

3D QCA in de LAD/Diagonal, LCx/OM, en PDA/PLA weinig van elkaar verschilden: respectievelijk 151°±13°, 146°±18°, en 145°±19°, en de verschillen zijn niet statistisch significant (p = 0.133. De distale bifurcatiehoeken (DBAs) in de LAD/Diagonal waren echter kleiner dan die in de LCx/OM (p = 0.004) en in de PDA/PLA (p = 0.001), zijnde respectievelijk 48°±16, 57°±16°, en 59°±17°. De bifurcatie in de hoofdtak had de grootste PBA (128°±24°) en de grootste DBA (80°±21°).

Het is al vele jaren bekend, dat ondanks de brede toepassing van het angiogram en de QCA, een angiogram slechts een lumenogram is, dat wil zeggen een afbeelding van de binnenkant van een vat, maar dat het echte ziekteproces in de vaatwand plaats vindt. Om de juiste beslissingen te kunnen nemen, moet de interventionalist de gegevens van het angiogram combineren met die van de plakinformatie op basis van invasieve beeldtechnieken, zoals IVUS en OCT. Die invasieve beeldtechnieken behouden echter niet de informatie over de vorm van het vat, hetgeen de mentale correspondentie van overeenkomstige segmenten op basis van het angiogram en IVUS of OCT bemoeilijkt, zeker wanneer er geen herkenningspunten beschikbaar zijn voor de desbetreffende segmenten. **In hoofdstuk 8** wordt een nieuwe benadering gepresenteerd voor de on-line registratie van 3D QCA en IVUS/OCT. Deze benadering vereist alleen dat de arteriële hartlijn van de twee angiografische projecties wordt gereconstrueerd. Voor de reconstructie van het IVUS/OCT pullback traject wordt in ons geval gebruik gemaakt een zogenaamde distance mapping algoritme, dat voor ieder punt langs de gereconstrueerde arteriële hartlijn de overeenkomstige IVUS/OCT doorsnede schat. Door deze benadering wordt het nadeel van het gebruik van de contrastvloeistof tijdens de angiografische opname teneinde simultaan het lumen en de IVUS/OCT catheter te kunnen afbeelden, opgelost en als resultaat is de 3D QCA verbeterd en waren er minder manuele correcties nodig in de lumen contour detectie in 3D QCA. Deze aanpak is gevalideerd in een twaalftal silicoon fantomen, die opgenomen zijn met röntgen, IVUS en OCT, en in 24 patiënten, van wie zowel diagnostische angiografie als IVUS data beschikbaar was. De stent-uiteinden danwel zijtakken van de vaten werden gebruikt om de registratiefouten te bepalen. De fouten waren vrij klein: Voor de XA-IVUS fantoom registratie 0.03 ± 0.32 mm (p = 0.75), voor de XA-OCT fantoom registratie 0.05 ± 0.25 mm (p = 0.49), en 0.03 ± 0.45 mm (p = 0.67) voor de XA-IVUS in-vivo registratie.

Er zijn vaak discrepanties geconstateerd in de coronaire lumen afmetingen zoals die bepaald zijn op basis van de röntgen-angiografie en de IVUS of OCT. Op dit moment is zeer beperkte informatie beschikbaar over de vergelijking tussen 3D QCA en IVUS of OCT. Een mogelijke foutenbron betreft een mogelijke mismatch in de selectie van de

overeenkomstige vaatposities. In **hoofdstuk 9** is de voorgestelde co-registratie benadering gebruikt om de fout in de mogelijke mismatch te elimineren en om de lumen afmetingen te vergelijken in 80 vaten van 74 patiënten met 3D QCA en IVUS of OCT. De studie toont aan dat zowel IVUS als OCT goed correleert met de 3D QCA in de bepaling van de lumen afmetingen op overeenkomstige posities. De lumen afmetingen waren groter voor zowel IVUS als OCT, maar de overeenkomst met 3D QCA lijkt iets beter te zijn voor OCT dan voor IVUS. De verschillen tussen OCT en 3D QCA in de korte diameter, de lange diameter en de doorsnede waren respectievelijk 0.14 mm (5.3%), 0.30 mm (10.2%), and 1.07 mm^2 (16.5%), terwijl de verschillen tussen IVUS en 3D QCA respectivelijk 0.16 mm (6.6%), 0.39 mm (13.8%), en 1.21 mm2 (21.3%) waren. Een ander belangrijk resultaat van het onderzoek was dat de discrepantie tussen de 3D QCA en IVUS of OCT groter lijkt te worden bij toenemende curvatuur van het vat, in het bijzonder in de bepaling van de lange diameter.

Kronkelige vaten met veel curvatuur kunnen leiden tot schuine opnames, d.w.z. dat de afbeeldingscatheter schuin in het vat ligt, en als gevolg daarvan worden cirkelvormige doorsneden ellipsvorming, hetgeen leidt tot een overschatting van de lange diameter met IVUS of OCT. Deze potentiële fout moet worden meegenomen in de klinische praktijk wanneer IVUS of OCT wordt gebruikt om de juiste stent-maat te bepalen.

Concluderend worden in dit proefschrift verschillende innovatieve algoritmes gepresenteerd op de gebieden van röntgen-angiografische beeldverbetering, 3D angiografische reconstructie, angiografische vaatoverlap predictie en de co-registratie van de röntgen-angiografie met IVUS of OCT. De algoritmes zijn geïmplementeerd in een software prototype dat in meerdere klinische centra in de wereld is geïnstalleerd en gevalideerd. De toepasbaarheid van een dergelijk prototype software-pakket in een typische klinische omgeving is aangetoond, waarbij de voordelen en de nauwkeurigheid van de voorgestelde algoritmes duidelijk zijn gedemonstreerd in fantoom en in-vivo klinische studies. Daarnaast wordt in dit proefschrift een aantal belangrijke resultaten gepresenteerd, zoals de invloed van de angiografische hoekverschillen op de 3D QCA, en de discrepantie in lumen-afmetingen tussen 3D QCA en IVUS of OCT. Op basis van al deze resultaten kan geconcludeerd worden dat onze oorspronkelijke doelstellingen, zoals geformuleerd in sectie 1.3, gerealiseerd zijn.

11.2 Toekomstige Ontwikkelingen

Coronair vaatlijden (CAD) is nog altijd een van de belangrijkste oorzaken voor ziekte en overlijden in de wereld. De continue zoektocht naar een optimale behandeling van de patiënt vereist een intuïtieve

visualisatie van de coronaire vaatstructuren en een nauwkeurige en reproduceerbare kwantificatie. Terwijl de coronaire röntgen-angiografie een uitstekend globaal overzicht geeft van de coronaire vasculatuur, geven IVUS en OCT gedetailleerde informatie over de plakcompositie en de omvang van de laesie in de vaatwand. In dit proefschrift is alleen het probleem van de correspondentie tussen de vatdoorsnede-beelden van IVUS en OCT met de angiografische beelden behandeld. De complete fusie van deze beeldmodaliteiten waarbij de vaatwand in de natuurlijke gebogen vorm van de vaten wordt gevisualiseerd en gekwantificeerd is nog niet uitgewerkt. Daarom dient toekomstig werk gericht te zijn op de ontwikkeling van nieuwe algoritmes die ook de vaatwand in de gebogen 3D-vorm nauwkeurig kan afbeelden. Daarnaast dienen technieken te worden ontwikkeld voor het fuseren van twee pullbacks bij een bifurcatie, namelijk die van de hoofdtak en van de zijtak, en dan nog in 3D, en op een zodanige wijze dat de anatomie van de bifurcatie met een grote mate van detail kan worden geëvalueerd.

Ondanks het grote voordeel dat de gehele coronair-anatomie kan worden afgebeeld, kan de fusie van de röntgen-angiografie en de IVUS of OCT de ernst van de ziekte slechts vaststellen vanuit anatomisch perspectief. De gecombineerde evaluatie van de coronair anatomie en de myocardiale ischemie heeft de potentie om de diagnose te verbeteren, hetgeen mogelijk vertaald kan worden naar een verbeterde zorg voor de patiënt. Op dit moment wordt de fractional flow reserve (FFR) gezien als de referentie-standaard om de functionele ernst van de coronaire vernauwing te bepalen in het catheterisatie laboratorium. De integratie van de gepresenteerde co-registratie benadering met de FFR zou de volgende stap kunnen zijn op weg naar een optimale bepaling van de ernst van de ischemische CAD en voor het ondersteunen van coronaire interventies.

List of Abbreviations

AAD	acquisition angle difference
ABOVA	anatomy-defined bifurcation optimal viewing angle
BMS	bare-metal stents
DBA	distal bifurcation angle
DICOM	digital imaging and communications in medicine
DMV	distal main vessel
ED	end-diastolic
DES	drug-eluting stents
EVA	expert viewing angle
IVUS	intravascular ultrasound
LAD	left anterior descending
LAO	left anterior oblique
LCx	left circumflex artery
LD	long diameter
LM	left main
MLD	minimum lumen diameter
OBOVA	obtainable bifurcation optimal viewing angle
OAV	observer agreement value
OCT	optical coherence tomography
OM	obtuse marginal
PBA	proximal bifurcation angle
PCI	percutaneous coronary interventions
PDA	posterior descending artery
PLA	posterolateral artery
PMV	proximal main vessel
PTCA	percutanueous transluminal coronary angioplasty
PVA	perspective viewing angle
QCA	quantitative coronary angiography
RAO	right anterior oblique
RCA	right coronary artery
RI	ramus intermedius
SB	sidebranch
SD	short diameter
SGLI	stick-guided lateral inhibition
SSV	sample scoring value
SVA	software viewing angle
UM	unsharp masking
XA	X-ray angiography

Publications

Journal papers

1. **Tu S**, Jing J, Holm NR, Onsea K, Zhang T, Adriaenssens T, Dubois C, Desmet W, Thuesen L, Chen Y, Reiber JHC. In-vivo Assessment of Bifurcation Optimal Viewing Angles and Bifurcation Angles by Three-dimensional (3D) Quantitative Coronary Angiography. International Journal of Cardiovascular Imaging 2011. Epub Ahead of Print, DOI: 10.1007/s10554-011-9996-x.
2. **Tu S**, Xu L, Ligthart J, Xu B, Witberg K, Sun Z, Koning G, Reiber JHC, Regar E. In-vivo Comparison of Arterial Lumen Dimensions Assessed by Co-registered Three-dimensional (3D) Quantitative Coronary Angiography, Intravascular Ultrasound and Optical Coherence Tomography. International Journal of Cardiovascular Imaging 2012. Epub Ahead of Print, DOI: 10.1007/s10554-012-0016-6.
3. **Tu S**, Hao P, Koning G, Wei X, Song X, Chen A, Reiber JHC. In-vivo assessment of optimal viewing angles from X-ray coronary angiograms. EuroIntervention 2011; 7(1):112-120.
4. **Tu S**, Holm N, Koning G, Maeng M, Reiber JHC. The impact of acquisition angle difference on three-dimensional quantitative coronary angiography. Catheterization and Cardiovascular Interventions 2011; 78(2):214-222.
5. **Tu S**, Holm NR, Koning G, Huang Z, Reiber JHC. Fusion of 3D QCA and IVUS/OCT. International Journal of Cardiovascular Imaging 2011; 27(2):197–207.
6. Reiber JHC, **Tu S**, Tuinenburg JC, Koning G, Janssen JP, Dijkstra J. QCA, IVUS and OCT in Interventional Cardiology in 2011. Cardiovascular Diagnosis and Therapy 2011; 1(1):57-70.
7. Wijns W, **Tu S**. Transluminal attenuation gradient analysis - A new approach for diagnostic optimization of coronary computed tomography angiography. Journal of the American College Cardiology: Cardiovascuar Imaging 2011; 4(11):1158-1160. (Editorial Comment)
8. Holm NR, **Tu S**, Christiansen EH, Reiber JHC, Lassen JF, Thuesen L, Maeng M. Use of 3-dimensional optical coherence tomography to verify correct wire position in a jailed side branch after main vessel stent implantation. EuroIntervention 2011; 7:528-529.
9. **Tu S**, Koning G, Jukema W, Reiber JHC. Assessment of obstruction length and optimal viewing angle from biplane X-ray angiograms. International Journal of Cardiovascular Imaging 2010; 26(1):5–17.
10. **Tu S**, Huang Z. Koning G, Cui K, Reiber JHC. A novel three-dimensional quantitative coronary angiography system: In-vivo comparison with intravascular ultrasound for assessing arterial segment length. Catheterization and Cardiovascular Interventions 2010; 76(2):291-298.
11. **Tu S**, Koning G, Tuinenburg JC, Jukema W, Zhang S, Chen Y, Reiber JHC. Coronary angiography enhancement for visualization. International Journal of Cardiovascular Imaging 2009; 25(7):657–667.
12. **涂圣贤**, 魏向龙, 宋旭东, 郝培远, 黄铮, Koning G, Reiber JHC. 一种从冠状动脉X线造影生成最佳投照角度的新方法. 中华放射学, 2011, 45(2): 195-198.
13. 郝培远，陈爱华，宋旭东，魏向龙，周珊珊，何非，**涂圣贤**. 三维、二维定量冠脉X射线造影与目测对靶病变血管的评估对比研究. 南方医科大学学报 2011; 31(2):333-337.
14. 刑栋，杨丰，黄靖，**涂圣贤**，Dijkstra J. 结合硬斑块特征的心血管内超声图像中-外膜边缘检测. 中国生物医学工程学报. Accepted.

Abstracts

1. **Tu S**, Holm N, Koning G, Maeng M, Reiber JHC. The impact of acquisition angle difference on three-dimensional quantitative coronary angiography. EuroIntervention (Supplement) 2011; 7:M113.
   EuroPCR 2011, Paris.
2. Mangiacapra F, Conte M, **Tu S**, Peace AJ, Di Serafino L, Ntarladimas I, Barbato E, De Bruyne B, Reiber JHC, Wijns W. Performance of three-dimensional vs. two-dimensional quantitative coronary angiography in discriminating functionally significant coronary stenosis according to fractional flow reserve. EuroIntervention (Supplement) 2011; 7:M144.
   EuroPCR 2011, Paris.
3. **Tu S**, Holm NR, Koning G, Reiber JHC. A new approach to co-register X-ray angiography and intravascular ultrasound/optical coherence tomography.
   Asian Society of Cardiovascular Imaging 2011, Hongkong.
4. **Tu S**, Holm NR, Huang Z, Koning G, Cui K, Hou Y, Reiber JHC. A Novel Approach for the Co-registration of Coronary Angiography and Intravascular Ultrasound Images: A Validation Study. JACC Transcatheter Cardiovascular Therapeutics - Invasive Imaging (Supplement B) 2010; 56 (13):B82.
   TCT 2010, Washington.
5. **Tu S**, Koning G, Hao P. Wei X, Song X, Chen A, Reiber JHC. A New Approach to Assess Optimal Viewing Angles for Interventional Stent-procedure from X-ray Coronary Angiography. JACC Transcatheter Cardiovascular Therapeutics – No-Invasive Imaging (Supplement B) 2010; 56 (13):B86.
   TCT 2010, Washington.
6. **Tu S**, Gerhard K, Huang Z, Cui K, Rares A, Janssen JP, Reiber JHC. Coronary intervention planning by fusing angiogram and IVUS.
   Dutch Society for Pattern Recognition and Image Processing 2009; Leiden.

Acknowledgments

This thesis describes the work which was performed between 2008 and 2011 under the supervision of Prof. dr. ir. J.H.C. Reiber and ir. G. Koning at the Division of Imaging Processing (LKEB), Department of Radiology, Leiden University Medical Center, and at the Department of Applied Research, Medis medical imaging systems bv, the Netherlands. Through the course of my PhD quest, many people have contributed to this thesis and I would like to express my gratitude to them.

I would like to thank the XA research group in Medis. The clinical knowledge of Gerhard and Joan, and the programming skills of Jasper and Andrei have inspired me tremendously over the past years. I owe you many, many thanks for all your help!

I am also very grateful to all my other colleagues in LKEB and in Medis. Pieter, your prompt help in the MeVisLab programming is very much appreciated. Berend, the discussions on Statistics are very helpful. Jouke, thanks for the discussions on intravascular ultrasound imaging. Boudewijn and Rob, thank you for your help in the ASCI school registration and the layout of this thesis. Kees, Clemens, Marleen, Marcel, and Sonia, I will always remember the coffee/tea time and your help in Dutch. Angela, Ellemiek, David and Lars, many thanks for the remote IT supports while I was carrying out validations in the hospitals. The M&S and R&D teams, I appreciate your consistent supports as well.

Through all the validation studies, I got tremendous supports from many physicians, technicians, and engineers around the world. Niels Holm, thank you so much for your prompt feedbacks and for all your helps. I cannot even count how many e-mails and talks we had for the past year. Bo Xu, Evelyn Regar, Jurgen Ligthart, Tom Adriaenssens, Williams Wijns, Yundai Chen, Zheng Huang, and Xianglong Wei, thank you for all the arrangements and efforts to make the validations possible. I benefited a lot from our clinical discussions as well. Kevin Onsea, Liang Xu, Jing Jing, Peiyuan Hao, Tao Zhang, Kai Cui, Karen Witbert, Paul De Graaf, Fabio Mangiacapra, Stelios Pyxaras, Olivier Nelis, Zhongwei Sun, Jozef Adams, and Andy Wiyono, I enjoy a lot working with you. Albert Bruschke, Xudong Song, Yasuhiro Ishii, Hiram Bezerra, Xiao De, Wouter Jukema, Christophe Dubois, Walter Desmet, Michael Maeng, Leif Thuesen, Yazhu Chen, Su Zhang, Feng Yang, Tobias Boskamp, Patrick Brouwer, and Alexandra Lansky, many thanks for all your interests and your contributions.

I am very grateful to be surrounded by my family with full love and harmony. 爸爸，妈妈，感谢你们多年来一直在支持我，鼓励我。你们无私的爱与默默的关怀，一直是我最强大的精神动力。姐姐，我最想说的是：有你这个姐姐真好！

Yinghui, thank you for sharing all the excitements, joys and sorrows with me during my PhD study. Particularly, thank you so much for giving me such a precious daughter. Minghua, it is such a great pleasure to witness your growth every day! Your laugh always lights up my day.

Curriculum vitae

Shengxian (Sanven) Tu was born in Raoping, Guangdong, China on September 17, 1981. In 2000 he received his secondary school degree from Fengzhou Middle School in Raoping and started his bachelor study on Biomedical Engineering, at Southern Medical University (formerly known as First Military Medical University), Guangzhou, China. He received the bachelor degree in July 2005. In the same year, he was admitted by the Department of Biomedical Engineering, Shanghai Jiao Tong University, Shanghai, China, as a master student, under the supervision of Prof. ir. Yazhu Chen and dr. ir. Su Zhang. He graduated in February 2008 with a thesis entitled "Image-guided targeting in treatment planning for focused ultrasound therapy" and was awarded the title "Shanghai Outstanding Graduate Student". Right after his graduation, he joined the XA research group at the Department of Applied Research, Medis medical imaging systems as a scientific researcher, while at the same time pursuing a PhD degree at the Division of Image Processing (LKEB), Department of Radiology, Leiden University Medical Center, Leiden, the Netherlands, under the supervision of Prof. dr. ir. J.H.C. Reiber and ir. G. Koning. He has been working on the project of coronary vascular reconstruction from X-ray angiographic images and the fusion with intravascular ultrasound (IVUS) and optical coherence tomography (OCT), plus the use of 3D OCT for support of coronary interventions. The works are presented in this thesis and the algorithms were integrated into prototype software packages that were installed and validated in a number of hospitals around the world. At the early of 2011, he was awarded the "Outstanding Oversea Chinese Student" for his PhD study by the Ministry of Education of the People's Republic of China.

Currently he continues his research and development on multi-modality imaging at Medis medical imaging systems. His research interests include image reconstruction, quantitative analysis, image fusion and image-guided therapy.